Università di Genova

Scuola Politecnica

DIME

Dipartimento di Ingegneria Meccanica, Energetica

Gestionale e dei Trasporti

Master's Degree in Mechanical Engineering

-

Energy and Aeronautics

Investigation of thermoacoustic instabilities in a simple model of a gas turbine combustor

Students

Lorenzo Carrattieri

Giulia Innocenti

Supervisor

Prof. Alessandro Bottaro

December 19, 2022

Alla mia famiglia,
a chi mi è stato vicino.

L. C.

Alla mia famiglia,
a chi mi è stato vicino.

G. I.

Abstract

This work aims to investigate the thermoacoustic behavior, both linear and nonlinear, of the premixed combustor model described by Dowling and Stow [1]. It is composed of three ducts: a plenum, a premixer, and lastly a combustion chamber.
The first part of the work involves the application of a low-order lumped parameter model to the system, treated as one-dimensional. The purpose is to solve an eigenvalue problem to predict the resonant modes. Consequently, these results are validated with the solutions provided by the reference paper.
Secondly, the nonlinear behavior of the modeled combustor is examined with the help of the software Ansys Fluent; this investigation represents the main body of the work. After defining a proper unstructured mesh, the combustion reaction is characterized without a specific combustion model, but simply by defining a specific region of cells, downstream of the premixed duct, whose temperature or heat release rate is controlled. Concerning the turbulence modeling, the $k-\omega$ SST model is chosen to perform steady and unsteady simulations.
To gain experience with the thermoacoustic problem, the flame temperature is firstly controlled by prescribing a specific law that varies with time.
Secondly, the unsteady heat release rate provided by the flame is defined. This is accomplished by implementing an expression analogous to Crocco's model [2], which depends on some flow variables sampled before the flame.
For both cases, the numerical tests result in a decay of the system to a stable state or into an unstable state, characterized by growing oscillations, which then saturate, reaching a limit cycle.
The last part of the work looks at ways to damp the thermoacoustic instabilities; the first proposed option is to implement a porous diaphragm located in the premixer, its operation, and its validity are analyzed by varying its porosity. Similarly, another possibility to mitigate the instabilities is studied by inserting a porous medium after the flame, in the combustion chamber. Three possible positions are investigated, and the most effective results are discussed. As final solution, an axisymmetric Helmholtz resonator is designed, and its ability to prevent instabilities is examined for different operating conditions, again by varying its position inside the combustion chamber, and its dimensions. The resonator appears to be a very effective tool to damp even large amplitude acoustic fluctuations.

Prefazione

Questa tesi si propone di studiare il comportamento termoacustico, lineare e non lineare, del modello di combustore premiscelato descritto da Dowling e Stow [1].
Il modello è composto da tre condotti: un plenum, un premiscelatore e infine una camera di combustione.
La prima analisi prevede l'applicazione di un approccio modellistico al sistema, trattato come monodimensionale, a parametri concentrati di ordine ridotto. Lo scopo è quello di risolvere un problema agli autovalori per prevedere i modi di risonanza. Successivamente, questi risultati vengono convalidati con le soluzioni fornite dall'articolo di riferimento.
In secondo luogo, il comportamento non lineare del modello di combustore viene esaminato con l'aiuto del software Ansys Fluent; questa indagine rappresenta il corpo principale del testo. Una volta definita un'adeguata mesh non strutturata, la reazione di combustione è caratterizzata senza uno specifico modello di combustione, ma semplicemente definendo una specifica regione di celle a valle del condotto premiscelato, di cui si controlla la temperatura o il tasso di rilascio di calore. Per quanto riguarda la modellazione della turbolenza, è stato scelto il modello di turbolenza $k - \omega$ SST eseguendo simulazioni stazionarie e instazionarie.
Per acquisire esperienza con il problema termoacustico, la temperatura della fiamma viene controllata in primo luogo prescrivendo una legge specifica che varia con il tempo. In secondo luogo, si definisce il tasso di rilascio di calore instazionario fornito dalla fiamma. Ciò si ottiene implementando un'espressione analoga al modello di Crocco [2], che dipende da alcune variabili di flusso campionate prima della fiamma.
Per entrambi i casi, le prove numeriche danno come risultato un decadimento del sistema verso uno stato stabile o il raggiungimento di uno stato instabile, caratterizzato da oscillazioni crescenti, che poi saturano, raggiungendo una condizione di ciclo limite.
L'ultima parte del lavoro esamina i modi per smorzare le instabilità termoacustiche; la prima opzione proposta è quella di implementare un setto poroso situato nel premiscelatore, il suo funzionamento e la sua validità vengono analizzati variandone la porosità. Allo stesso modo, un'altra possibilità per mitigare le instabilità è studiata inserendo un mezzo poroso dopo la fiamma, nella camera di combustione, in tre diverse posizioni. Come ultima soluzione, si progetta un risonatore di Helmholtz assialsimmetrico e si esamina la sua capacità di prevenire le instabilità, variandone la sua posizione all'interno della camera di combustione e le sue dimensioni. Il risonatore risulta essere un dispositivo molto efficace per smorzare fluttuazioni acustiche anche di grande ampiezza.

Ringraziamenti

Raggiunta la conclusione di questa tesi, vorrei innanzitutto ringraziare il professor Alessandro Bottaro. Questa esperienza mi ha permesso di stare a contatto con quello che amo definire un luminare della meccanica dei fluidi, capace di trasmettere la sua forte passione e la sua grande conoscenza in materia.
Inoltre, ringrazio la mia fortissima compagna di tesi Giulia.

Desidero ringraziare mia mamma, mia sorella e mia nonna per il loro sostegno psicologico, finanziario e la loro vicinanza presente anche a distanza. Allo stesso modo ringrazio Matteo, partecipe in ogni singolo momento di questo percorso, sempre con consigli preziosi.

Ringrazio Alice, Beatrice, Laura e Margherita, amiche insostituibili, senza il cui supporto difficilmente avrei potuto affrontare alcune difficoltà. Grazie a Virgina per tutto l'aiuto, fin dal primo giorno in questa città, e per le magiche serate.
Infine, ringrazio tutti coloro che durante questi anni mi sono stati vicini, grazie a tutti gli amici di Reggio, di Modena, grazie a Giuseppe e Francesco con cui ho avuto la fortuna di condividere casa e apprezzare ogni momento di compagnia.

Ringraziamenti

Ringrazio il Prof. Bottaro per avermi dato l'opportunità di svolgere questa tesi e per avermi trasmesso il suo entusiasmo e la sua passione per la ricerca, è per me fonte di grande ispirazione.
Inoltre, ringrazio anche il mio fortissimo compagno di tesi, Lorenzo.

Uno speciale ringraziamento va alla mia famiglia, il mio porto sicuro.
Ai miei genitori che mi accompagnano in ogni mio percorso, gioendo delle mie vittorie e standomi accanto nei momenti più bui. Grazie per avermi sempre dato la giusta carica per affrontare le sfide della vita e per avermi cresciuta così perché è solo grazie a voi se sto diventando la donna che voglio essere.
A Chiara e Luca, da sempre al mio fianco come fratelli, grazie per farmi sentire il vostro punto di riferimento o come diceste una volta il vostro 'idolo', perché voi siete il mio.
Ai miei secondi genitori, Marina e Daniele, mi avete supportata fin da piccola ed oggi siete qui a vivere con me uno dei traguardi più importanti della mia vita, grazie per non avermi mai fatto mancare nulla.
Ai miei zii, Bruna e Paolo, e a mia cugina Sara per avermi fatto sentire importante, sostenuta ma soprattutto amata.
A mia nonna Marisa e a miei nonni che mi proteggono, grazie per i vostri insegnamenti preziosi.

Un grazie dal profondo del cuore è per i miei amici, perle rare.
A te Ali, il mio punto fermo, grazie per non esserti mai persa un "in bocca al lupo" per ogni mio esame ed essere sempre presente in ogni occasione della mia vita.
A te Mirti, la mia fan numero 1, grazie per credere così tanto in me, mi hai dato tanta grinta e coraggio.
Grazie a #8mismo perché nonostante le strade così diverse che stiamo prendendo, rimanete gli amici di sempre.
Grazie al mio super gruppo di amiche, le Catacite, mi avete regalato tanti momenti insieme di spensieratezza e di leggerezza, di cui ho spesso bisogno.
Grazie ai miei compagni di università, Eli, Assa e Rob, siete stati parte del mio percorso di studio, abbiamo condiviso davvero ogni singolo esame, sofferenza, paura, ma anche gioia e soddisfazione, mi avete fatto tirare fuori tanta determinazione, ci siamo sostenuti a vicenda senza lasciare che nessuno dei quattro rimanesse indietro. Davvero grazie perché il mio percorso è stato questo anche per merito vostro.

Grazie al mio complice, la mia anima affine, Ercole. Circa 5 anni fa, condividendo con me la tua passione e la tua forte curiosità per l'ingegneria hai acceso una scintilla nella me liceale ed è anche grazie a te che ho scelto di intraprendere questa strada. Grazie per avermi ascoltata e aiutata, grazie per essere fiero di me e per dimostrarmelo ogni giorno, sei il mio rifugio di serenità.

Infine, grazie a tutti gli amici, i familiari e i conoscenti, vicini e lontani, che hanno incrociato la loro vita con la mia lasciandomi qualcosa di buono e non facendomi mai sentire sola.

Contents

Symbology

Symbols

$\bar{}$	Base quantity
$'$	Perturbation quantity
$\bar{}$	Complex conjugate
^{T}	Transpose
$\dot{}$	Time derivative
δ_{hk}	Kronecker delta
i	Imaginary unit
c_p	Specific heat at constant pressure
c_v	Specific heat at constant volume
$\gamma = \frac{c_p}{c_v}$	ratio of the specific heats
$\mathbf{u}$	Velocity vector
p	Pressure
t	Time
ρ	Density
$\dot{Q}$	Heat transfer rate
Q	Heat transfer rate per unit volume
q	Heat transfer rate per unit area
$\sigma_{i,j}$	Viscous stress tensor
$\mathbf{e_i}$	Unit vector along coordinate i

T	Temperature
R_{gas}	Gas constant
k	Conductivity
S	Entropy
c	Speed of sound
ω	Complex frequency
St	Strouhal number
δ_L	Laminar flame thickness
l_0	Kolmogorov turbulence scale
l_K	Integral turbulence scale
Re	Reynolds number
Da	Damköhler number
Le	Lewis number

1 Introduction

The necessity to reduce nitrogen oxide emissions, in response to stricter regulations, has led to the adoption of new combustion techniques, such as the lean premixed prevaporized (LPP) combustion, a process that allows combustion with a lower mean temperature that inhibits thermal NO_x formation. This type of technology has the downside to be more susceptible to thermoacoustic instability, an anomaly characterized by large-amplitude velocity and pressure oscillations and possible undesirable effects, e.g. fatigue cracking, increased emissions, deterioration of the gas turbine system performance, flame blowoff or flashback, higher heat transfer rates. This is also a result of the high energy densities, in the order of 0.1 GW/m^3, and the low damping that characterizes a typical gas turbine combustor. Since nowadays LPP combustion is one of the best ways to reduce dangerous pollutants, thermoacoustic instabilities have become one of the major topics of research in the design of gas turbine combustors. In LPP combustors, liquid fuel vaporizes and mixes with air before entering the combustion chamber. Ignition, flame anchoring, and safety are provided by a pilot diffusion flame, because still today, a combustion based only on an LPP technology is not safe enough.

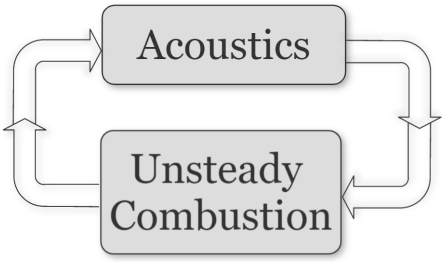

Figure 1.1: Schematic representation of the positive feedback between acoustics and unsteady combustion.

Combustion instability is, therefore, an unsteady phenomenon and occurs at well-defined frequencies, it is caused by the positive feedback between acoustics and combustion. When this happens, loud sounds develop in the combustion chamber, which are different from the combustion noise that comes from turbulent fluctuations. Essentially, unsteady combustion generates acoustic waves, which alter the inlet flow rates of fuel and air. At lean premixed conditions, this changed fuel-air ratio leads to significant unsteady combustion, and consequently an unsteady heat release rate. If the phase relationship is suitable, self-excited oscillations grow in a confined space [3]. This is the basic idea of positive feedback. The frequencies of the combustion dynamics are proximate to the acoustic resonance frequencies of the combustion system. Although the coupling between combustion and acoustics alters the frequencies of the oscillations, in many situations this difference is not so far from the resonance ones. This phenomenon is difficult to predict and the engi-

neering approach to eliminate it is typically expensive.
The flame can be considered as a source adding energy in a resonator. If the acoustic energy created is more than the one which is lost due to damping, then the oscillations will grow. If they balance, a limit cycle might be reached. A limit cycle is a trajectory for which the energy of the system would be constant over a cycle - i.e. on average, there is no loss or gain of energy [4].
The mechanisms involved in the interaction between the flame and the acoustics include hydrodynamic instabilities, gas dynamics, chemical reactions, heat transfer, multi-phase flows, and so on. Importantly, these mechanisms are not confined to the vicinity of the combustion zone [5]. For example, bluff bodies shed vortices, as consequence, there are hydrodynamic fluctuations scales, if these scales match with the acoustic ones, there might be instability.

2 Generalities on combustion instabilities

2.1 Brief recap on acoustics

As previously presented in the introduction, **acoustics** deals with the generation, propagation, and effects of sound. **Sound** is defined as a disturbance of the pressure field, which propagates at finite speed in a compressible medium, be it solid, liquid or gas. In this work, the attention will be only on gas mediums. The propagation of sound translates into *pressure waves*, they can be *transverse*, but typically they do not develop in gases or *longitudinal*, which means that particles move along the traveling direction of the wave.

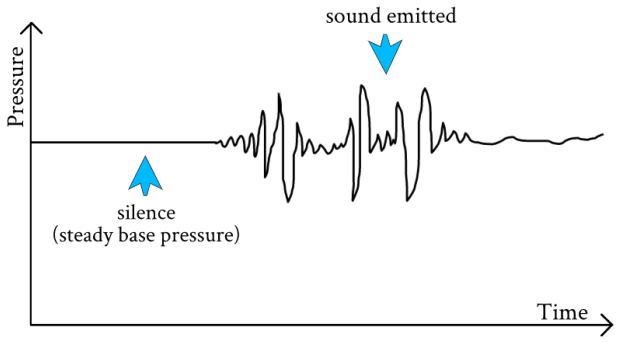

Figure 2.1: Illustration of a transition in time from silence (steady base pressure) to sound emission (generation of perturbations of pressure).

Pressure then is generally decomposed as the sum of a mean or base pressure, $\bar{p}$, (please note it is a time mean) and a fluctuating or acoustic pressure, $p'(\mathbf{x}, t)$.

$$p = p(\mathbf{x}, t) = \bar{p} + p'(\mathbf{x}, t) \tag{2.1}$$

where t stands for time and $\mathbf{x}$ for the position vector. Afterward, the acoustic pressure can be expressed in the frequency domain by a complex amplitude $\hat{p}$ and an angular frequency ω.

$$p'(\mathbf{x}, t) = \hat{p}(\mathbf{x})e^{i\omega t} \tag{2.2}$$

Obviously, to obtain the instantaneous value of pressure, we start from the complex amplitude $\hat{p}(\mathbf{x})$, multiply for the term $e^{i\omega t}$ and then take the real part of this product.

$$\begin{aligned} p'(\mathbf{x}, t) = \hat{p}(\mathbf{x})e^{i\omega t} = [\hat{p}(\mathbf{x})_{real} + i\hat{p}(\mathbf{x})_{imaginary}][cos(\omega t) + isin(\omega t)] = \\ = [\hat{p}(\mathbf{x})_{real}cos(\omega t) - \hat{p}(\mathbf{x})_{imaginary}sin(\omega t)] + i[\hat{p}(\mathbf{x})_{real}sin(\omega t) + \hat{p}(\mathbf{x})_{imaginary}cos(\omega t)] \end{aligned} \tag{2.3}$$

Consequently,

$$Re[p'(\mathbf{x}, t)] = \hat{p}(\mathbf{x})_{real}cos(\omega t) - \hat{p}(\mathbf{x})_{imaginary}sin(\omega t) \tag{2.4}$$

The instantaneous trend of acoustic pressure is not suitable for characterizing a sound, because it is "cumbersome," i.e. it requires large storage media, is redundant with information, and, among other things, does not highlights aspects of interest. Therefore, it is necessary to identify quantities that will allow one to do so in a manner appropriate to the accuracy of the analysis to be performed.
The first quantity to be considered is the mean square value, which is the square of the root mean square value:

$$p_{RMS}^2 = \lim_{T\to+\infty} \frac{1}{T} \int_{-T/2}^{T/2} [p(\mathbf{x},t) - \bar{p}]^2 dt = \lim_{T\to+\infty} \frac{1}{T} \int_{-T/2}^{T/2} p'(\mathbf{x},t)^2 dt \quad [Pa^2] \tag{2.5}$$

For periodic signals of period T_0, we can employ:

$$p_{RMS}^2 = \frac{1}{T_0} \int_{-T_0/2}^{T_0/2} p'(\mathbf{x},t)^2 dt \quad [Pa^2] \tag{2.6}$$

Given that acoustics cannot disregard the perception of sounds by the human ear, it is necessary to introduce a quantity that is closer to perception than p_{RMS}. As a first approximation, we can say that, on average, healthy humans perceive "pure tones," in a range of frequency within 20 to 20000 Hz and with p_{RMS} values above 0.00002 Pa (20 Pa), the so-called threshold of audibility; around p_{RMS} = 100 Pa there is the so-called pain threshold (actually these values are relative to pure tones at 1 kHz and vary significantly with frequency). As a result, the values of interest vary over a range of 7 orders of magnitude, thus posing representation problems.
Please remember that the sensitivity of the human ear and, in particular the threshold of audibility, depends on the frequency and also on the particular type of sound. Sounds composed of several pure tones of different frequencies are called "complex tones" and, there are then sounds so-called broadband sounds, in which no particular frequencies predominate, but instead there are "frequency ranges" of greater or lesser extent.
In addition to this, it should be considered that, roughly speaking, the perception of sounds is logarithmic, that is, the sensation of the "sound volume" is not proportional to p_{RMS} but is related to its logarithm, that is, to its order of magnitude. Therefore, reference is made to the so-called "level". Namely, the logarithm (in base 10) of p_{RMS}. To make the result used for p_{RMS} nondymensional, one must refer it to a reference value p_{ref}, commonly assumed to be equal to 20 μPa, which is the threshold of audibility. Essentially, one should work with $log_{10}(p_{RMS}/p_{ref})$, obtaining a level expressed in *Bel*. However, this choice has two disadvantages:

- the entire scale of sounds of practical interest would reduce into only 7 integer values, therefore, deciBel: $10 \cdot log_{10}(p_{RMS}/p_{ref})$ is used;
- in addition, the value obtained wouldn't be directly related to the powers, which are proportional to the square of p_{RMS}

As a result of this, the **sound pressure level (SPL)** or acoustic pressure level is defined as:

$$L_p = SPL = 10 \cdot log_{10}\left(\frac{p_{RMS}^2}{p_{ref}^2}\right) = 20 \cdot log_{10}\left(\frac{p_{RMS}}{p_{ref}}\right) \quad [dB] \tag{2.7}$$

Therefore, the threshold of audibility corresponds to 0 dB, and the threshold of pain corresponds to 20log10(100 Pa / 0.00002 Pa) = 134 dB. It follows that the range of sounds of interest can be represented by a scale of 134 integer values, thus offering good resolution. Sometimes, for convenience, the pain threshold is assumed to correspond to 140 dB. Moreover, given the uncertainties to which pressure measurements over such a wide range are subject, the variability of the phenomena involved, the strong dependence of perception on frequency, and also subjective aspects, only integer values of SPL are often reported and hardly more than decimal digits are given.
For the same reasons, approximations unacceptable in many other fields of engineering, such as fluid dynamics, are common in acoustics, since, working with levels, one is interested in orders of magnitude rather than in the values of physical quantities. In practice, the quantity defined in the previous equations is called **OASPL**, an acronym for overall sound pressure level, to distinguish it from SPL, which is usually used to refer to the frequency distribution or the so-called spectrum [6].

Source	sound pressure level in dB	corresponding pressure in Pa
Jet aircraft, 50 m away	140	200
Threshold of pain	130	63.2
Threshold of discomfort	120	20
Chainsaw, 1 m distance	10	6.3
Disco concert, 1 m from speaker	100	2
Diesel truck, 10 m away	90	0.63
Kerbside of busy road, 5 m	80	0.2
Vacuum cleaner, 1 m away	70	0.063
Conversational speech, 1 m distance	60	0.02
Average home	50	0.0063
Quiet library	40	0.002
Quiet bedroom at night	30	0.00063
Background in TV studio	20	0.0002
Calm breathing	10	0.000063
Threshold of hearing	0	0.00002

Figure 2.2: Common values of sound pressure levels.

2.2 Linearized equations of motion

Following the definitions given in [1], for a compressible viscous fluid, without external forces, conservation of mass and momentum bring to the Navier-Stockes equations,

$$\frac{D\rho}{Dt} + \rho\,\boldsymbol{\nabla}\cdot\mathbf{u} = 0; \quad \rho\frac{D\mathbf{u}}{Dt} = -\boldsymbol{\nabla}p + \frac{\partial\sigma_{i,j}}{\partial x_j}\mathbf{e_i} \tag{2.8}$$

Here $\frac{D}{Dt} = \frac{\partial}{\partial t} + \mathbf{u}\cdot\boldsymbol{\nabla}$ is the material derivative, $\mathbf{e_i}$ is the unit vector in the direction of coordinate *i*. For a perfect gas we have the gas law $p = R_{gas}\rho T$, remembering that $R_{gas} = c_p - c_v$ is the gas constant. The internal energy per unit mass is $e = c_v T$, and the

enthalpy $h = c_p T = e + \frac{p}{\rho}$. The conservation of energy returns the following equation

$$\rho \frac{D}{Dt}\left(e + \frac{1}{2}\mathbf{u}^2\right) = -\boldsymbol{\nabla}\cdot(p\mathbf{u}) + Q + \boldsymbol{\nabla}\cdot(k\boldsymbol{\nabla}T) + \frac{\partial(\sigma_{i,j}u_i)}{\partial x_j} \tag{2.9}$$

where we remember k being the the conductivity and Q the heat release addiction per unit volume. Combining the momentum equation with the energy equation, this can be rewritten in terms of enthalpy:

$$\rho \frac{Dh}{Dt} = \frac{Dp}{Dt} + Q + \boldsymbol{\nabla}\cdot(k\boldsymbol{\nabla}T) + \sigma_{i,j}\frac{\partial u_i}{\partial x_j} \tag{2.10}$$

In addition, one can also define an entropy equation from the thermodynamic relation $dh = TdS + \frac{1}{\rho}dp$. Hence, from the previous equation it results:

$$\rho T \frac{DS}{Dt} = Q + \boldsymbol{\nabla}\cdot(k\boldsymbol{\nabla}T) + \sigma_{i,j}\frac{\partial u_i}{\partial x_j} \tag{2.11}$$

From this, we can see that heat input, heat transfer, and viscous effects lead to an entropy increase. Finally, by taking the curl of the momentum equation and including the mass equation, the equation for the development of vorticity, $\xi = \boldsymbol{\nabla}\times\mathbf{u}$ is found,

$$\frac{D}{Dt}\left(\frac{\xi}{\rho}\right) = \left(\frac{\xi}{\rho}\cdot\boldsymbol{\nabla}\right)\mathbf{u} + \frac{1}{\rho^3}\boldsymbol{\nabla}\rho\times\boldsymbol{\nabla}p + \frac{1}{\rho}\boldsymbol{\nabla}\times\left(\frac{1}{\rho}\frac{\partial\sigma_{i,j}}{\partial x_j}\mathbf{e_i}\right) \tag{2.12}$$

On the right-hand side of this last equation, the first term describes how the stretching of vortex lines intensifies the local vorticity, the second term indicates that vorticity can be created when there is a misalignment between the density and pressure gradients, such as an acoustic pressure oscillation with a component normal to a flame front (characterized by a density gradient). Ultimately, the third term expresses the generation of vorticity by viscous effects.
From now on, we will assume the fluid to be inviscid, $\sigma_{i,j} \equiv 0$, the gas is ideal, so there is also no heat conduction, and c_v, c_p are assumed to be constant. We then find entropy $S = log(\frac{p}{\rho^\gamma})$, plus an arbitrary constant set equal to zero.
The flow is then taken to be decomposed into a steady uniform flow (denoted by overbars, which stand for a time mean) and a small perturbation (indicated by primes). As already mentioned, pressure is decomposed as,

$$p = p(\mathbf{x}, t) = \bar{p} + p'(\mathbf{x}, t) \tag{2.13}$$

and similarly for the other flow variables. Consequently, the linearized version of the equations of conservation for mass, momentum, energy, entropy, and vorticity results in:

$$\frac{\bar{D}\rho'}{Dt} + \bar{\rho}\,\boldsymbol{\nabla}\cdot\mathbf{u}' = 0 \tag{2.14}$$

$$\frac{\bar{D}\mathbf{u}'}{Dt} + \frac{1}{\bar{\rho}}\,\boldsymbol{\nabla}\,p' = \mathbf{0} \tag{2.15}$$

$$\bar{\rho}\bar{T}\frac{\bar{D}S'}{Dt} = Q' \tag{2.16}$$

$$\frac{\bar{D}\xi'}{Dt} = \mathbf{0} \tag{2.17}$$

where $\frac{\bar{D}}{Dt} = \frac{\partial}{\partial t} + \bar{\mathbf{u}} \cdot \boldsymbol{\nabla}$. Moreover, $\bar{\xi}$ has been set to zero. Now, by using the definition for $S' = c_v \frac{p'}{\bar{p}} - c_p \frac{\rho'}{\bar{\rho}}$ and combining the four previous equations, we come to an inhomogeneous equation for pressure, the *wave equation*,

$$\frac{1}{\bar{c}^2}\frac{\bar{D}^2 p'}{Dt^2} - \boldsymbol{\nabla}^2 p' = \frac{\gamma - 1}{\bar{c}^2}\frac{\bar{D}Q'}{Dt} \tag{2.18}$$

where c is the speed of sound. If there is no unsteady heat release rate, then the linearized pressure equation and the linearized entropy equation are uncoupled.

An important aspect that needs to be kept in mind is that any perturbation can be assumed as the sum of three types of disturbance [7]:

- an acoustic disturbance that is isentropic and irrotational.
- an entropy disturbance that is incompressible and irrotational.
- a vorticity disturbance that is incompressible and isentropic.

These three types are independent and can be considered separately. So, for the pressure disturbance one has $S' = 0$ and $\xi' = \mathbf{0}$; hence $\rho' = \frac{p'}{\bar{c}^2}$. Considering no heat release fluctuations ($Q' = 0$), the wave equation becomes:

$$\left(\frac{1}{\bar{c}^2}\frac{\bar{D}^2}{Dt^2} - \boldsymbol{\nabla}^2\right) p' = 0 \tag{2.19}$$

with the corresponding velocity fluctuation, $\mathbf{u}'$ obtained thanks to the momentum equation. These solutions are acoustic waves that propagate at the speed of sound, relative to the fluid. Next, for the entropic disturbances, $p' = 0$, $\mathbf{u}' = \mathbf{0}$. From the linearized equation for entropy, the reader can see that the entropy wave is convected with the mean flow, so it is stationary relative to the fluid, sometimes this is labeled as *hot spot*. Likewise, for the vortical disturbance, $p' = \rho' = 0$ and $\boldsymbol{\nabla} \cdot \mathbf{u}' = \mathbf{0}$; the linearized vorticity equation shows that also this type of disturbance is convected with the mean flow. Consequently, if the mean flow is zero, we will have only acoustic waves.

2.3 The Rayleigh criterion

2.3.1 Analytical derivation

By the end of the nineteenth century, Lord Rayleigh had formulated a criterion to explain how acoustic waves could be excited and sustained by heat addition. Lord Rayleigh stated his principle with the following words:

"If heat be communicated to, and abstracted from, a mass of air vibrating (for example) in a cylinder bounded by a piston, the effect produced will depend upon the phase of the vibration at which the transfer of heat takes place. If heat be given to the air at the moment of greatest condensation, or be taken from it at the moment of greatest rarefaction, the vibration is encouraged. On the other hand, if heat be given at the moment of greatest rarefaction, or abstracted at the moment of greatest condensation, the vibration is discouraged".

Rayleigh's criterion can be described by the following mathematical relation,

$$\int_0^T \iiint_V \frac{\gamma - 1}{\bar{c}^2} p'(\mathbf{x}, t) Q'(\mathbf{x}, t) \, dV \, dt > \int_0^T \oiint_S p'(\mathbf{x}, t) \mathbf{u}'(\mathbf{x}, t) \cdot \mathbf{n} \, dS \, dt \tag{2.20}$$

where T is the period of excitable harmonics, V will be the combustor volume, S the boundary surface, and $\mathbf{n}$ is the normal to the surface boundary. Here, Q is intended as heat release rate per unit mass. As seen in the previous section, the flow variables can be decomposed as the sum of a mean term and a small perturbation term, e.g. $\mathbf{u} = (u, v, w) = \bar{\mathbf{u}} + \mathbf{u}'(\mathbf{x}, t)$. When Lord Rayleigh talks about *"giving or taking heat"* in his criterion, that means $Q' > 0$ or $Q' < 0$, instead $\bar{Q}$ will always be positive. The term:

$$\iiint_V \frac{\gamma - 1}{\bar{c}^2} p'(\mathbf{x}, t) Q'(\mathbf{x}, t) dV$$

on the left hand side of the previous formula represents the *acoustic driving*, the term on the right hand side, instead,

$$\oiint_S p'(\mathbf{x}, t) \mathbf{u}'(\mathbf{x}, t) \cdot \mathbf{n} dS$$

embodies the *losses* or the *acoustic damping*. So, if the acoustic driving is greater than the damping effect over a time interval, then thermoacoustic instabilities will set in. To derive the criterion in an easy and treatable way, a special set of assumptions need to be done:

1. Uniform steady state properties along the ducts that constitute the combustor.
2. Constant mean pressure (which implies zero mean flow) and temperature, although this is unrealistic for a combustor chamber.
3. The gas is inviscid and not heat conductive.
4. Oscillations are one dimensional.
5. c_p, c_v, γ are constant, which is almost valid for gas turbines combustors.
6. The fluctuations u', p', ρ', Q' are small, so to deal the with the linear theory.

With that being said, the equations for momentum and energy are respectively

$$\bar{\rho} \frac{\partial u'}{\partial t} + \frac{\partial p'}{\partial x} = 0 \tag{2.21}$$

$$\frac{\partial p'}{\partial t} + \gamma \bar{p} \frac{\partial u'}{\partial x} = (\gamma - 1)\bar{\rho} Q' \tag{2.22}$$

The first equation is multiplied by u', obtaining

$$\frac{\partial}{\partial t}\left(\frac{1}{2}\bar{\rho} u'^2\right) + u' \frac{\partial p'}{\partial x} = 0 \tag{2.23}$$

The energy equation is multiplied by $\frac{p'}{\bar{\rho}}$, resulting in

$$\frac{\partial}{\partial t}\left(\frac{1}{2\bar{\rho}} p'^2\right) + \left(\frac{\gamma \bar{p}}{\bar{\rho}}\right) p' \frac{\partial u'}{\partial x} = (\gamma - 1) p' Q' \tag{2.24}$$

where we recognize $\frac{\gamma \bar{p}}{\bar{\rho}} = \bar{c}^2$. The equation is then divided by $\bar{c}^2$

$$\frac{\partial}{\partial t}\left(\frac{1}{2\bar{\rho}\bar{c}^2} p'^2\right) + p' \frac{\partial u'}{\partial x} = \frac{(\gamma - 1)}{\bar{c}^2} p' Q' \tag{2.25}$$

These last modified equations for momentum and energy are then summed together, giving the following equation

$$\frac{\partial}{\partial t}\left(\frac{1}{2}\bar{\rho} u'^2 + \frac{p'^2}{2\bar{\rho}\bar{c}^2}\right) + \frac{\partial (u'p')}{\partial x} = \frac{(\gamma - 1)}{\bar{c}^2} p' Q' \tag{2.26}$$

Finally we integrate over the control volume of the considered system, and thanks to the Gauss's theorem, this gives

$$\frac{\partial}{\partial t} \iiint_V \left(\frac{1}{2}\bar{\rho} u'^2 + \frac{p'^2}{2\bar{\rho}\bar{c}^2}\right) dV + \oiint_S p' u' \, dS = \iiint_V \frac{\gamma - 1}{\bar{c}^2} p' Q' \, dV \tag{2.27}$$

We now define the *acoustic energy*, W,

$$W = W_{potential} + W_{kinetic} = \iiint_V \frac{p'^2}{2\bar{\rho}\bar{c}^2} \, dV + \iiint_V \frac{1}{2}\bar{\rho} u'^2 \, dV \tag{2.28}$$

If p' and Q' are in phase, with the acoustic term bigger than the acoustic losses (represented by the net flux of acoustic energy across the control surfaces), then the acoustic energy of the system will grow in time. Let us neglect the loss term and suppose that p' and Q' are defined in the following way,

$$p' = \hat{p} cos(\omega t); \quad Q' = \hat{Q} cos(\omega t + \phi) \tag{2.29}$$

where ϕ is the *phase*. Let's denote G as

$$G = \frac{1}{T} \int_0^T p' Q' \, dt \tag{2.30}$$

By substituting the previous definitions for p' and Q', we obtain:

$$G = \frac{\hat{p}\hat{Q}}{T}\int_0^T cos(\omega t)cos(\omega t + \phi)\,dt = \frac{\hat{p}\hat{Q}}{T}\int_0^T \frac{cos(2\omega t + \phi) + cos(\phi)}{2}\,dt = \\ = \frac{\hat{p}\hat{Q}}{T}\frac{T}{2}cos(\phi) = \frac{\hat{p}\hat{Q}cos(\phi)}{2} \tag{2.31}$$

Consequently, if $-90° < \phi < 90°$ there will be *acoustic driving*, vice versa if ϕ is outside this range, there will be *acoustic damping*. If $\phi \pm 90°$ no driving or damping will onset. While if $\phi = 0°$, the amplification will be maximum because p' is completely superimposed to Q' , thus the product $p' \cdot Q'$ is positive in every location.
There seems to be four general circumstances under which thermoacoustic instabilities arise in practical systems:

- sufficiently high densities of combustion energy release.
- introduction of pulses.
- unstable mean flow field or geometric configuration favourable to shedding large vortices.
- operation near the lean blowout limit of combustion.

2.3.2 Thermodynamic interpretation of the Rayleigh criterion

We can make use of a thermodynamic cycle to better explain the Rayleigh criterion [8]. Sound waves are isentropic, so in the p-v diagram a volume would advance back and forth on an isentropic line. When heat is added periodically to a gas, an increase of its specific volume v occurs. If this heat supplement is in phase with pressure oscillations, then the state of the gas volume will move clockwise around a thermodynamic cycle (please see curve 1-2'-3'-4' in figure 2.3). This series

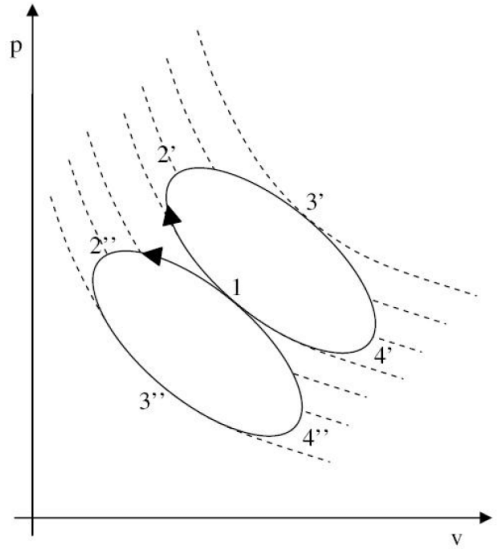

Figure 2.3: Thermodynamic interpretation of the Rayleigh criterion.

of transformations can be defined as a *thermoacoustic heat engine*, transferring mechanical energy into sound waves, and a self-excited instability could build up. If heat release fluctuations are not perfectly in phase with pressure fluctuations, the area delineated by the curve 1-2'-3'-4' will be smaller and the efficiency reduced. For the case where the heat release fluctuations are out-of-phase with pressure fluctuations, the system will move along a counterclockwise direction, see curve 1-2"-3"-4", and mechanical energy is removed from the acoustic wave. The resulting mechanical work performed by the thermodynamic cycle can be expressed as follows,

$$\oint p dv = \oint (\bar{p} + p')d(\bar{v} + v') = \oint \bar{p} dv' + \oint p' dv' = 0 + \oint p' dv \tag{2.32}$$

We now split the specific volume into an isentropic part, for which it is valid $v' = -\frac{\bar{v}dp'}{\gamma \bar{p}}$ and a second part related to the heat addiction (removal) $v'^{(Q)}$

$$\oint p' dv' = -\frac{\bar{v}}{\gamma \bar{p}} \oint p' dp' + \oint p' dv'^{(Q)} = 0 + \oint p' \frac{dv'^{(Q)}}{dt} dt \backsim \oint p' Q' dt \tag{2.33}$$

The rate of change of v' in time is proportional to heat release perturbations. We see that the work done by the *thermoacoustic engine* is positive (which corresponds to an energy addition to acoustics), if the integral $\oint p'Q'dt$ is positive over one period of oscillation, as proposed by Rayleigh. As previously stated, if the losses of acoustic energy exceed the rate of energy input to the acoustic field, provided by a fluctuating flame, a self-excited instability cannot arise, although p' and Q' are in phase. This is why the Rayleigh criterion is a necessary condition, but not sufficient, for instability to occur.

2.4 Role of hydrodynamic instabilities

Hydrodynamic instabilities are one of the possible sources that can lead to an unsteady heat release rate provided by the flame, they are generally initiated at the injector and can cause perturbations that are advected downstream at convection speeds of the order of the mean flow. When these arrive at the flame, they perturb the flame surface causing heat release rate fluctuations far downstream of the region of absolute instability. Coherent vortices, generated by these types of phenomenon, have the ability to alter combustion stability in several possible ways:

- they perturb the flame area.
- the contribute to the turbulent burning velocity.
- they cause a delay in convection from the origin of the vortices.

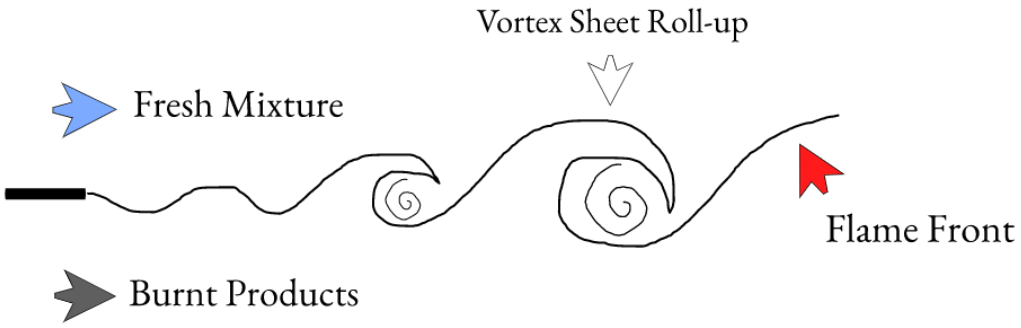

Figure 2.4: Schematic of a turbulent flame front with vortex roll-up.

In figure 2.4, the reader can see a simple schematic representing the development of a hydrodynamic instability (Kelvin-Helmholtz instability) at a flame front, separating a fresh mixture and burnt products. The vortex sheet roll-up is a periodic phenomenon, so naturally everything periodic can lead to fluctuating heat release rate.
In a general combustor, a recirculating region is required to guarantee that the flame will be stable and not blown off. From this turbulent recirculating region, a vortex shedding will establish. If the vortex shedding frequency is close to one of the natural modes of the combustor, then instability could likely be built up, and vice versa there would be a detuning.

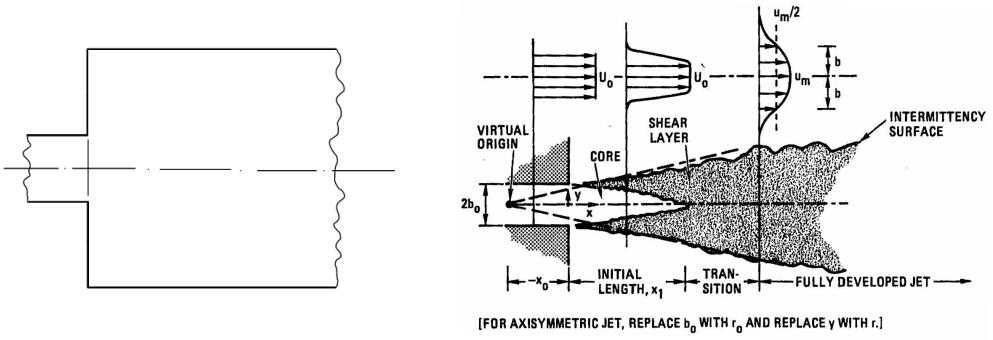

Figure 2.5: Dump Combustor (left image). Schematic of a simple non-reactant turbulent jet (right image).

In figure 2.5, a *dump combustor* is represented, it is a very simple combustor, characterized by a straight section increase that has the objective to generate a recirculating region for flame stability. It is taken as an example to illustrate the role of hydrodynamic instabilities in thermoacoustic problems. Please note that inside the duct before the section increase, *swirlers* or *bluff bodies* might be implemented to facilitate and guarantee a stable flame for more complex incoming flows, please see figure 2.6.

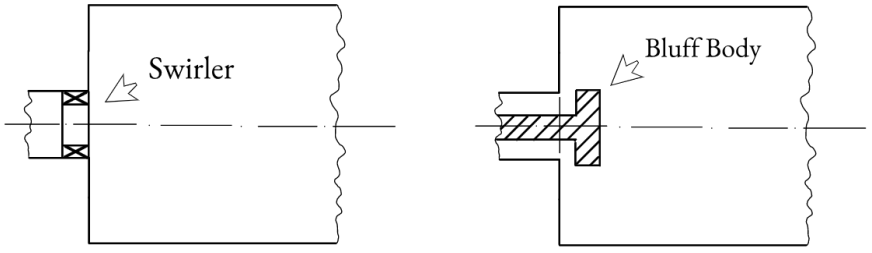

Figure 2.6: Schematic of a dump combustor with a swirler or bluff body.

Keeping the focus on the simple dump combustor, from a hydrodynamic point of view, there will be a vortex shedding starting at the intersection where the sectional area increase. This phenomenon is described by a specific initial frequency , called f_i, it depends on the characteristic velocity profile at the intersection, which in turn depends on the shape on the duct, on the turbulence level, on the initial momentum thickness θ_0, and on the jet velocity u_0. We can then introduce a non-dimensional initial frequency based on the Strouhal number,

$$St_i = \frac{f_i \theta_0}{u_0} \tag{2.34}$$

From a linear stability theory [9], the initial Strouhal number has a value around $St_i \backsim 0.017$. After this first shedding, the initial vortices will merge, grow, and be

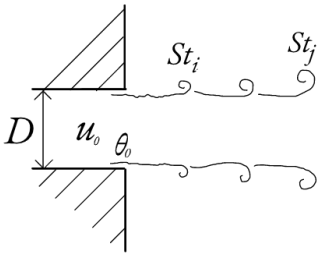

Figure 2.7: Schematics of the vortex shedding from the jet flow entering the combustion chamber.

convected downstream. So as a consequence of the merging and entrainment, the shear layer spreads and then the vortex frequency will decrease. With that being said, the shear layer will therefore be characterized by several instability frequencies associated with different sizes of the vortices. If we now focus on the end of the region of the potential core of the outgoing jet, all of this will have been merged, there will be one big vortex, governed by what is called *jet column instability*. The fluctuations in this region have another characteristic frequency, f_j, which is typically the second or third sub-harmonic of the initial shear layer frequency: $f_j \backsim \frac{f_i}{3}$. This frequency is scaled again to a Strouhal number, but with different variables:

$$St_i = \frac{f_j D}{u_0} \tag{2.35}$$

where D is the diameter of the duct before the combustion chamber. In this case, the Strouhal number is $St_j \backsim 0.25 - 0.5$. f_j is a particular frequency, if one excites the flow at this frequency, the vortices will become much more coherent, and the following spectra much sharper. So, the development of large coherent structures depends on the relationship between the acoustic frequency and the flow instability frequency. An important point to keep in mind is that imagining dealing with a non-reactant fluid, with no combustion, the vortices themselves will generate sound, but it is not that much to create a positive feedback.

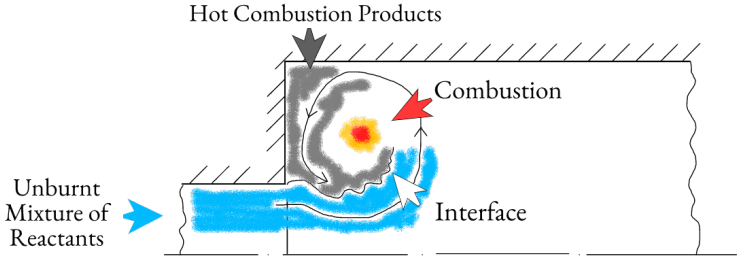

Figure 2.8: Illustration of combustion taking place after fine-scale mixing.

Looking from a combustion point of view, it is desired to have fine mixing between the "cold" fresh mixture and the hot burnt gases, that is when combustion happens. In particular, the large-scale structures will be beneficial for the enhancement of large-scale mixing also called *bulked mixing*. Nevertheless, bulk mixing may not really

intensify fine scale mixing or *molecular mixing*. Actually, only if mixing happens at a molecular level, combustion will take place. Otherwise, one will just have big pockets of air and big pockets of fuel. As a consequence, in presence of large scales structures, we still need to transition to fine-scale mixing. This is often initiated by the braids of vortices, where high strain rates between the high and low-speed streams exist, together with the small scale turbulence provided by vortex merging. When this occurs the reaction of combustion develops, characterized by a sharp heat release. One should keep in mind that this is a periodic phenomenon, vortices are convected by the mean flow, inside them there is a continuous mixing, and as soon as we reach sufficiently small scales, the mixture will then burn. This will decide the location and the moment of heat release, which then connects the feedback with acoustics. Acoustics tends to reinforce the shear layer and the coherent structures in it, which are, as explained before, strongly related to combustion, moreover some parts of the flame can add acoustic energy, while others can subtract it, what counts is the net addition. Finally, there are many other types of hydrodynamic instabilities. For example, for small steps combustors, the developing vortex downstream the jet exit can get impinged against the wall, this would bring to some kind of flapping instability, which could then combine with the Kelvin-Helmholtz instability.

2.5 Flame dynamics

2.5.1 Flame propagation

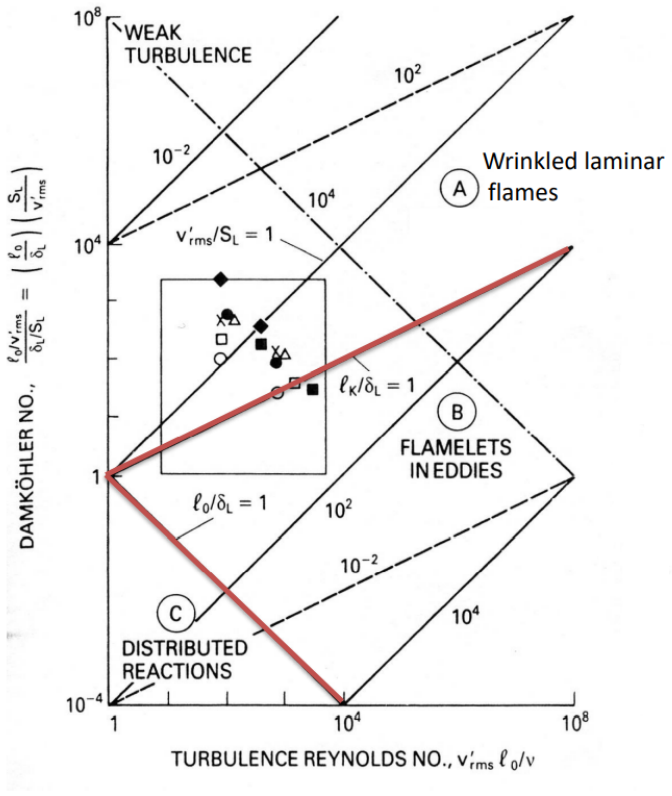

Figure 2.9: Important parameters characterizing turbulent premixed combustion. Conditions satisfying the Williams-Klimov criterion for the existence of wrinkled flames lie above the solid line $l_k = \delta_l$, and conditions satisfying the Damköhler criterion for distributed reactions fall below the solid line $l_0 = \delta_l$.

The study of dynamic models is very important for understanding the physics of combustion because they describe the interaction between heat release and the perturbations in the flames.
In order to achieve awareness about flame dynamics, it's necessary to analyze the interaction between turbulence and combustion.
It's possible to describe three different kinds of interactions:

- reaction sheets or wrinkled laminar flames;
- flamelets in eddies;
- distributed reactions.

Reaction sheets occur when the turbulence scale l_k is greater than the relative scale to combustion. Reactions develop in a range internal to the Kolmogorov scale, thus turbulence is able only to wrinkle the surface of the flame, so there's a laminar flame in a turbulent flow.

Gas turbine combustion fits in the wrinkled laminar flames due to the high Damköhler number (fast chemical reaction) together with reduced turbulence Reynolds number.
Flamelets in eddies are an intermediate state and it occurs when $l_k < \delta_L < l_0$; in this case combustion may take place inside small enough vortical structures, and the flame front is no longer continuous, and it is partially destroyed by turbulence.
Flamelets in eddies assume interest in a few applications such as some four-stroke internal combustion engines.
Distributed reactions occur when the turbulence integral length scale l_0 is smaller than the scale relative to combustion forcing turbulence time to be larger than the chemical one. This fact implies that chemical kinetics is influenced by the features of the flow. The flame front doesn't exist.
Distributed reactions are less used for engineering applications since they require high flow velocities in pipes with small diameters, generating unacceptable losses, in addition they are very hard to model because of the strong interaction between chemical and turbulent reactions.

2.5.2 Flame and acoustic waves in combustion system in CFD

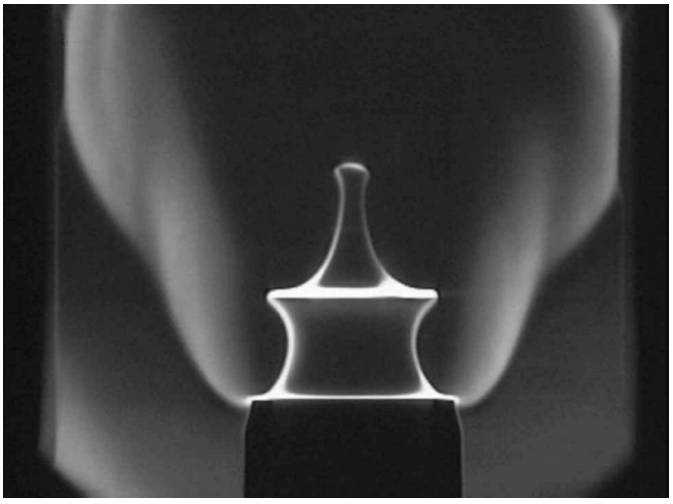

Figure 2.10: Photograph of flame disturbances generated by acoustic velocity oscillations, courtesy of [10].

Some of the many mechanisms of flame–acoustics interaction are listed below:

- flame front kinematics, which relates to the distortion and perturbation of the flame area;
- flame speed modifications, caused by an alteration of the incoming turbulence intensity, which consequently influence the heat release rate;
- equivalence ratio perturbations, due to fluctuations of velocity or pressure, which then alter the heat of reaction ΔH.

It's easy to understand that the interactions between flames and acoustic waves are very difficult to predict, model and test.
To make a correct numerical simulation, it's necessary to know the flame shape and its position, since there is a deep dependence of the unsteady phenomena on the interaction between turbulence and the flame fronts.
In this way, it's possible to define a model able to properly describe the interplay between flames and acoustic waves occurring in the combustion system.
As an interesting example, figure 2.11, reports the results of a direct numerical simulation (DNS) that investigates the interaction between acoustic waves and a flame, localizing the flame front thanks to isolevels of heat release.

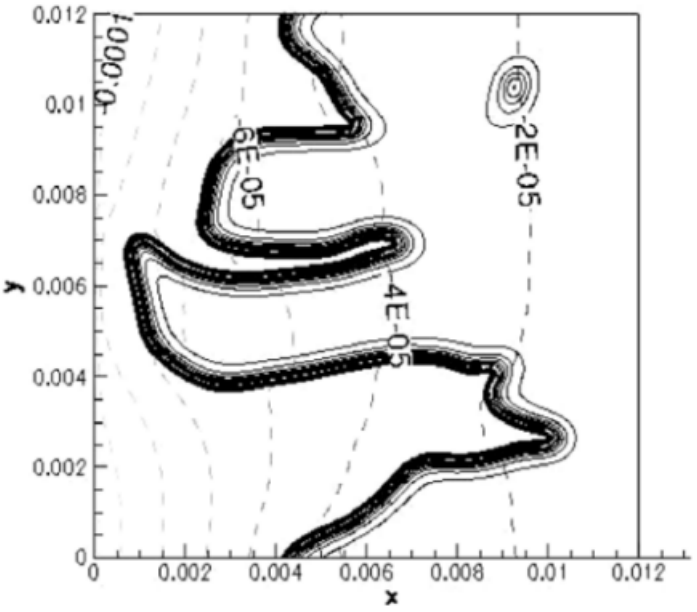

Figure 2.11: Acoustically-induced pressure fluctuation (dashed lines). The instantaneous position of the flame front is shown with isolevels of heat release (black solid lines).

However, there are two main problems. The first is related to the fact that a model that doesn't consider the integral length scales isn't a good predictor of the flame front, because of their strong influence on the phenomenon. CFD allows to investigate many thermoacoustic instability problems, which are difficult and extremely expensive to test experimentally. But at the same time, performing Large Eddy Simulations (LES) or DNS require large computational time and resources.
Up to this point, the interest of the scientific community is moving more and more in the direction of defining good transfer functions, in order to find a relation that easily describes this difficult thermoacoustic interaction.

2.5.3 Flame transfer functions

A system can be generally defined using a mathematical relationship, called transfer function, which is a mathematical model that relates and predicts the output of the system for each possible input.
The flame dynamic response to a perturbation can be represented by a **Flame Transfer Function (FTF)** , which relates the heat release rate fluctuations to the velocity oscillations at a reference location upstream of the flame (for instance at the exit of the injection system). As a matter of fact, for turbulent premixed flames, the direct influence of pressure, temperature, and density variations on the heat release rate is usually considered to be small. Taking into account that lean-premixed flames are particularly prone to combustion instabilities, since their rate of heat release Q is very sensitive to acoustic perturbations, it is interesting to relate this physical aspect with a mathematical model in order to predict the thermoacoustic interaction.
That being the case, the flame frequency response or flame transfer function is defined as the ratio of heat release rate and velocity fluctuations (or pressure fluctuations), which are typically normalized with their mean values.
This completely characterizes the dynamic response of a flame to acoustic perturbations, leading to the following expression:

$$F(\omega) \equiv \frac{\dot{Q}'/\bar{\dot{Q}}}{u'/\bar{u}} \tag{2.36}$$

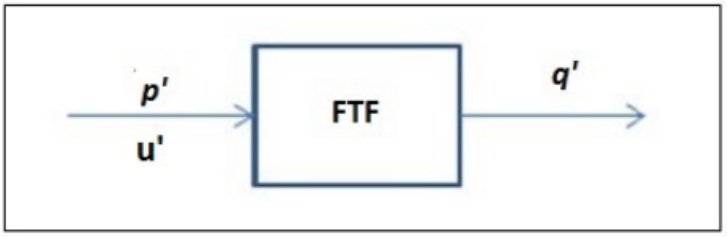

Figure 2.12: Flame Transfer Function approach.

In particular, for a turbulent premixed flame, the heat release rate can be expressed as:

$$\dot{Q} = \rho_u \cdot A \cdot S \cdot \Delta H \tag{2.37}$$

where ρ_u is the unburnt gas density, A is the flame surface area, S is the turbulent burning velocity or turbulent flame speed, and ΔH is the heat of reaction per unit mass. The burning velocity S is defined by different flow quantities, such as laminar flame speed S_L, the length scale of turbulent fluctuations, chemical species and it can be also written as a function of dimensionless quantities [11].
From equation 2.36 various comprehensive criteria have been introduced. The validation of a model is in practice often challenging, this is due to the fact that many parameters can not be selected from first principles. Instead, parameters must be adjusted to match experimental or numerical data. In recent years, detailed laser diagnostic studies in gas turbine combustors have significantly contributed to a better understanding of phenomena like flame stabilization, combustion instabilities,

pollutant formation and finite-rate chemistry effects.
Let us first consider a general FTF that correlates the normalized heat release fluctuations relative fluctuations $\dot{Q}'/\dot{\bar{Q}}$ with N quantities G_i that could have influence on it, together with N weights k_i, with $i = 1...N$:

$$\frac{\dot{Q}'}{\dot{\bar{Q}}} = k_1 \frac{G_1'}{\bar{G}_1} + k_2 \frac{G_2'}{\bar{G}_2} + ... + k_i \frac{G_i'}{\bar{G}_i} + ... + k_N \frac{G_N'}{\bar{G}_N} \tag{2.38}$$

where it can be assumed that:

$$\lim_{\omega \to 0} \sum_{i=1}^{N} k_i = K \tag{2.39}$$

The last equation is an easy way to verify the validity of any transfer function, where K satisfies the quasi-steady limit deducible from global conservation laws.
Adopting a flame model leads to many difficulties because too many parameters need to be taken into account simultaneously, moreover they are correlated only by one equation, like 2.39. To overcome this issue, several simplified models have been developed considering only the most pertinent quantities and neglecting all the others.
Experimental analysis is extremely complex since it is very hard to get a good instrumentation of a critical flow field (temperatures are very high) and to get measurement of certain quantities like heat release fluctuations. This is why nowadays researcher, as stated before, count mostly on numerical simulations, that can grant a better comprehension of the flame-acoustics interaction.
As a consequence, few empirical models remain, some of them are briefly listed below:

- The flame kinematics is independent of the flow field, and as a first approximation, taking into account this aspect leads to a very useful model as follows:

$$\frac{\dot{Q}'}{\dot{\bar{Q}}} = 0 \tag{2.40}$$

- The heat release rate is proportional to mass flow rate perturbation, sampled in section i:

$$\frac{\dot{Q}'}{\dot{\bar{Q}}} = \frac{\dot{m}_i'}{\dot{\bar{m}}_i} \tag{2.41}$$

- Crocco's model:

$$\frac{\dot{Q}'}{\dot{\bar{Q}}} = -k \cdot \frac{\dot{m}_i'}{\dot{\bar{m}}_i} \cdot e^{i\omega\tau} \tag{2.42}$$

  where k is a constant interaction index, which represents a dimensionless parameter of proportionality between the heat release fluctuations and the mass flow fluctuations, andτ is a specific time lag.

- A model that simulates a 3D flame surface through the parameter τ:

$$\frac{\dot{Q}'}{\dot{\bar{Q}}} = k \cdot \frac{\Phi_i'}{\bar{\Phi}_i} = -k \cdot \frac{u_i'}{\bar{u}_i} \cdot \frac{sin(\omega \Delta T)}{\omega \Delta T} \cdot e^{i\omega\tau} \tag{2.43}$$

- Finally, the most complete model, which takes into account several dependencies, although it's hard to calibrate since it has many degrees of freedom:

$$\frac{\dot{Q}'}{\bar{\dot{Q}}} = k_p \cdot \frac{p_i'}{\bar{p}_i} \cdot e^{i\omega\tau_p} + k_u \cdot \frac{u_i'}{\bar{a}_i} \cdot e^{i\omega\tau_u} + k_v \cdot \frac{v_i'}{\bar{a}_i} \cdot e^{i\omega\tau_v} + k_w \cdot \frac{w_i'}{\bar{a}_i} \cdot e^{i\omega\tau_w} \tag{2.44}$$

Crocco's theorem (2.8) is one of the most important flame models and a sort of milestone in transfer function evolution since it represents the delay time of perturbations from a reference point to the flame sheet.
It is largely employed to study combustion instabilities in liquid-propellant rocket engines. The model globally describes the dynamic relationship between fuel injection and heat release; the major difficult is to choose accurately the parameters k and τ, otherwise the results will be incorrect.
At a general time t, the pressure in the chamber suddenly decreases, causing an increase in the fuel flow through the injector. The fuel mass burns later, $t + \tau$, where τ is the time delay. Some quantities contribute to improve the time delay, they're related to the convection time needed to travel the spatial gap from the fuel injection location to the flame front, the mixing time for fresh air and fuel to mix with hot product gases, and the chemical time corresponding to the ignition delay.
This model can be applied with the hypothesis to consider a flat thin flame, more in detail the flame thickness δ_L has to be much less than wavelength λ.
Below, are reported the limits of this model in order to assure to have correct results, the subscript "ac" means acoustic waves and the other one "cv" means convective waves:

$$\lambda_{ac} = \frac{c_s}{f} \Longrightarrow f \ll \frac{c_s}{\delta_L} \approx \frac{800\,m/s}{2\,cm} = 40\,kHz \tag{2.45}$$

$$\lambda_{cv} = \frac{\bar{u}}{f} \Longrightarrow f \ll \frac{\bar{u}}{\delta_L} \approx \frac{20\,m/s}{2\,cm} = 1\,kHz \tag{2.46}$$

So if frequency $\omega \ll 1\,kHz$ the hypotesis of thin flame is respected and the model can be used as a good approximation, otherwise if the flame is too distributed into a 3D surface (figure 2.13), this model isn't a good choice.

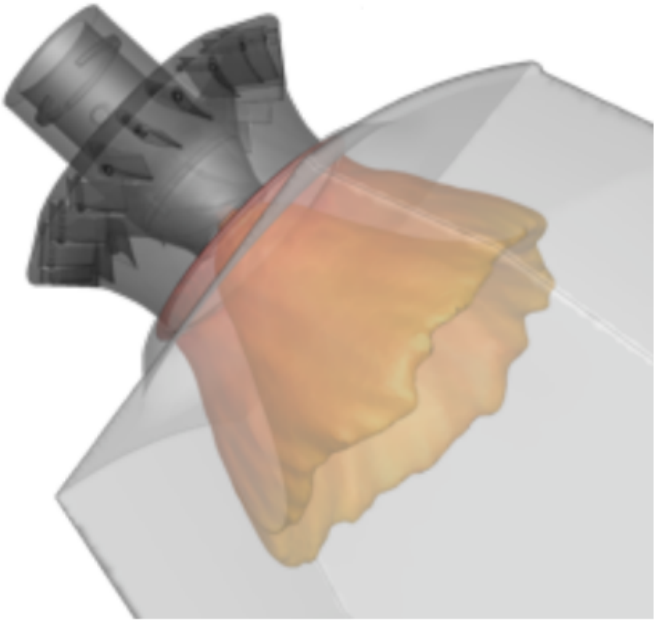

Figure 2.13: Three-dimensional flame surface, LES simulation.

In the last years, many flame frequency response models have been developed and they take into account small oscillation amplitudes. This implementation is not hard, because these models are often written as a linear superposition of different contributions from the flame and acoustic interaction.
On the other hand, the main issue is to validate these models, because there are many difficulties related to experimental measurements.
Another possibility is to extract the flame frequency responses from computational fluid dynamics results (CFD data), in fact, the numerical simulations have the power to take into account flame and acoustic interactions.

3 Linear and nonlinear stability analysis

3.1 Introduction

Before addressing the objective of this work, it is advised to recover some basic definitions of linear and nonlinear stability analysis.
A system is defined as **linearly stable** if any small amplitude disturbance (as small as one wants) decays with time; vice versa if it grows, the system is told to be linearly unstable. Within a linear framework, in the event of an instability, the perturbations will grow exponentially, till nonlinearities become effective and consequently a limit cycle could be reached, meaning that the oscillations would saturate.

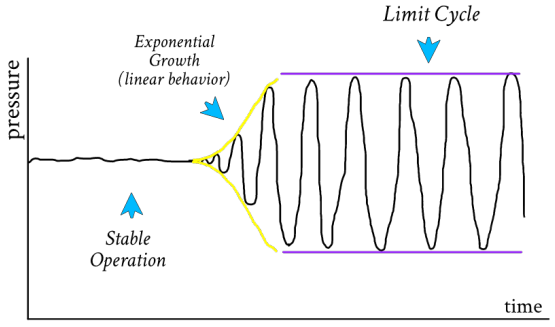

Figure 3.1: Linear instability with succeeding limit cycle.

A system is defined as **nonlinearly unstable** if some finite amplitude disturbance grows with time. In this case, for triggering instability, the initial amplitude should be greater than a *threshold amplitude*, as a consequence there is a clear dependence on initial conditions.

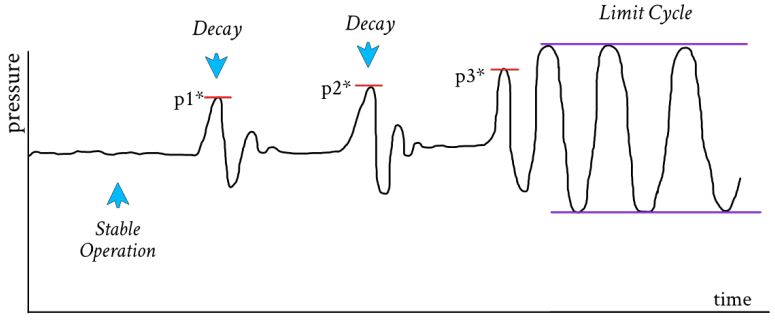

Figure 3.2: Nonlinear instability with decays and succeeding limit cycle.

3.2 Linear analysis

3.2.1 Setting the eigenproblem

Let's consider the evolution of a system described by the following expression.

$$\frac{\mathrm{d}\mathbf{x}}{\mathrm{d}t} = \mathbf{f}[\mathbf{x}(t), t; r] \tag{3.1}$$

where $\mathbf{x}$ is the state vector (N components, column vector), $\mathbf{f}$ is the evolution function (another N-column vector), t is time and r is a control parameter. From here on, only autonomous systems will be considered, where the evolution function doesn't depend on time.

$$\frac{\mathrm{d}\mathbf{x}}{\mathrm{d}t} = \mathbf{f}[\mathbf{x}(t); r] \tag{3.2}$$

We now want to predict the asymptotic behaviour of the system, that means time goes to infinite, as a function of the initial conditions and the control parameter. The state vector is now considered as sum of a base state vector $\bar{\mathbf{x}}$ (please note that the overbar denotes a time mean), and a perturbation $\mathbf{x}'(t)$, multiplied for a small amplitude ϵ.

$$\mathbf{x} = \bar{\mathbf{x}} + \epsilon\mathbf{x}'(t) \tag{3.3}$$

So that they respectively satisfy:

$$\frac{\mathrm{d}\bar{\mathbf{x}}}{\mathrm{d}t} = \mathbf{f}[\bar{\mathbf{x}}(t); r] \qquad \frac{\mathrm{d}\mathbf{x}'}{\mathrm{d}t} = \mathbf{A}\mathbf{x}'(\mathbf{t}) \tag{3.4}$$

where $\mathbf{A}$ is the Jacobian matrix of the coefficients (NxN). It comes from the substitution of the new definition of the state vector inside the previous formulation, followed by a Taylor expansion to second order:

$$\frac{\mathrm{d}\bar{\mathbf{x}}}{\mathrm{d}t} + \epsilon\frac{\mathrm{d}\mathbf{x}'}{\mathrm{d}t} = \mathbf{f}[\bar{\mathbf{x}} + \epsilon\mathbf{x}'] = \mathbf{f}(\bar{\mathbf{x}}) + \epsilon \left.\frac{\partial\mathbf{f}}{\partial\mathbf{x}}\right|_{\bar{\mathbf{x}}} \mathbf{x}' + O(\epsilon^2) \tag{3.5}$$

where we call $\mathbf{A} = \left.\frac{\partial\mathbf{f}}{\partial\mathbf{x}}\right|_{\bar{\mathbf{x}}}$.

The focus is on the **perturbed system**. We first expand the perturbation vector $\mathbf{x}'$ with the aim of setting an eigenvalue problem.

$$\mathbf{x}'(t) = \mathbf{x}'(0) + t \left.\frac{\mathrm{d}\mathbf{x}'}{\mathrm{d}t}\right|_{t=0} + \frac{t^2}{2} \left.\frac{\mathrm{d}^2\mathbf{x}'}{\mathrm{d}t^2}\right|_{t=0} + ... \tag{3.6}$$

$$\frac{\mathrm{d}\mathbf{x}'}{\mathrm{d}t} = \mathbf{A}\mathbf{x}'; \quad \frac{\mathrm{d}^2\mathbf{x}'}{\mathrm{d}t^2} = \mathbf{A^2}\mathbf{x}'; \quad \frac{\mathrm{d}^3\mathbf{x}}{\mathrm{d}t^3} = \mathbf{A^3}\mathbf{x}'; \quad ... \quad \frac{\mathrm{d}^n\mathbf{x}'}{\mathrm{d}t^n} = \mathbf{A^n}\mathbf{x}' \tag{3.7}$$

Resulting in

$$\mathbf{x}'(t) = \mathbf{x}'(0) + t\mathbf{A}\mathbf{x}'(0) + \frac{t^2}{2}\mathbf{A^2}\mathbf{x}'(0) + ... = \sum_{n=0}^{+\infty} \frac{t^n\mathbf{A^n}}{n!}\mathbf{x}'(0) \tag{3.8}$$

We define the analytic function of the matrix

$$e^{\mathbf{A}t} = \sum_{n=0}^{+\infty} \frac{t^n \mathbf{A}^{\mathbf{n}}}{n!} \tag{3.9}$$

and finally, the solution of the disturbance problem is obtained.

$$\mathbf{x}'(t) = e^{\mathbf{A}t}\mathbf{x}'(0) \tag{3.10}$$

3.2.2 Left and right eigenvectors

For the purpose of assessing the stability of the system it is useful to decompose the matrix $\mathbf{A}$ in the sum of products of left and right eigenvectors. We name λ_k the N eigenvalues of the matrix $\mathbf{A}$, they are the solution of the characteristic equation:

$$det(\mathbf{A} - \lambda_k \mathbf{I}) = 0 \tag{3.11}$$

where $\mathbf{I}$ is the identity matrix. For each eigenvalue λ_k there exist an eigenvector such that

$$\mathbf{A}\mathbf{u}_k = \lambda_k \mathbf{u}_k \tag{3.12}$$

$\mathbf{u}_k$ is called a right eigenvector. If λ_k is complex then $\mathbf{u}_k$ has complex entries. The left eigenvectors $\mathbf{v}_k$ are non-trivial solutions, defined up to an arbitrary factor of the system

$$\mathbf{v}_k^T \bar{\mathbf{A}} = \bar{\lambda}_k \mathbf{v}_k^T \tag{3.13}$$

The reader can note from the previous definitions that, the left eigenvectors $\mathbf{v}_k$ of matrix $\mathbf{A}$ are also the right eigenvectors of the conjugate transpose of $\mathbf{A}$:

$$\bar{\mathbf{A}}_k^T \mathbf{v}_k = \bar{\lambda}_k \mathbf{v}_k \tag{3.14}$$

3.2.3 The adjoint matrix

We first give a definition of the scalar product between two vectors (in general complex):

$$(\mathbf{u}_k, \mathbf{v}_k) \equiv \bar{\mathbf{u}}_k^T \mathbf{v}_k \tag{3.15}$$

The adjoint matrix can be expressed as follows:

$$(\mathbf{A}\mathbf{u}, \mathbf{v}) = \overline{\mathbf{A}\mathbf{u}}^T \mathbf{v} = \bar{\mathbf{u}}^T \bar{\mathbf{A}}^T \mathbf{v} = (\bar{\mathbf{u}}, \mathbf{A}^T \mathbf{v}) \tag{3.16}$$

From which we call $\mathbf{A}^\dagger \equiv \bar{\mathbf{A}}^T$ the **adjoint matrix**. If $\mathbf{A} = \mathbf{A}^\dagger$ the matrix $\mathbf{A}$ is self-adjoint. For this peculiar case, the matrix $\mathbf{A}$ results real and symmetric, the eigenvalues are real, and the eigenvectors form an orthogonal base. Moreover, left and right eigenvectors coincide. A non-self-adjoint matrix has usually complex eigenvalues, plus its conjugates.
Eigenvectors are stated as orthogonal if their scalar product results: $(\mathbf{u}_h, \mathbf{v}_k) = a\delta_{hk}$, where δ_{hk} is the Kronecker delta, and a is some amplitude coefficient. If a it's equal to one, the eigenvectors are then *orthonormalized*.

3.2.4 Modal analysis and the L propagator

Let us feature the N eigenvalues as distinct and the eigenvectors as linearly independent (so as to form a basis). At t = 0 we have: $\mathbf{x}'(0) = \sum_{k=1}^{N} \mathbf{u}_k c_k$.

$$(\mathbf{v}_h, \mathbf{x}'(\mathbf{0})) = \sum_{k=1}^{N} (\mathbf{v}_h, \mathbf{u}_k c_k) = \sum_{k=1}^{N} c_k (\mathbf{v}_h, \mathbf{u}_k) = c_k (\mathbf{v}_h, \mathbf{u}_h) \tag{3.17}$$

Whence we end in

$$c_k = \frac{(\mathbf{v}_h, \mathbf{x}'(\mathbf{0}))}{(\mathbf{v}_h, \mathbf{u}_h)} \tag{3.18}$$

Assuming the eigenvectors are orthonormalized, then $c_k = (\mathbf{v}_k, \mathbf{x}'(\mathbf{0}))$ can be expressed as follows

$$\mathbf{x}'(\mathbf{0}) = \sum_{k=1}^{N} \mathbf{u}_k (\mathbf{v}_k, \mathbf{x}'(\mathbf{0})) = \sum_{k=1}^{N} \mathbf{u}_k \bar{\mathbf{v}}_k^T \mathbf{x}'(\mathbf{0}) = \mathbf{I}\mathbf{x}'(\mathbf{0}) \tag{3.19}$$

So, assuming $\mathbf{x}'(\mathbf{0})$ to be any kind of vector, one can retrieve the identity matrix from

$$\mathbf{I} = \sum_{k=1}^{N} \mathbf{u}_k \bar{\mathbf{v}}_k^T \tag{3.20}$$

The matrix $\mathbf{A}$ can then be represented as

$$\mathbf{A} = \mathbf{A}\mathbf{I} = \sum_{k=1}^{N} \mathbf{A}\mathbf{u}_k \bar{\mathbf{v}}_k^T = \sum_{k=1}^{N} \lambda_k \mathbf{u}_k \bar{\mathbf{v}}_k^T \tag{3.21}$$

that means, assuming linearly independent eigenvectors and distinct eigenvalues, that the matrix $\mathbf{A}$ can be expressed as the sum of the product of eigenvalues and eigenvectors, this type of analysis is called *modal analysis*. We now name $\mathbf{U}$ the matrix containing in its columns the N right eigenvectors of $\mathbf{A}$, and $\mathbf{V}$ the matrix containing in its columns the N left eigenvectors of $\mathbf{A}$, considering again the eigenvalues to be distinct.
When the eigenvectors are orthonomal:

$$(\mathbf{v}_h, \mathbf{u}_k) = \delta_{hk} \quad \rightarrow \quad \bar{\mathbf{v}}_h^T \mathbf{u}_k = \delta_{hk} \quad \rightarrow \quad \bar{\mathbf{V}}^T \mathbf{U} = \mathbf{I} \tag{3.22}$$

If now one examines the next product

$$\bar{\mathbf{v}}_h^T \mathbf{A}\mathbf{u}_k = \lambda_k \bar{\mathbf{v}}_h^T \mathbf{u}_k = \lambda_k \delta_{hk} \tag{3.23}$$

Consequently

$$\bar{\mathbf{V}}^T \mathbf{A}\mathbf{U} = \mathbf{\Lambda} \quad \rightarrow \quad \mathbf{A} = \mathbf{U}\mathbf{\Lambda}\bar{\mathbf{V}}^T \tag{3.24}$$

with $\mathbf{\Lambda}$ the diagonal matrix of the eigen values of $\mathbf{A}$.
Going back to the problem for the perturbed system:

$$\frac{\mathrm{d}\mathbf{x}'}{\mathrm{d}t} = \mathbf{A}\mathbf{x}'(t) \tag{3.25}$$

let us take $\mathbf{x}'(t) = \mathbf{U}\mathbf{q}(t)$, hence $\frac{\mathrm{d}\mathbf{x}'}{\mathrm{d}t} = \mathbf{U}\dot{\mathbf{q}}$.
Therefore

$$\mathbf{U}\dot{\mathbf{q}} = \mathbf{A}\mathbf{U}\mathbf{q} \quad \rightarrow \quad \dot{\mathbf{q}} = \mathbf{U}^{-1}\mathbf{A}\mathbf{U}\mathbf{q} \quad \rightarrow \quad \dot{\mathbf{q}} = \mathbf{\Lambda}\mathbf{q} \tag{3.26}$$

as result, we obtain

$$\mathbf{q}(t) = e^{\mathbf{\Lambda}t}\mathbf{q}(0) = \mathbf{U}^{-1}\mathbf{x}' = e^{\mathbf{\Lambda}t}\mathbf{U}^{-1}\mathbf{x}'(0) \tag{3.27}$$

By substituting the previous definition for $\mathbf{q}$(t), we get to the solution

$$\mathbf{x}'(t) = \mathbf{U}e^{\mathbf{\Lambda}t}\mathbf{U}^{-1}\mathbf{x}'(0) = \mathbf{U}e^{\mathbf{\Lambda}t}\bar{\mathbf{V}}^T\mathbf{x}'(0) \tag{3.28}$$

We now define the *propagator* $\mathbf{L} = \mathbf{U}e^{\mathbf{\Lambda}t}\bar{\mathbf{V}}^T$.

3.2.5 Stability conditions

Retrieving the definition for matrix $\mathbf{A}$

$$\mathbf{A} = \sum_{k=1}^{N} \lambda_k \mathbf{u}_k \bar{\mathbf{v}}_k^T \tag{3.29}$$

One can calculate $\mathbf{A}^2$ as follows

$$\begin{aligned}\mathbf{A}^2 = \sum_{k=1}^{N} \lambda_k \mathbf{u}_k \bar{\mathbf{v}}_k^T \sum_{h=1}^{N} \lambda_h \mathbf{u}_h \bar{\mathbf{v}}_h^T = \sum_{k=1}^{N}\sum_{h=1}^{N} \lambda_k\lambda_h \mathbf{u}_k \bar{\mathbf{v}}_k^T \mathbf{u}_h \bar{\mathbf{v}}_h^T = \ldots \\ = \sum_{k=1}^{N}\sum_{h=1}^{N} \lambda_k\lambda_h \mathbf{u}_k \delta_{hk} \bar{\mathbf{v}}_h^T = \sum_{k=1}^{N} \lambda_k^2 \mathbf{u}_k \bar{\mathbf{v}}_k^T\end{aligned} \tag{3.30}$$

This is consequently valid also for $\mathbf{A}^n = \sum_{k=1}^{N} \lambda_k^n \mathbf{u}_k \bar{\mathbf{v}}_k^T$. The matrix $\mathbf{A}^n$ has the same eigenvectors as $\mathbf{A}$, and as eigenvalues λ_k^n.
In general, for a linear combination of powers of $\mathbf{A}$ named g we have:

$$g(\mathbf{A}) = \sum_{k=1}^{N} g(\lambda_k) \mathbf{u}_k \bar{\mathbf{v}}_k^T \tag{3.31}$$

and in particular, for the exponential of a matrix one has:

$$e^{\mathbf{A}} = \sum_{k=1}^{N} e^{\lambda_k} \mathbf{u}_k \bar{\mathbf{v}}_k^T \tag{3.32}$$

As a result, the solution for the linear problem reads also

$$\mathbf{x}'(t) = e^{\mathbf{A}t}\mathbf{x}'(0) = \sum_{k=1}^{N} e^{\lambda_k t}\mathbf{u}_k(\mathbf{v}_k, \mathbf{x}'(\mathbf{0})) = \sum_{k=1}^{N} e^{\lambda_k t}\mathbf{u}_k c_k \tag{3.33}$$

The reader can see that the left eigenvectors weigh the initial conditions.
The main objective of this demonstration is that the eigenvalues λ_k determine the asymptotic behaviour (time goes to infinite) of the perturbed system.
The λ_k are generally complex numbers, so they can be seen as

$$\lambda_k = \alpha_k + i\omega_k \tag{3.34}$$

where the real part α_k is named *growth rate*, and the imaginary part ω_k *angular frequency*. Therefore, if we consider an autonomous system, with the evolution matrix **A** and N distinct eigenvalues. The system is told to be:

- **Asymptotically stable** if all eigenvalues of a have negative real part.
- **Marginally stable** if one (or more) eigenvalues have real part equal to zero (and the others have negative real part).
- **Unstable** if at least one eigenvalue has real part larger than zero.

The aforementioned theory refers to [12].

3.3 Non-normality and transient growth

Keeping the focus on the perturbed system

$$\frac{\mathrm{d}\mathbf{x}'}{\mathrm{d}t} = \mathbf{A}\mathbf{x}'(t) \tag{3.35}$$

it is said to be **non-normal** when its evolution operator **A** doesn't commute with its adjoint $\mathbf{A}^\dagger$:

$$\mathbf{A}\mathbf{A}^\dagger \neq \mathbf{A}^\dagger\mathbf{A} \tag{3.36}$$

That means that the thermoacoustic interaction will be non-normal. The reader should also notice that for some problems the boundary conditions can bring some non-normality in the operator, even the heat release rate from the combustion process can do that. Non-normality is always verified if the eigenvectors of the thermoacoustic system are non-orthogonal.
This property of the system can lead to **transient growth** of oscillations, even when the eigenvalues indicate linear stability, please see figure 3.4. This eventuality could

prompt thermoacoustic instability in a non-normal combustion system, since perturbations can linearly and transiently grow away from the steady base flow and eventually grow transiently around an unstable periodic solution. That being the case, individual eigenvalues are the wrong tool to analyze a non-normal system at intermediate times, because they return the asymptotic stability of the system. In the modal analysis, we look at the growth rate of each mode, if it's stable or unstable. The concept of transient growth is that one can have every mode stable, but in the transient time, there is still some growth, figure 3.3.

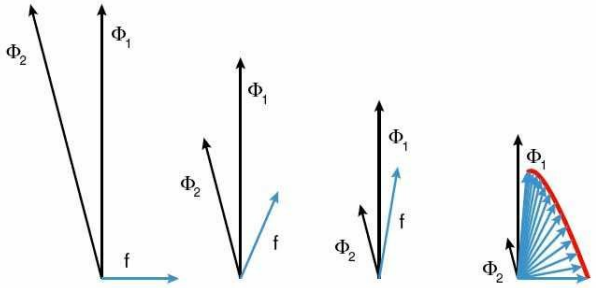

Figure 3.3: Vector representation of transient growth. The magnitude of $\mathbf{f} = \mathbf{\Phi_1} - \mathbf{\Phi_2}$ *intensify before diminishing to zero as the two* Φ_1 *and* Φ_2 *decay (courtesy of Schmid, 2007).*

It should be emphasized that non-normality can give transient growth with the correct initial conditions. The initial disturbance is generally projected over all the eigenvectors, but if its projection is just over one of them, even a non-normal system does not experience growth transiently in time.
We conclude this subsection by mentioning that it's often interesting to determine the specific condition that achieves the maximum energy amplification. It is generally done by computing a *singular value decomposition* (SVD) of the evolution operator **A** or by adopting a more general method, which is the *Lagrange multiplier technique*, that seeks the extreme of a specific functional.

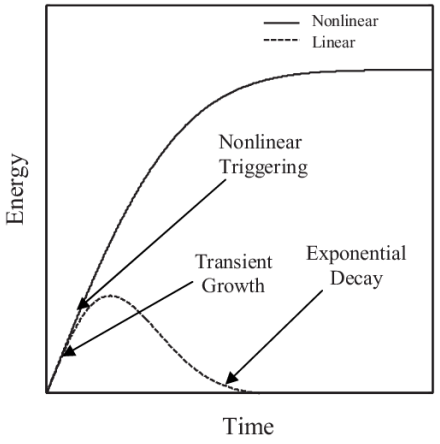

Figure 3.4: Schematic of linear and nonlinear evolutions of the acoustic energy for a Rijke tube [13].

3.4 Sensitivity analysis and bootstrapping

Once introduced the definition of a non-normal system, we briefly report another type of analysis: the *non-modal stability analysis*. It is the description of disturbance behavior governed by a linear non-normal evolution operator. This technique describes the complete dynamics of the flow as a superposition of many eigensolutions. An important aspect of this type of approach is the **sensitivity analysis**, which consists of a perturbation of the system matrix **A** by a random matrix **E**. In a real case, this could be caused by disturbances in the boundary conditions or by a noisy base flow, and it will produce perturbations in both the eigenvalues and the eigenvectors. In particular, we can define $\mathbf{z}$ as an ϵ-pseudoeigenvalue of **A** if it satisfies $\|(\mathbf{zI} - \mathbf{A})^{-1}\| > \epsilon^{-1}$, where ϵ is a small quantity that depends on the system itself.

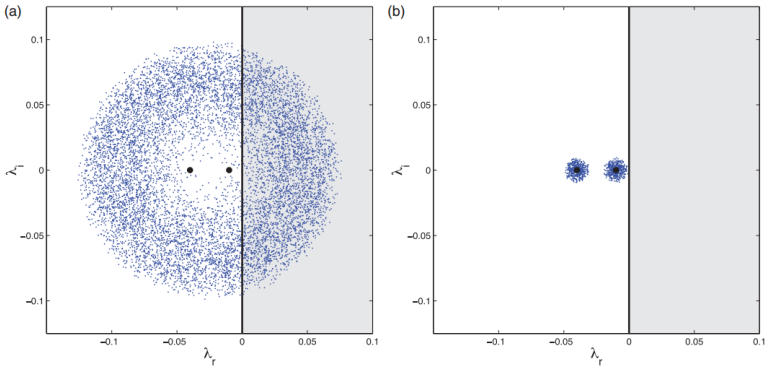

Figure 3.5: Sensitivity analysis for (a) a non-normal system, and (b) a normal system [14].

Displaying in the complex plane the set of all eigenvalues which are ϵ-close to **A**, returns the ϵ-pseudospectrum of **A**. If the contours of the spectrum protrude into the right half of the plane (that means positive growth rate), the system might exhibit transient growth. That is in fact, a necessary condition for transient growth. Moreover, we conclude assessing that a marked sensitivity of the eigenvalues is a first indication of non-normality. In figure 3.5, are presented two cases for a non-normal fig. 3.5a and normal system fig. 3.5b perturbed by random matrices of norm 10^{-2}. The black dots represent the eigenvalues for the unperturbed system, the blue ones are for the perturbed system. The reader can see that for a non-normal system perturbations have large effect on the eigenvalues, and subsequently could exceed the stability limit. On the other hand, for a normal system the displacement of the eigenvalues is bounded by the size of the perturbation.
Another extension of non-modal analysis is **bootstrapping**. This concept arises from the possibility for the transient amplification to reach sufficiently large values to trigger nonlinear effects. If the initial amplitude surpasses a critical value, nonlinear effects will pull the system towards a non-zero steady state. Specifically, the nonlinear terms present in a nonlinear system, which do not produce energy by themselves, redistribute the energy of the system from decaying directions to transiently growing ones. Thus harvesting the full potential for transient growth by a nonlinear mechanism, that is bootstrapping [14].

3.5 Nonlinear analysis

In nature, as well as in engineering, many phenomena have a nonlinear behaviour and these appear commonly to be chaotic, unpredictable or counterintuitive. This attitude may resemble a random behaviour, but it's absolutely not. This is due to nonlinear phenomena, which are complex to analyze because most of nonlinear systems are impossible to solve analytically. For this reason, nonlinear systems are commonly approximated by linear equations, this operation is defined as *linearization*. This works well up to some level of accuracy and some range of the input values, although some interesting phenomena such as chaos and singularities can be hidden by linearization. The essential difference between linear and nonlinear systems is that the first ones can be decomposed into two parts, each part can be solved separately and finally recombined together to get the answer. This is a powerful tool to study and predict a lot of phenomena, but unfortunately many things in nature do not act in this way [15]. Combustion instability is also a typical nonlinear phenomenon. Linear techniques can predict whether a thermoacoustic system is stable or unstable, but as previously said, when the amplitude of an infinitesimal perturbation becomes so large that the nonlinear behavior overwhelms the linear one, the typical consequence is that the system reaches a constant amplitude periodic solution, known as *stable limit cycle*. In this case, a nonlinear analysis is required for predicting and evaluating the self-sustained oscillations and limit cycle amplitudes.

3.5.1 Source of nonlinearity in thermoacoustics

In gas turbine systems, both the pressure perturbations and the velocity perturbations are related to the mean pressure and to the speed of sound, respectively. Also, the mean flow velocity is minor compared to the speed of sound. As a consequence, second and higher-order terms involving the mean flow Mach number and perturbation Mach number in the nonlinear gas dynamic equations are negligible [16]. In the framework of thermoacoustics, the possible sources of nonlinearity come from:

- nonlinear gasdynamics
- nonlinear damping
- nonlinear heat release rate

The third source is generally a function of pressure and velocity fluctuations, the latter has the strongest influence on heat release fluctuations. One should also remember that thermoacoustic nonlinearities are not energy-conserving. The main cause of nonlinearity in gas turbine combustors is the nonlinear behavior of the unsteady heat release rate coming from the flames. Generally, it is possible that acoustic waves can interact with entropy or vorticity waves. However, when the unsteady perturbations are small the acoustics can be approximated to behave independently from entropy and vorticity, except for the boundaries and at the zones of heat release [17]. Acoustic waves could also be generated by the acceleration of entropy waves in nozzles, in this work this condition won't be taken into account. As previously stated, today

most modern gas turbine systems operate with lean premixed or partially premixed flames. The heat release rate of a premixed flame depends on:

- the density of the reactant flow;
- the burning rate or flame speed;
- the heat of reaction;
- the flame surface area.

Hence, fluctuations in these quantities will provoke unsteadiness in the heat release rate. Perturbations in temperature, stretch rate, and mixture composition of the reactant flow, affect in turn the fluctuations of the flame speed. The fluctuations in the flame surface area depend on the disturbances that alter the location and shape of the flame, which rely on the fluctuations either of the flame speed or of the inflow velocity. Finally, the fluctuations in the heat of the reaction are due to perturbations in the mixture composition. A detailed discussion of the heat release rate response to fluctuations in each of these physical quantities is given by Lieuwen [2].
Seven reasons determine the nonlinear dynamics of premixed flames. First, the propagation of the flame normal to itself, also known as *kinematic restoration*, depends nonlinearly on the amplitude and wavelength of a flame wrinkle. The amplitude and wavelength of flame wrinkles, in turn, depend on the amplitude and frequency of velocity disturbances that perturb the flame [2]. Second, the flame behavior relies not only on the instantaneous velocity field around the flame but also on the history of the velocity perturbations [18]. The reason is that wrinkles generated on the flame surface are advected at the velocity tangential to the flame surface and then spread along the flame until they are destroyed by flame propagation. As a third reason, fluctuations in the velocity field can cause an oscillating flame surface to pinch off, causing a sharp change in the flame surface area and, therefore, in the heat release rate [19]. Fourth, fluctuations in the velocity field cause local flow straining which leads to a flame stretch, which alters the flame speed, and as a consequence the heat release rate, in a nonlinear way [20]. Fifth reason, in attached flames the change in position of the flame attachment point depends nonlinearly on the amplitude of velocity perturbations. At low-amplitude velocity perturbations, the attachment point does not relocate itself, instead at high-amplitude velocity perturbations, the attachment point moves over a part of the cycle [21]. Furthermore, in this situation, flashbacks may occur thus introducing an additional nonlinearity [19]. For the next reason, flame geometry affects the degree to which local nonlinear effects influence the global nonlinearities in the heat release rate (integrated over the entire flame surface) [22].
In an axisymmetric flame, the degree to which local nonlinear effects affect the global nonlinearities depends on the flame shape, for example conical, wedge-shaped, etc. Seventh, fluctuations in the equivalence ratio cause fluctuations in the flame speed and heat of reaction, which are in turn nonlinear functions of the equivalence ratio [23].

3.5.2 Bifurcations

Dynamical systems theory has been often employed to study nonlinear flow and flame dynamics in combustion systems [24], [25]. The *trajectory* of a system represents the evolution in time of the system. Depending on the stability or instability of the system, a different type of trajectory is expected.
Let us consider a one-parameter autonomous (time-invariant) nonlinear dynamical system as follows

$$\frac{\mathrm{d}\mathbf{x}}{\mathrm{d}t} = \mathbf{f}[\mathbf{x}; P] \tag{3.37}$$

where $\mathbf{x}$ is the state vector variable and P is a scalar parameter. The equilibrium point $\mathbf{x_0}$ for the autonomous system of the previous equation, given some value of P, is the real root of the equation

$$\frac{\mathrm{d}\mathbf{x}}{\mathrm{d}t} = \mathbf{f}[\mathbf{x_0}; P] = 0 \tag{3.38}$$

The equilibrium solution $\mathbf{x_0}$ has the property that whenever the state of the system starts at $\mathbf{x_0}$, it will stay there for all future time. If the system is perturbed, in case of stable behaviour it will always return to its initial condition, while in case of instability the system solution will diverge. The stability of an equilibrium point is assessed by the eigenvalues of the Jacobian matrix $\mathbf{J} = \frac{\partial \mathbf{f}}{\partial \mathbf{x}}$ evaluated at the considered point. For the equilibrium solution to be stable, all the eigenvalues must have negative real parts. These type of dynamical systems may have not only equilibrium solutions but also periodic solutions: the limit cycles.
They are intrinsically nonlinear phenomena, as consequence they cannot occur in linear systems. The amplitude of a linear oscillation is set entirely by its initial conditions. On the other hand, limit cycle oscillations are prescribed by the structure of the system itself and, if the system is slightly perturbed, it will always return to the limit cycle. The qualitative behaviour of an autonomous dynamical system is thus determined by the pattern of its equilibrium points and periodic orbits, as well as by their stability properties, which further depend on the parameter P. Depending on the type of system and on the control parameter, three types of limit cycle can be expected, please see figure 3.6.

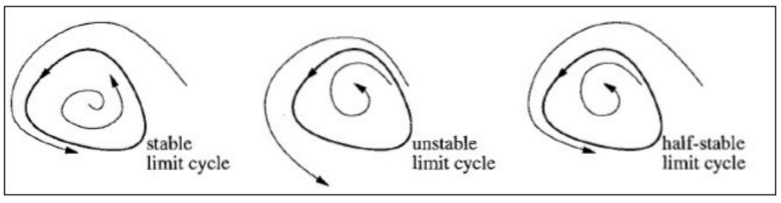

Figure 3.6: Different types of limit cycle [15].

As the reader can see in figure 3.6, for a *stable limit cycle* the perturbed system will return to the limit cycles's oscillations, while if we consider the *unstable limit cycle*, the system will depart from the limit cycle condition and eventually reach

an equilibrium point or maybe diverge. If there is a neighboring trajectory which spirals into the limit cycle as time approaches infinity, and another one which spirals into it as time approaches negative infinity, a *half-stable limit cycle* occurs. Nonlinear dynamic systems can have multiple solutions for a given system configuration. About this topic, we can define a *bifurcation plot*, which is a visual representation of all the solutions, and their stability, as a function of one or more parameters that change smoothly.
Bifurcations are divided into two major classes: **static bifurcations** and **dynamic Hopf bifurcations**. Static bifurcatons can then be subdivided into: *pitch fork bifurcations, transcritical bifurcation*s or *saddle note bifurcations*. However, these types of configurations are not the case for combustion instabilities, which are instead characterized by oscillations.
Dynamic Hopf bifurcations can be divided into: *supercritical* and *subcritical bifurcations*. As the reader can see in figure 3.7, in the two diagrams are presented two systems with the same control parameter P, with some measure of the steady-state amplitude of the system plotted on the vertical axis, a_s. Taking into consideration an oscillating system, a_s is frequently the peak-to-peak amplitude of the oscillations.

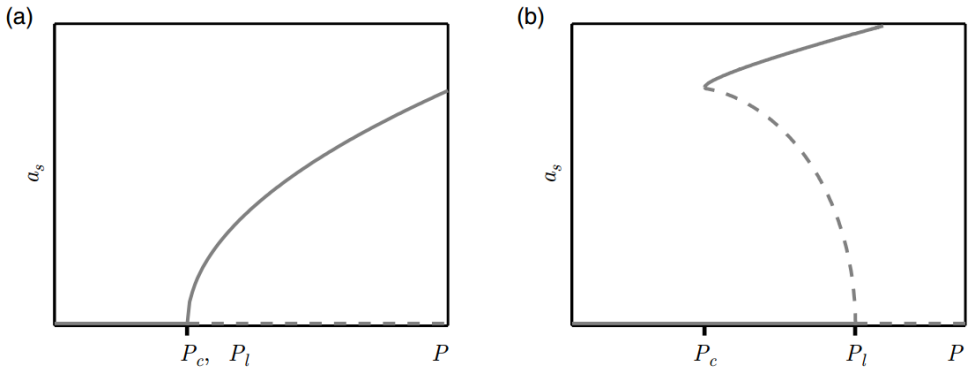

Figure 3.7: The steady state oscillation amplitude, a_s, as a function of a control parameter, P, for (a) a supercritical bifurcation and (b) a subcritical bifurcation [14].

We call *fixed point* the solutions characterized by a zero amplitude, which coincide with the horizontal axis in the following diagrams.
For low values of the control parameter the fixed point results to be stable in both cases. Once P is equal to P_l, at a location named *Hopf bifurcation point*, the fixed point becomes unstable. The system starts oscillating and ultimately ends up at the solid line, which represents the steady-state amplitude. As already anticipated, this state corresponds to a periodic solution named *limit cycle*. It is important to bear in mind that besides the stable periodic solution, there are other types of solutions, such as *multi-periodic, quasi-periodic* or *chaotic attractors*, even in this case the system can trigger sustained oscillations, but these are not characterized by a simple period [26].
The nonlinear response around the Hopf bifurcation point at P_l defines which type of bifurcation it is. The first pattern is a supercritical bifurcation (figure 3.7a) and is characterized by an amplitude that grows gradually with P for $P > P_l$. The second pattern is a subcritical bifurcation (figure 3.7b) and is characterized by an amplitude

that grows suddenly as P increases through P_l. This second type has two stable solutions for $P_c \leq P \leq P_l$, defining a *bistable region*. In this range, every little perturbation will die down, on the contrary, if they are large enough to cross the dashed line, which delineates an unstable periodic solution, then the perturbations will grow to the limit cycle [26].
Regarding subcritical bifurcations, the reason why the system can have a periodic stable solution for values of $P < P_l$ is due to hysteresis, whose presence, in consequence, is the signature of triggering instability. Undoubtedly, for $P > P_l$, concerning each type of bifurcation, even the slight perturbation can become unstable.

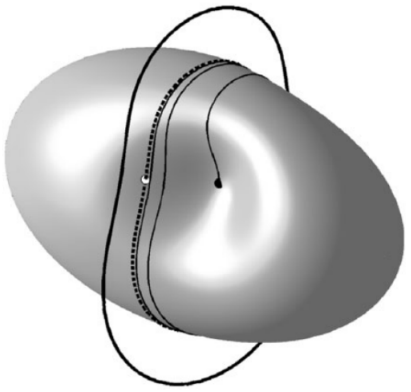

Figure 3.8: A cartoon of the manifold that separates the states that evolve to the stable fixed point from those that evolve to the stable periodic solution [14].

Another important aspect to keep in mind is that most of the time these types of analysis involve systems with many degrees of freedom. So, the bifurcation plot will be obtained from a section of a multi-space representation. As an example, in figure 3.8 we can find a representation for a three-dimensional space of the bistable region, typical of subcritical bifurcations. The potato-shaped surface corresponds to the manifold that separates the states that evolve to the stable fixed point from those evolving to the stable periodic solution, illustrated as the large loop allocated outside the surface [14]. The nonuniformity of this surface is related to the non-normality of the examined system. Moreover, the point that lays precisely on the manifold will stay on it permanently. For a state to end up to the limit cycle, it has to start outside the manifold. The unstable periodic solution is again depicted by a dashed line, if there would be an infinitesimal addition of energy to any state in balance on this loop, it would soon evolve to the stable periodic solution.

4 Linear analysis of the case study

4.1 General description

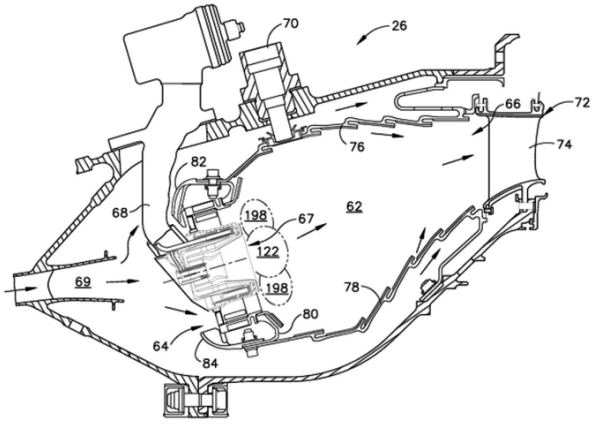

Figure 4.1: Jet engine combustor geometry. Mixer assembly for gas turbine engine combustor. Source: From US Patent US8171735B2, Mancini and Mongia , GE [27].

The starting point of this work is to investigate the thermoacoustic instabilities of a toy model LPP combustor. As the reader can see in figure 4.1, representing a combustor with a main LPP burner for an aero engine application, at the inlet of the combustor the high-speed flow coming from the preceding compressor is decelerated in a diffuser and made at the same time more uniform for the next component, the premixer. At this stage, the fuel is injected and mixed with air, to react and burn in the subsequent section, the combustion chamber.

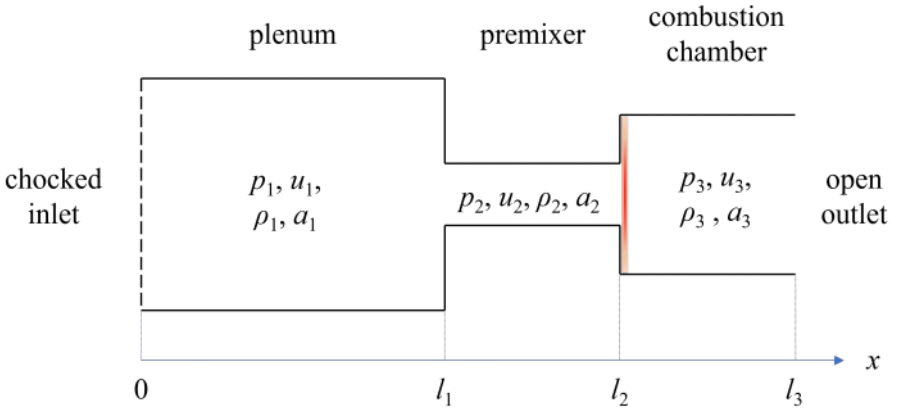

Figure 4.2: Sketch of the three-ducts combustion model.

4.2 The TALOM approach

To carry out a mathematical analysis on a more treatable problem, a simple three-ducts combustion model is investigated, consisting of a plenum, followed by a premixer, and finally by a combustor chamber, using the premixed combustor prototype described by Dowling and Stow [1], figure 4.2.
The flow evolving in this control volume is considered to be one-dimensional. The inlet is choked, so regardless to downstream perturbations of pressure, the energy and mass flow rates are practically constant. The outlet is defined as a pressure outlet.
In the following table the details of the geometry are presented.

Description	Symbol	Value
Plenum cross-sectional area	a_1	0.0129 m^2
Plenum length	l_1	1.7 m
Premixer cross-sectional area	a_2	0.00142 m^2
Premixer lentgth	l_2	0.0345 m
Combustor cross-sectional area	a_3	0.00385 m^2
Combustor lentgth	l_3	1.0 m

Table 4.1: Geometry of the simple combustor.

The mean flow parameters are considered to be uniform in each of the three ducts that form the system. The flow is treated as inviscid.
As the reader can notice, the flame is considered a compact flame sheet located at the intersection between the premixer and the combustion chamber, that means it is axially short compared to the wavelengths of the perturbations.
In addition, it reaches a temperature of 2000 K, which is uniformly distributed in all section three. The chemical reactions are consequently instantaneous, so in the governing equations, the flame model is not added as a source term, but only introduced in the jump condition between the last two ducts.
The system is solved as an eigenvalue problem in the complex domain using an approach denominated **TALOM** (Thermo-Acoustic Low-Order Modelling). This approach has been developed because on the reference paper from Dowling and Stow, it is not specified what type of method is used to compute the eigenmodes. This is a lumped approach which expresses the system through a set of suitable equations deduced from boundary and jump conditions, it computes the eigenvalues in an iterative way, with a proper tolerance, in a neighborhood of a starting solution, found with a graphical method based on the determinant of the coefficient matrix.

4.2.1 Base flow equations

We first put our attention to the base flow. As already done before, the flow variables are decomposed as the sum of a base term (time mean) plus a small fluctuating term, e.g.

$$p = p(x,t) = \bar{p} + p'(x,t); \quad u = u(x,t) = \bar{u} + u'(x,t); \quad ecc. \tag{4.1}$$

the unknowns are $\bar{u}_i, \bar{p}_i, \bar{\rho}_i, \bar{T}_i$, where $i = 1, 2, 3$ represents each section, the last unknown is the mean rate of heat input per unit area $\bar{q}$, introduced in the jump condition between the premixer and the combustion chamber. The total number of unknowns is therefore 13. So, the base flow equations for mass, momentum and energy conservation, without heat input are

$$\bar{\rho}\frac{\mathrm{d}\bar{u}}{\mathrm{d}x} + \bar{u}\frac{\mathrm{d}\bar{\rho}}{\mathrm{d}x} = 0 \tag{4.2}$$

$$\bar{\rho}\bar{u}\frac{\mathrm{d}\bar{u}}{\mathrm{d}x} + \frac{\mathrm{d}\bar{p}}{\mathrm{d}x} = 0 \tag{4.3}$$

$$\bar{u}\frac{\mathrm{d}\bar{p}}{\mathrm{d}x} + \gamma\bar{p}\frac{\mathrm{d}\bar{u}}{\mathrm{d}x} = 0 \tag{4.4}$$

This set of equations is written for every duct. Next, the perfect gas equation is written for each duct

$$\bar{p}_i = \bar{\rho}_i R_{gas} \bar{T}_i \tag{4.5}$$

where $R_{gas} = c_p$ - c_v is the perfect gas constant.
For the intersection at $x = l_1$ (plenum-premixer), three jump conditions are introduced, one equation for mass conservation, one for energy conservation and one isentropic condition attributable to the cross sectional area decreases

$$\bar{\rho}_1 a_1 \bar{u}_1 = \bar{\rho}_2 a_2 \bar{u}_2 \tag{4.6}$$

$$\bar{\rho}_1 a_1 \bar{u}_1 \bar{H}_1 = \bar{\rho}_2 a_2 \bar{u}_2 \bar{H}_2 \tag{4.7}$$

$$\frac{\bar{p}_1}{\bar{p}_2} = \left(\frac{\bar{\rho}_1}{\bar{\rho}_2}\right)^{\gamma} \tag{4.8}$$

where $\bar{H} = c_p\bar{T} + \frac{1}{2}u^2$ is the total enthalpy.
For the intersection at $x = l_2$ (premixer-combustion chamber), three jump conditions are introduced, one equation for mass conservation, one for energy conservation, and one Borda equation attributable to the cross sectional area increase

$$\bar{\rho}_2 a_2 \bar{u}_2 = \bar{\rho}_3 a_3 \bar{u}_3 \tag{4.9}$$

$$\bar{\rho}_1 a_2 \bar{u}_2 \bar{H}_2 = \bar{\rho}_3 a_3 \bar{u}_3 \bar{H}_3 + a_3 \bar{q} \tag{4.10}$$

$$\bar{\rho}_3 a_3 \bar{u}_3^2 - \bar{\rho}_2 a_2 \bar{u}_2^2 = a_3(\bar{p}_3 - \bar{p}_2) \tag{4.11}$$

Finally, from the boundary conditions we can get some values for the starting conditions:

$$\bar{\dot{m}}_1 = 0.05\ kg/s; \quad \bar{T}_1 = 300\ K; \quad \bar{p}_3 = 101000\ Pa; \quad \bar{T}_3 = T_{flame} = 2000\ K \tag{4.12}$$

This previous set of 13 equations gives the following results for the base variables:

Section	$\bar{u}$ $[m/s]$	$\bar{p}$ $[Pa]$	$\bar{\rho}$ $[\frac{kg}{m^3}]$	$\bar{T}$ $[K]$
Plenum	3.269	103121	1.186	300
Premixer	29.809	102616	1.181	299.563
Combustion Chamber	73.818	101000	0.1759	2000

Table 4.2: Results for the mean flow.

Together with $\bar{q} = 22216000$ $[W/m^2]$, and after multiplying by the flame area, we obtain the heat transfer rate provided by the flame, $\dot{\bar{Q}}_f = \bar{q} \cdot a_3 = 22216000$ $[W/m^2] \cdot 0.00385[m^2] = 85531.6$ $[W]$

4.2.2 Perturbation equations

Once the mean flow is solved, we can start with the following conservation equations, for an inviscid compressible flow, for mass, momentum, energy, respectively.

$$\frac{\partial \rho'}{\partial t} + \bar{u}\frac{\partial \rho'}{\partial x} + \bar{\rho}\frac{\partial u'}{\partial x} = 0 \tag{4.13}$$

$$\bar{\rho}\frac{\partial u'}{\partial t} + \bar{u}\bar{\rho}\frac{\partial u'}{\partial x} + \frac{\partial p'}{\partial x} = 0 \tag{4.14}$$

$$\frac{\partial p'}{\partial t} + \bar{u}\frac{\partial p'}{\partial x} + \bar{p}\gamma\frac{\partial u'}{\partial x} = 0 \tag{4.15}$$

The perturbed flow is solved in a similar manner as the base flow after having converted the variables in the frequency domain.

$$p'(x,t) = \hat{p}(x)e^{i\omega t}; \quad u'(x,t) = \hat{u}(x)e^{i\omega t}; \quad \rho'(x,t) = \hat{\rho}(x)e^{i\omega t} \quad q'(x,t) = \hat{q}(x)e^{i\omega t} \tag{4.16}$$

where $\omega = \omega_{real} + i\omega_{imaginary}$ is the complex frequency, whose real part (ω_{real}) corresponds to the frequency of the oscillation and the negative imaginary part ($-\omega_{imaginary}$) represents the growth rate.
We now remember that any disturbance can be decomposed as the combination of an acoustic, entropy, and vorticity disturbance, independent from one another respectively. This possibility is admitted by the presence of a mean flow, that can convect entropy and vorticity disturbances. Moreover, another effect of the mean flow is that it admits modes with much lower frequencies, of the order of 40-150 Hz. We know from section 2.2, that unsteady combustion is able to generate entropy waves or local hot spots, at low-frequency oscillations, the entropy wavelengths result to be long, and these waves undergo little attenuation, thus generating sound. At higher frequencies instead, entropy waves will diffuse, so the amplitude of high-frequency entropic disturbances may be judged inconsiderable when the wave arrives at the exit of the combustor.
In this one-dimensional case the vorticity disturbances will not be considered. That being so, the complex amplitudes are decoupled as

$$\hat{p}(x) = A_+ \, e^{\,k_+ x} + A_- \, e^{\,k_- x} \tag{4.17}$$

$$\hat{\rho}(x) = \frac{1}{\bar{c}^2}\left(A_+ \, e^{\,k_+ x} + A_- \, e^{\,k_- x}\right) - \frac{1}{\bar{c}^2} A_e \, e^{\,k_0 x} \tag{4.18}$$

$$\hat{u}(x) = -\left(\frac{k_+}{\bar{\rho}\alpha_+} A_+ \, e^{\,k_+ x} + \frac{k_-}{\bar{\rho}\alpha_-} A_- \, e^{\,k_- x}\right) \tag{4.19}$$

where A_+ and A_- are the amplitudes of forward- and backward-travelling acoustic waves, respectively, A_e is the amplitude of the entropy wave and the speed of sound is $\bar{c} = \sqrt{\left(\frac{\partial p}{\partial \rho}\right)_s}$. The dispersion relations are

$$k_\pm = \frac{\bar{M}\omega \mp |\omega|}{\bar{c}(1-\bar{M}^2)}; \quad k_0 = -\frac{\omega}{\bar{u}}; \quad \alpha_\pm = \omega + \bar{u} k_\pm \tag{4.20}$$

with the Mach number defined as $\bar{M} = \frac{\bar{u}}{\bar{c}}$. Following that, the jump conditions for each duct section are proposed, linearized to the first-order.
For the first intersection ($x = l_1$), we have

$$a_1(\bar{\rho}_1 \hat{u}_1 + \bar{u}_1 \hat{\rho}_1) = a_2(\bar{\rho}_2 \hat{u}_2 + \bar{u}_2 \hat{\rho}_2) \tag{4.21}$$

$$\gamma \frac{\hat{\rho}_1}{\bar{\rho}_1} - \frac{\hat{p}_1}{\bar{p}_1} = \gamma \frac{\hat{\rho}_2}{\bar{\rho}_2} - \frac{\hat{p}_2}{\bar{p}_2} \tag{4.22}$$

$$cp\hat{T}_1 + \hat{u}_1 \bar{u}_1 = cp\hat{T}_2 + \hat{u}_2 \bar{u}_2 \tag{4.23}$$

The next intersection is at $x = l_2$:

$$a_2(\bar{\rho}_2 \hat{u}_2 + \bar{u}_2 \hat{\rho}_2) = a_3(\bar{\rho}_3 \hat{u}_3 + \bar{u}_3 \hat{\rho}_3) \tag{4.24}$$

$$a_2 \hat{\rho}_2 \bar{u}_2^2 + 2a_2 \bar{\rho}_2 \bar{u}_2 \hat{u}_2 = a_3 \hat{\rho}_3 \bar{u}_3^2 + 2a_3 \bar{\rho}_3 \bar{u}_3 \hat{u}_3 + a_3(\hat{p}_3 - \hat{p}_2) \tag{4.25}$$

$$a_2(\bar{u}_2 \bar{\rho}_2 \hat{H}_2 + \bar{H}_2 \bar{u}_2 \hat{\rho}_2 + \bar{\rho}_2 \bar{H}_2 \hat{u}_2) = a_3(\bar{u}_3 \bar{\rho}_3 \hat{H}_3 + \bar{H}_3 \bar{u}_3 \hat{\rho}_3 + \bar{\rho}_3 \bar{H}_3 \hat{u}_3 - \hat{q}) \tag{4.26}$$

with the complex amplitude of the unsteady heat release rate per unit area $\hat{q}$, expressed with the following FTF:

$$\hat{q} = -k\bar{q} \frac{\hat{\dot{m}}_2}{\bar{\dot{m}}_2} e^{-i\omega\tau} \tag{4.27}$$

where, the mass flow rate in the premixer is intended as $\dot{m}_2 = \bar{\dot{m}}_2 + \hat{\dot{m}}_2 e^{i\omega t}$, k is a term that let us switch on or off the unsteady heat release rate term. τ is a *time lag*, which will be set equal to 0.006 seconds and represents the fuel convection time, from its injection to combustion. The mass flow rate fluctuation $\dot{m}_2 = \hat{\dot{m}}_2 e^{i\omega t}$, is sampled right before the flame.
Finally, the boundary conditions for the choked inlet ($x = 0$), that comes from a constant nondimensional mass flow, and the pressure outlet ($x = l_3$) respectively are:

$$\frac{\hat{\rho}_1(0)}{\bar{\rho}_1(0)} + \frac{\hat{u}_1(0)}{\bar{u}_1(0)} = 0; \quad \hat{p}_3(l_3) = 0 \tag{4.28}$$

The correct frequencies will be the ones that satisfy the boundary conditions.
In order to close the problem, one more equation is needed, we will use the isentropic condition at $x = 0$:

$$\hat{p}_1(0) = \bar{c}_1^2 \hat{\rho}_1(0) \tag{4.29}$$

The perturbed flow is ready to be solved. The previous set of equations can be rewritten in a matrix form of the type $M\mathbf{q} = \mathbf{0}$. Where $\mathbf{q}$ is a vector containing the decoupled acoustic and entropy amplitudes: A_+, A_-, A_e; M is the coefficient matrix. This eigenvalue problem is solved by the *inverse iteration algorithm* [28]. The starting condition for the iteration algorithm is obtained from a graphical approach. It essentially consists of finding the determinant of the previous matrix M. We have a solution when the determinant is equal to zero, because the determinant is a complex number, both its real and imaginary parts need to be null at the same time. This is why we look for the intersection of the zero contours of $Re(detM)$ and $Im(detM)$. As a consequence, we draw the contour lines for the real and imaginary part of the computed determinant in a two-dimensional space that has frequency (Hz) on the x-axis, and the growth rate (s^{-1}) on the y-axis, please see figure 4.3.
The input values for the succeeding algorithm are extracted from the intersection of the two types of contour lines.
Next, once completed the iterations and found the wave amplitudes, they can be substituted in the previous formulations for the acoustic and entropy waves, in order to find the mode shapes, see equations 4.17, 4.18, and 4.19.

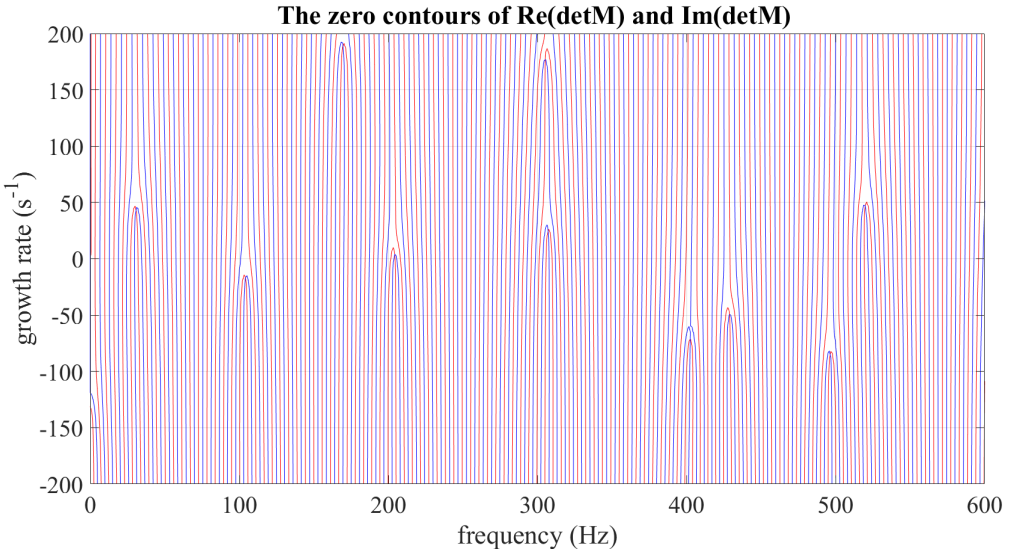

Figure 4.3: Grafical method for the case with fluctuating heat release rate (k=1).

In figure 4.4, is presented the spectrum for the case of constant heat release rate, that means the fluctuating term is set equal to zero. The results obtained from the previous system and resolved with the proposed algorithm are then compared with the ones calculated by Dowling and Stow, used as reference [1].
In this first case, all the growth rates are negative, as one would expect, because there is no fluctuating heat release rate, as a consequence, the system will be asymptotically

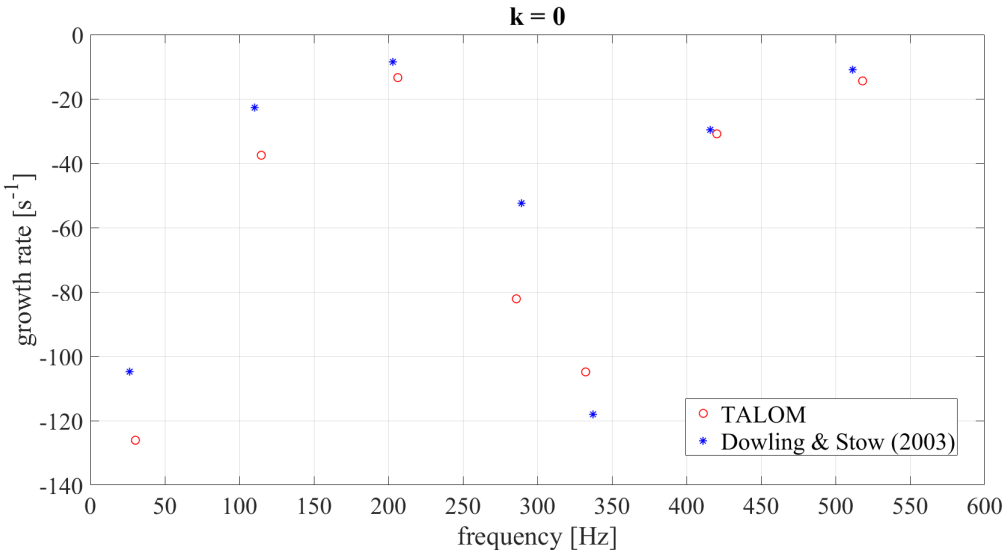

Figure 4.4: Spectrum for the case of zero fluctuating heat release rate (k=0).

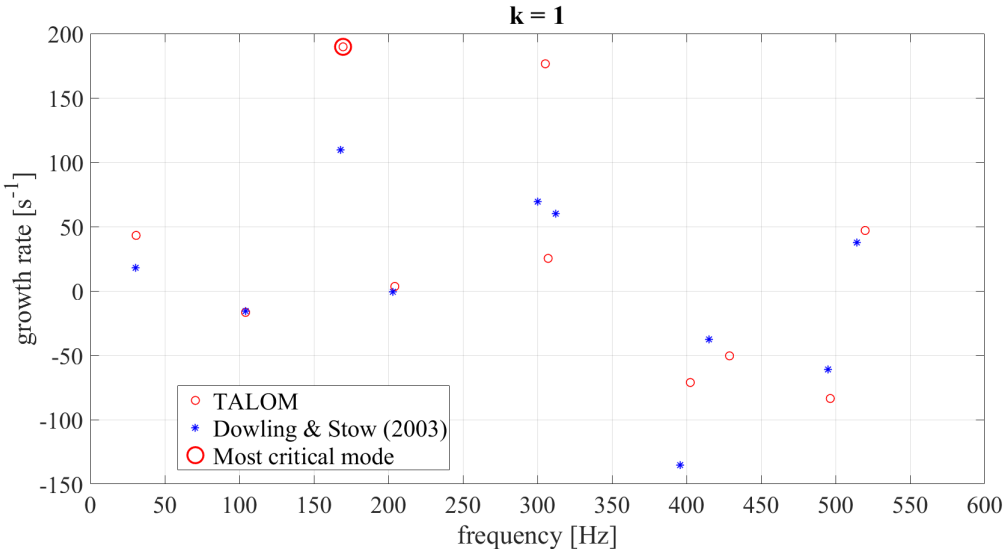

Figure 4.5: Spectrum for the case with fluctuating heat release rate (k=1).

stable. Although some values of the growth rates are not perfectly coincident with the reference results, the frequencies are almost equivalent.
The next case, please see figure 4.5, takes into account the unstable heat release rate presented in the previous section (equation 4.27). Also in this condition, the TALOM spectrum captures well the frequencies of the dominant modes provided by Dowling and Stow. In addition, the reader can now notice that some modes are characterized by a positive growth rate, especially between 0 and 500 Hz. That means, according to the linear stability theory, that the solution will be unstable, with a consequent exponential growth. We can also notice that the TALOM approach doesn't return the same growth rates as the ones computed by Dowling and Stow, this may highlight a strong sensibility of the system to the mean flow.
The asymptotic behavior of the system is dominated by the least stable eigenmode,

the one that has the largest growth rate, which here appears at a frequency of 169.5 *Hz* with a growth rate around 189 s^{-1}.

4.2.3 Variation of the time lag τ

In the previous subsection, we have investigated the thermoacoustic behavior of the system for a given time lag τ (the fuel convection time from its injection to c), set equal tombustiono 6 milliseconds. We now investigate the stability of the system for different values of the time lag, please see figure 4.6. The parameter τ has been varied from 0.1 to 10 milliseconds. For every new time lag, we have individuated a starting condition with the graphical method and then obtained the exact eigenvalues with the inverse iteration algorithm.

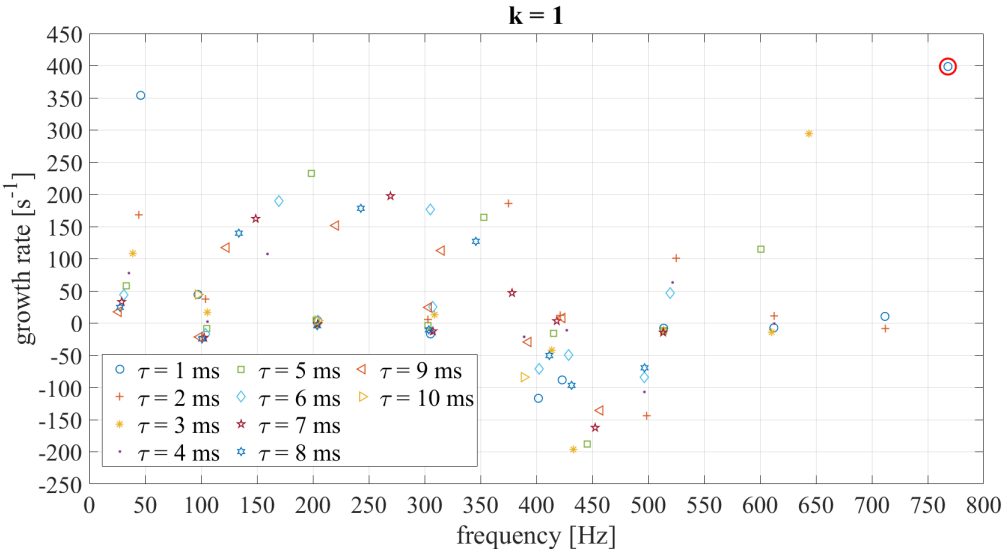

Figure 4.6: Eigenmodes for different time lags, $\tau = 0.1 - 10$ ms.

From these results, one can see that, by altering the time lag, particularly by reducing τ, higher frequencies and growth rates are obtained. This aspect highlights the strong variability of the resulting modes, which are greatly dependent on the time lag τ. The most critical mode, circled in red, is found for a time lag of 1 millisecond at a frequency around 775 Hz.

4.2.4 Implementation of a different flame model

To make a comparison with the results from future simulations, a new flame transfer function has been implemented on the MATLAB code for calculating the linear stability of the simple combustor. The new flame model has been extracted from the reference paper of Dowiling and Stow and resembles the Crocco's model, please see section 2.5.
The new formula for the unsteady heat input is related to the oncoming air velocity fluctuation with a time delay τ:

$$q'(t) = -\beta \frac{\bar{\rho}_2 \bar{c}_2^2}{(\gamma - 1)} u'_{bf}(t - \tau) \tag{4.30}$$

The subscript 2 indicates the mean values of section 2, the premixer, an *bf* stands for *before flame*. β is a nondimensional parameter and is expected to lie in the range from 0 to 10 [1].

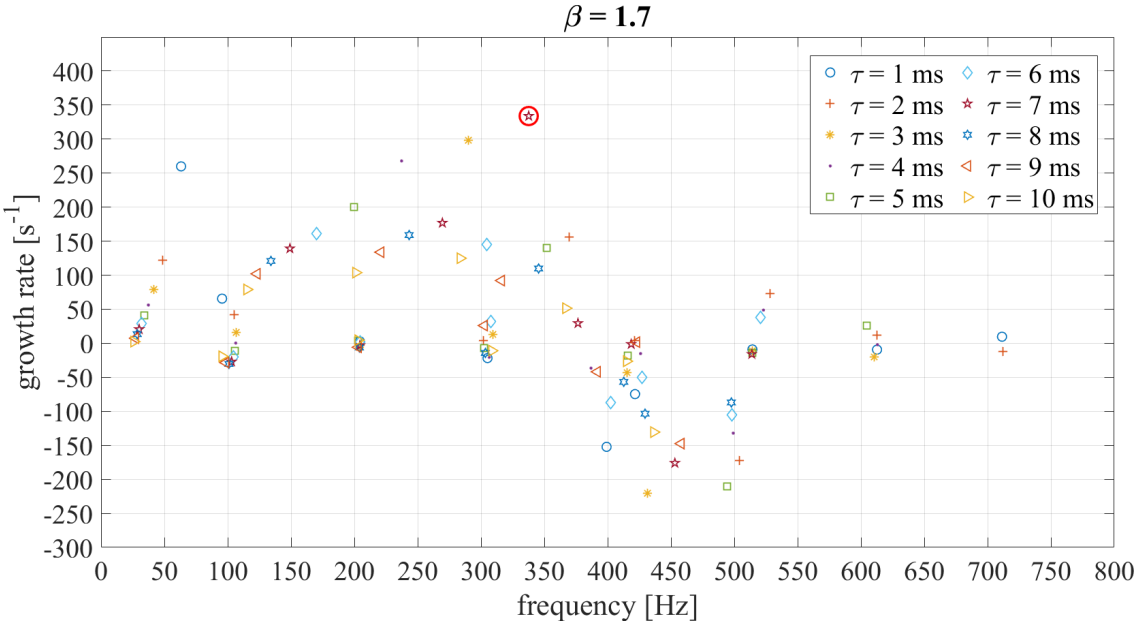

Figure 4.7: Eigenmodes for different time lags, $\tau = 0.1 - 10$ ms, $\beta = 1.7$.

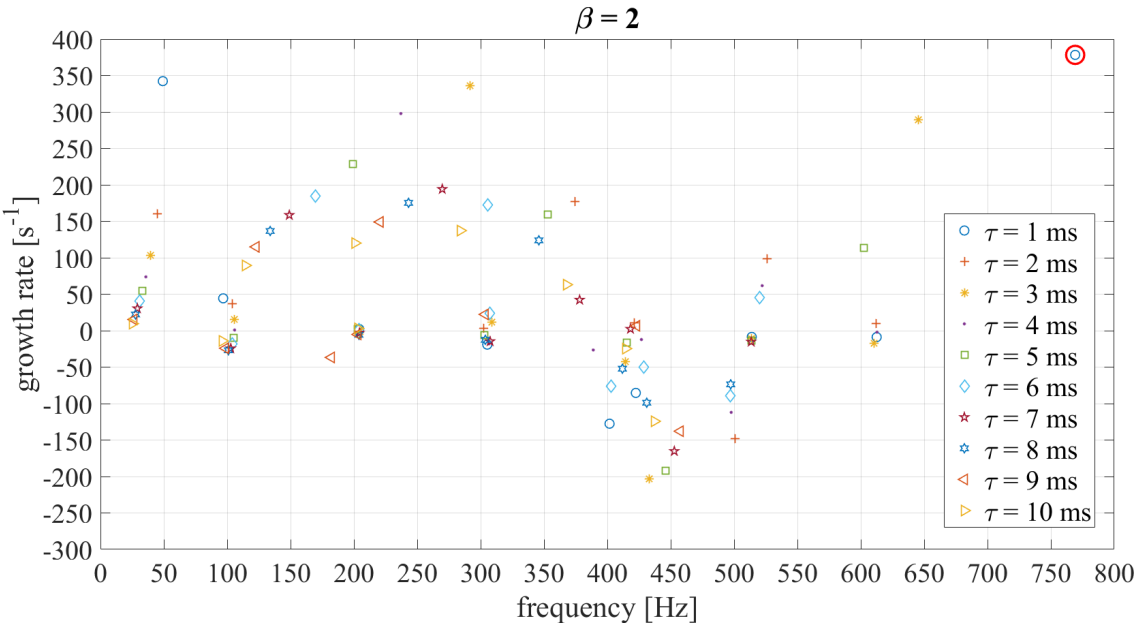

Figure 4.8: Eigenmodes for different time lags, $\tau = 0.1 - 10$ ms, $\beta = 2$.

In the succeeding figures 4.7, 4.8, are presented the eigenmodes for β set equal to 1.7 and 2, with a time lag τ varying from 0.1 to 10 milliseconds.
Similar conclusions to the previous case (paragraph 4.2.3), with a dependency of the unsteady heat transfer rate on the mass flow rate fluctuations, can be drawn here.

Again, one can see that reducing the time lag brings to new eigenmodes, located at higher frequencies. Additionally, the general trajectories of the eigenmodes in both cases for β=1.7 and 2, result to be similar to the ones obtained with Crocco's flame model.
In addition, increasing the value of the constant β grants higher growth rates. The most critical mode is circled again in red. For β=1.7, it is characterized by a frequency close to 350 Hz, for β=2, it is triggered at a frequency around 775 Hz, as found before with a different FTF, but with a bigger growth rate.
What we can conclude is that, the flame transfer functions are strongly dependent on parameters such as τ or β, and different choices of these two could give distinctive results, with distant eigenfrequencies. So, without knowing in advance what specific flame transfer function to use, there is good probability to obtain ambiguous results.

5 Nonlinear analysis of the case study

The successive part of this work is based on the numerical tests conducted with *Ansys*, a commercial software for computational fluid dynamics (CFD). The following numerical analysis aims to investigate the nonlinear behavior of the model combustor introduced in section 4. The workflow starts from the definition of the control volume geometry, subsequently, a proper mesh is defined, based on the type of simulation that is going to be performed, and lastly, the results are post-processed.

5.1 Geometry

The first step to follow to accomplish a CFD simulation is to generate a proper geometry. The program used is *SpaceClaim*. The numerical tests that have been conducted are for a two-dimensional flow. Moreover, having in mind to compute an axisymmetric simulation, which means that there will be no gradient along the circumferential direction, just half of the combustor has been designed. This has also the advantage to reduce the computational cost because the following mesh will be generated for half of the two-dimensional control volume. From the reference paper of Dowling and Stow, when it comes to the geometry of the model combustor the cross-sectional areas of the three ducts are given. As the reader can observe in the following figure 5.1, with the intention to draw a two-dimensional geometry, these cross-sections are intended to be circular, from which the radii of the three ducts have been extracted.

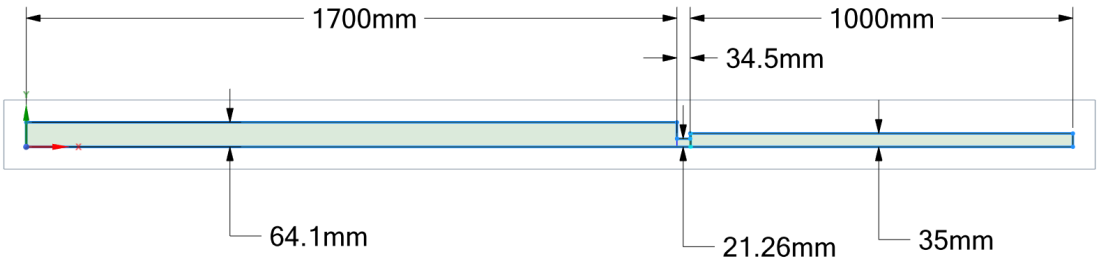

Figure 5.1: Geometry of the model combustor designed on SpaceClaim.

The next issue has been an adequate definition of the flame sheet. In this case, the flame cannot be of infinitesimal thickness as supposed by Dowling and Stow. Given the dimensions of the control volume, its thickness has been set equal to 2.5 millimeters, so that it can be estimated as adequately thin. In figure 5.2, highlighted in red, the flame geometry is presented. One could notice that, differently from Dowling and Stow, in this case, the flame has been limited in radial extension up to the second duct and not to the third one. Because, from the first simulations, it has been noticed that the flow recirculation established after the cross-section increase would have caused an overheating close to the walls.

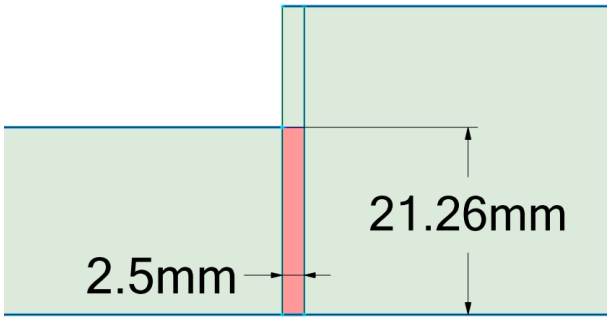

Figure 5.2: The modeled flame geometry.

5.2 Mesh

The second step is the mesh. For this particular case, an unstructured mesh with triangular elements has been designed, having in mind to conduct an URANS simulation, which models all the turbulent scales without solving them directly as with a DNS, or partially as with a LES. The number of cells is 135467, and the minimum orthogonal quality is $1.79838e-01$. In the following figure 5.3, a zoom on section two is represented, in addition, the flame region is highlighted in red. An inflation layer has been added at the walls aiming at properly computing the boundary layer with a value of the $y+$ around 1.

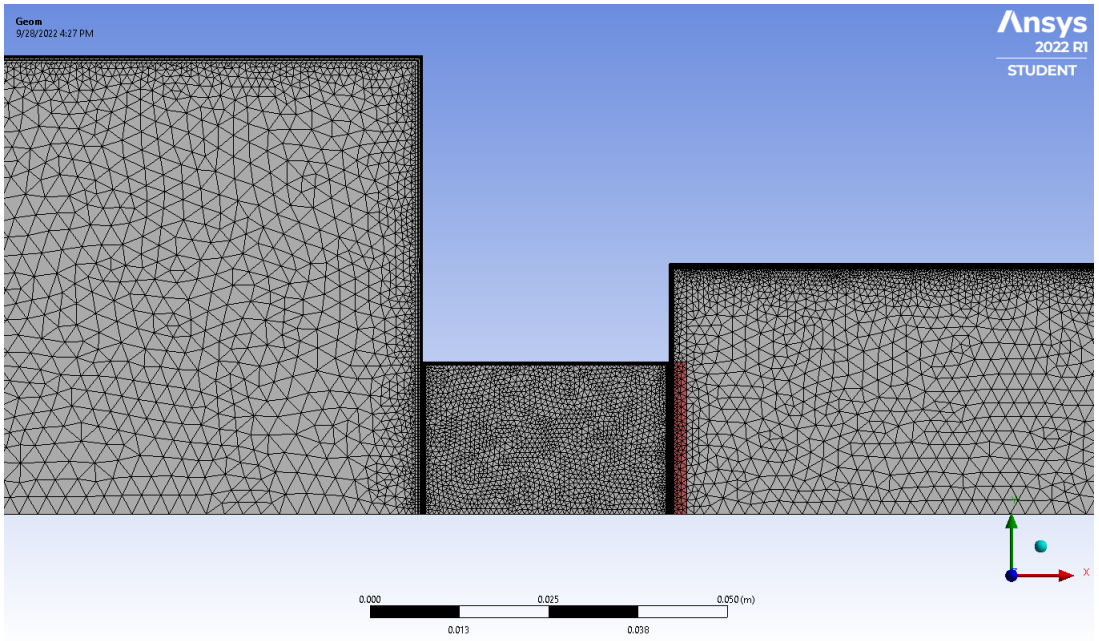

Figure 5.3: The mesh (zoom).

5.3 Setup of the simulation

The next software that has been adopted is *Ansys Fluent*. The solver type is pressure-based, the velocity formulation absolute and the two-dimensional space axisymmteric. The adopted turbulence model is the Shear-Stress Transport (SST) $k-\omega$ tur-

bulence model, with the energy equation that has been activated. In addition, no combustion model has been employed. In order to mimic a combustion reaction we act on the flame zone, for example controlling its temperature. For the solution method, the coupled scheme has been implemented, together with a second order upwind spatial discretization.
The setup of the simulations aims at reproducing the same conditions of the model combustor of Dowling and Stow (section 4).
The fluid simulated is air, the specified properties are the following:

- Density: calculated thanks to the ideal gas law.
- c_p: constant and equal to 1010 $\frac{J}{kgK}$.
- Thermal conductivity: constant and equal to 0.0242 $\frac{W}{mK}$.
- Viscosity: calculated thanks to the Sutherland's law.
- Molecular weight: constant and equal to 28.966 $\frac{kg}{kmol}$

The boundary condition for the inlet is specified as a mass flow rate inlet of 0.05 $\frac{kg}{s}$, the inlet temperature is set equal to 300 K. For the outlet, a pressure outlet has been set, with a pressure of 101000 Pa and a backflow total temperature of 2000 K. The walls are set to be adiabatic.

5.4 Control of the flame temperature

In order to reproduce the base flow conditions of the model combustor of Dowling and Stow, and properly calibrate the model, as first attempt the temperature of the flame has been fixed and controlled in time thanks to a specific expression introduced for the flame zone, please see figure 5.4 as an example.

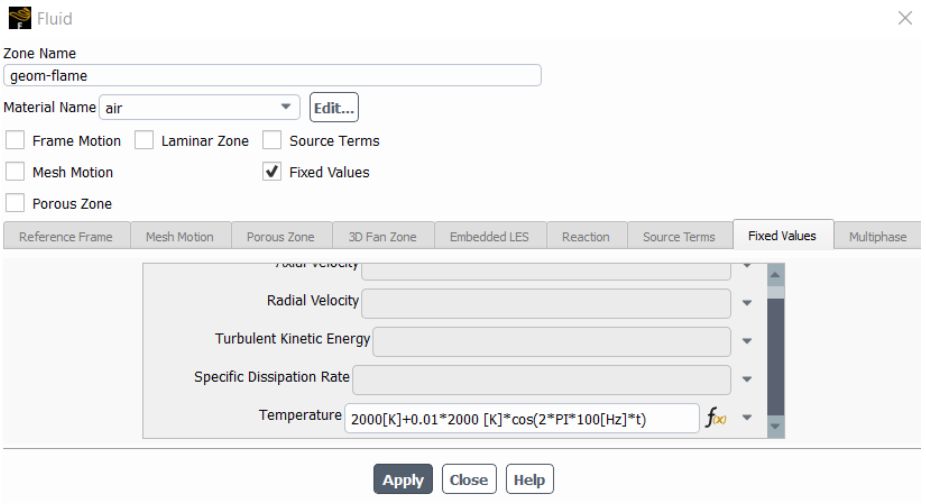

Figure 5.4: Example for the flame zone temperature expression.

5.4.1 The steady natural case

The first case that has been tested is the *natural case*, where the temperature of the flame is constant with time and set equal to 2000 K. Initially, steady simulations have been conducted, with the principal aim of reaching an almost uniform temperature in the combustion chamber. Moreover, an examination has been done also for the mean flow variables calculated in section 4, with reference to the table 5.2. In order to do this, four lines have been defined at 1.5, 1.72, 2, and 2.5 meters to perform an area weighted average of the resulting temperature, density, pressure and axial velocity profiles (figure 5.5).

Figure 5.5: Reference lines at 1.5, 1.72, 2, *and* 2.5 *meters from the inlet.*

After about 500 iterations, convergence of the RANS simulation is reached. The results for the area averages in the different ducts are:

Area weighted average	Axial velocity [m/s]	p [Pa]	ρ [$\frac{kg}{m^3}$]	T [K]
1.5 m	3.137	106163	1.232	299.995
1.72 m	28.760	104889	1.220	299.286
2 m	74.430	100997	0.1746	2015.532
2.5 m	74.402	101046	0.1746	2016.817

Table 5.1: Results from the steady simulation for $T_{flame} = 2000\ K$.

The **net total heat transfer rate** provided by the model combustor is **-85905 W**, this value is negative because the heat flux is globally outgoing from the control volume. For the purpose of clarity, we report the table of results for the base flow of the model combustor of Dowling and Stow. The reader can see that there is a notable

Section	$\bar{u}$ [m/s]	$\bar{p}$ [Pa]	$\bar{\rho}$ [$\frac{kg}{m^3}$]	$\bar{T}$ [K]
Plenum	3.269	103121	1.186	300
Premixer	29.809	102616	1.181	299.563
Combustion Chamber	73.818	101000	0.1759	2000

Table 5.2: Results for the mean flow.

agreement between the results. In the third duct, two lines have been defined in order to evaluate the effect on the flow variables of the hot jet flow coming from duct two. As expected, due to thermal diffusion at the end of the combustor the outgoing flow has a temperature around 2000 K. Finally, it is advised to point out that the comparison has been done with the mean flow variables, because the Reynolds-Averaged Navier-Stokes (RANS) simulations are based on averaged flow variables [D. C. Wilcox. Turbulence Modeling for CFD. DCW Industries, 2006].

5.4.2 The unsteady natural case

Once the steady natural case has been analyzed and the temperature of the flame zone defined, the following step is an unsteady simulation of the same case. Which will be the starting condition for the future numerical tests, once a statistically steady condition has been achieved. For the pressure-velocity coupling, in order to promote the stability of the solution, the factional step scheme has been implemented together with a second order spatial discretization. Finally, a bounded second order implicit transient formulation has been chosen, along with the non-iterative time advancement (NITA), this approach results to be faster than the "segregated methods", but needs much more memory. It is important to point out that a CFL number with a value less than one is necessary to grant convergence, as a consequence a time step of $6.7e-6$ seconds has been set.
In order to check the simulation in time, we have set monitors for the net mass flow rate between the boundaries, likewise for the net total heat transfer flux (which is defined as the flux of total enthalpy). Among various monitors, we have some for static pressure, calculated in five specific points located in the combustion chamber duct, please see figure 5.6. Their coordinates are, where we remember the origin of the reference system to be at the inlet on the axis,

Point	x [m]	y [m]
1	1.82	0.009
2	1.92	0.009
3	1.82	0.025
4	1.92	0.025
5	2.7	0.025

Table 5.3: Pressure points coordinates.

Figure 5.6: Pressure points (in white).

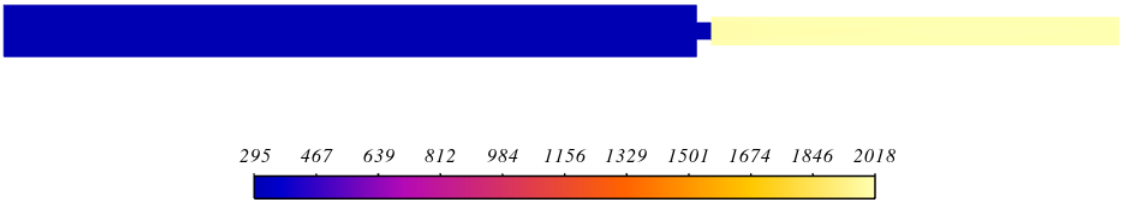

Figure 5.7: URANS simulation, general temperature distribution [K].

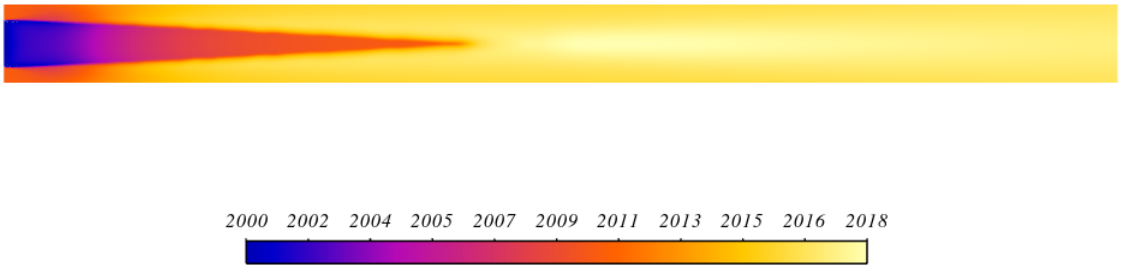

Figure 5.8: URANS simulation, temperature distribution in the combustion chamber duct [K].

In figure 5.8, the reader can appreciate the temperature distribution for the jet flow entering the combustion chamber section after the premixer duct, heating up through the flame sheet, and leaving the combustor with a temperature profile close to 2000 K.

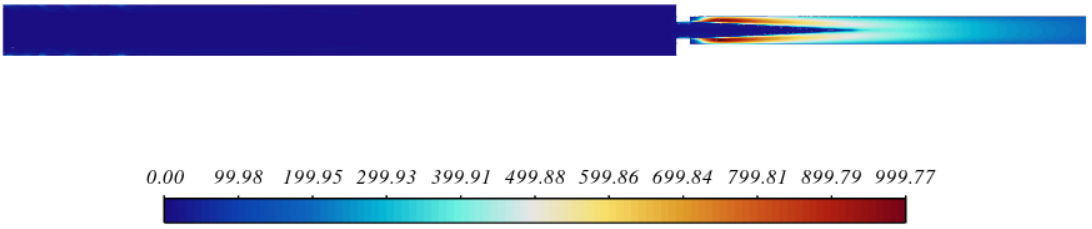

Figure 5.9: URANS simulation, turbulent intensity distribution [%].

From figure 5.9, we can see that the maximum turbulent intensity is registered at the interface between the high-speed flow and the low-speed flow close to the walls, mostly at the jet inlet. Together with this, in figures 5.10, 5.11 are presented the contours velocity magnitude distributions of the URANS simulation.

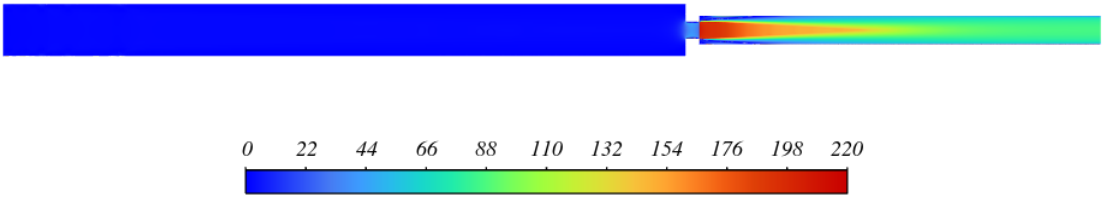

Figure 5.10: URANS simulation, general velocity magnitude distribution [m/s].

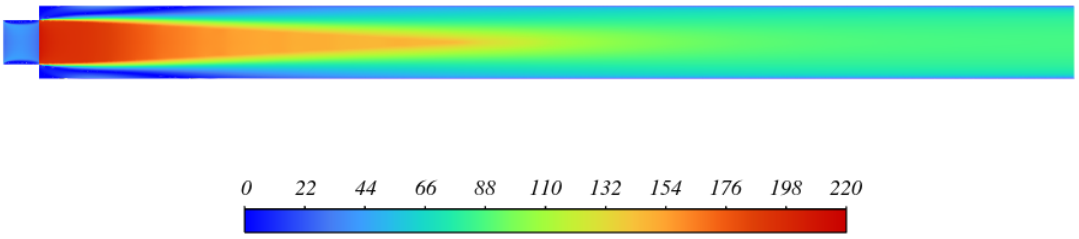

Figure 5.11: URANS simulation, velocity magnitude distribution in the premixer and combustion chamber [m/s].

For future comparisons, the monitor of the total heat transfer rate has been considered, followed by a Fast Fourier Transform (FFT) of the final portion of a signal, once reached a statistically steady condition. Hereinafter, the reader can see in figure 5.12, the portion of the signal that has been considered, from 0.65 to about 0.70 seconds. In figure 5.13 the FFT of the signal is proposed, with the power spectral density (PSD) on the vertical axis.

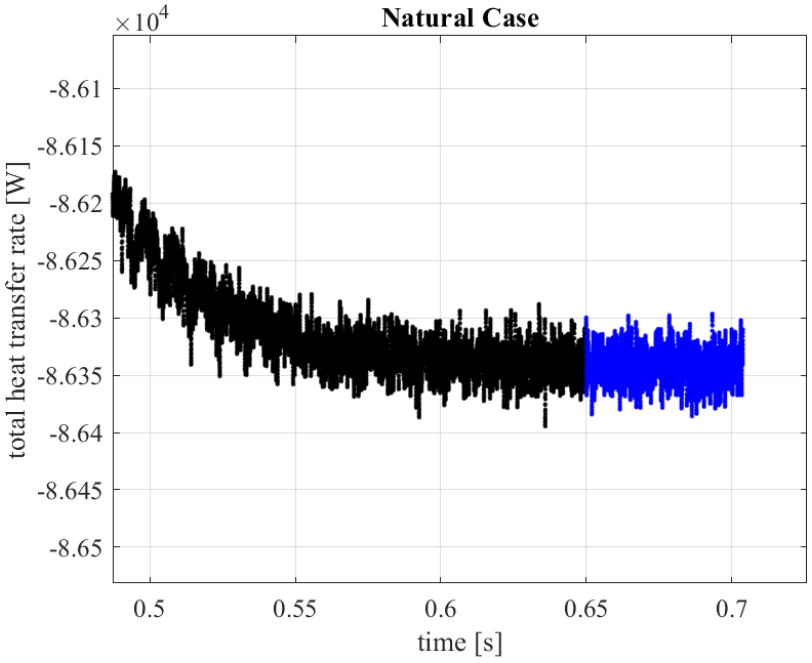

Figure 5.12: Monitor of the total heat transfer rate, and portion of the signal for the FFT (blue).

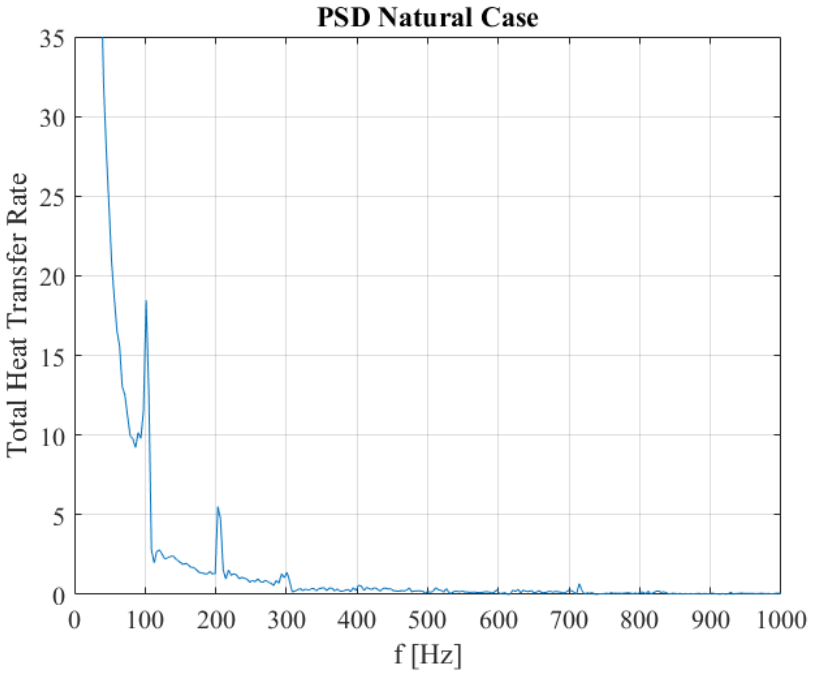

Figure 5.13: Fast Fourier Transform of the total heat transfer rate.

From figure 5.13, without taking into consideration the value of the PSD that goes to infinity as the frequency approaches the zero value, one can see that the main frequency is about 100 Hertz, followed by its harmonics distinguishable at about 200 and 300 Hertz.

5.4.3 Numerical tests for different forcing terms

In this subsection, the thermoacoustic instabilities of the combustor are investigated. With the aim of doing this, the temperature of the flame is now controlled in time. For the next simulations, it has been used the same setup of the unsteady natural case, with the difference that a forcing term has been introduced. The general formula that has been implemented is

$$T = 2000 + A \cdot 2000 \cdot cos(2\pi \cdot f \cdot t) \quad [K] \tag{5.1}$$

where A is a percentage of 2000 Kelvins, set equal to 0.1, 1, 10%, in this way three cases have been defined, t is time, and f stands for frequency, which varies from 50 to 450 Hz, with a step of 50 Hz. As example, a graphical solution of the temperature distribution is displayed in figure 5.14, for the case of 200 Hz and 10% of 2000 K. Twenty-seven cases in total have been tested, each of them has brought the system to a stable limit cycle.
Again, as example, in the the subsequent figures are presented the limit cycles reached for the 10% case at 100 Hz. In figure 5.15 is presented a limit cycle for the total heat transfer rate, which involves the entire control volume. Instead, in figure 5.16 one can see the limit cycle expressed with the absolute pressure measured at

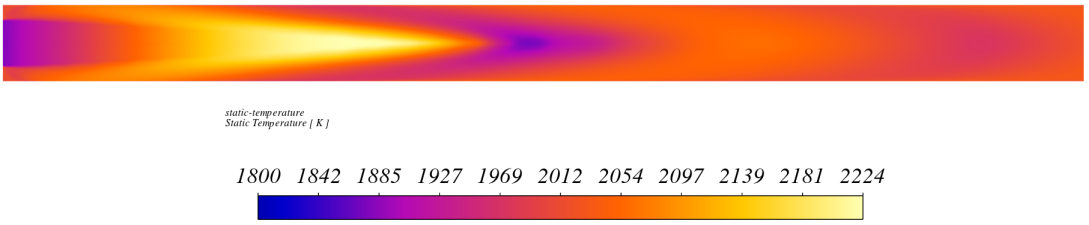

Figure 5.14: Temperature contour for the 10% case at 200 Hz.

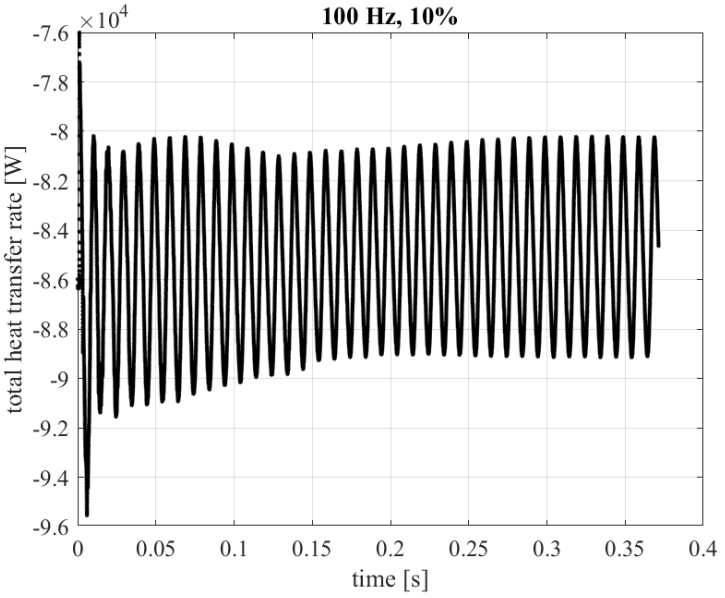

Figure 5.15: Total heat transfer rate limit cycle for the 10% case at 100 Hz.

point 4 located in the combustion chamber duct (for the coordinates of point 4, please see table 5.3).

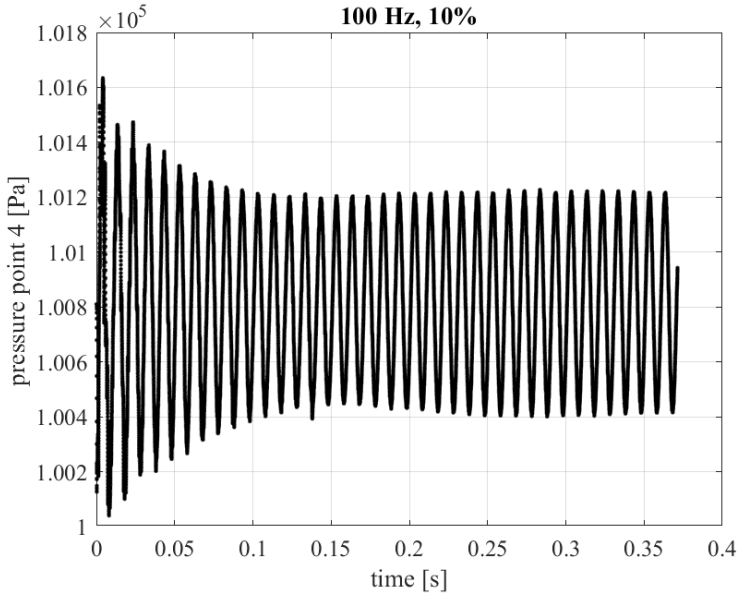

Figure 5.16: Pressure in point 4 for the 10% case at 100 Hz.

We now want to compare the different amplitudes of the limit cycles for the total heat transfer rate obtained for each case. We have to keep in mind that the signals are characterized by high peaks, they are not physical but only a result of the numerical calculations, thus they are not relevant. For this purpose, it is needed to introduce a proper formula for calculating the peak to peak amplitude of the signal. Once a statistically steady condition is obtained, we follow a series of steps:

- Selection of a time interval inside the stabilized signal.
- Calculation of the mean value of the cropped signal and subtraction to the signal itself to highlight the oscillations.
- Calculation of the root mean square (RMS) of the new signal.
- Research of the local maxima bigger than the RMS, and the local minima smaller than -RMS.
- Mean of the peaks values.

This should give a generalized value of the peak to peak amplitude of the limit cycle. In figure 5.17, a graphical explanation of the previous steps is shown. For this explanation, the case for 0.1% of forcing term at 350 Hz has been chosen. For this case, the peak to peak amplitude results to be equal to 218.3 W.

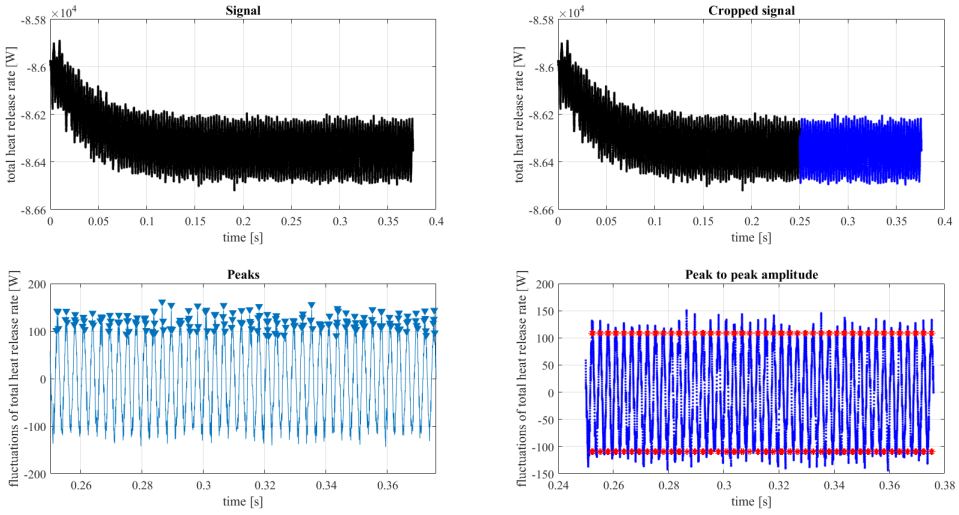

Figure 5.17: Peak to peak amplitude definition (350 Hz, 0.1%).

The same process has been followed for each case, and for different monitors, such as pressure and heat transfer rate. In the following figures are presented the trends of the peak to peak amplitudes of the limit cycles for the heat transfer rate and the pressure evaluated at point 4, located in the combustion chamber duct, for the three different cases and for different frequencies. From top to bottom: 0.1, 1, 10% case. In figure 5.18, the plot for the heat transfer rate is presented. We can see that, as expected, all the three plots show the same trend. With a global maximum at 50 Hz, and a subsequent local maximum at 300 Hz. The global minimum is for 100 Hz.

This is valid for all the three three cases, the corresponding values for the differ from one another by about a power of ten. In figure 5.19, the reader can find the plot of the limit cycle amplitudes for the pressure signals measured at point 4. In this case, differently from the heat transfer rate, we have a global maximum at 300 Hz, the global minimum is found at 50 Hz. The interpolation of the sample points has been conducted thanks to a Piecewise Cubic Hermite Interpolating Polynomial (PCHIP) on the software MATLAB.

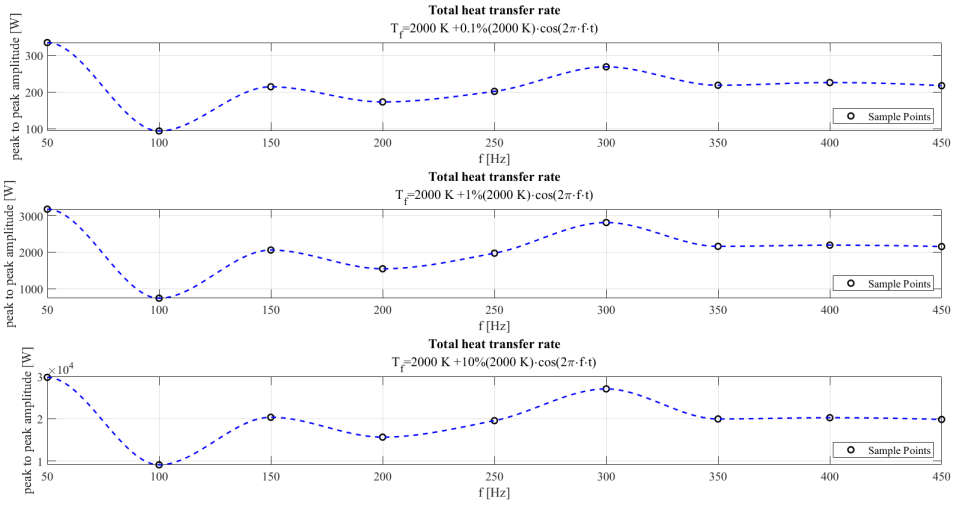

Figure 5.18: Interpolation of limit cycle amplitudes of heat transfer rate signals. From top to bottom: 0.1, 1, 10% case.

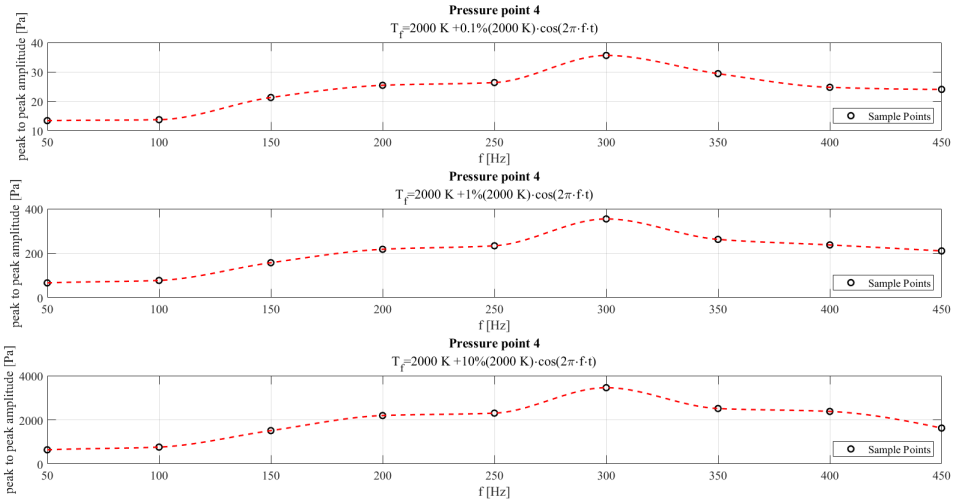

Figure 5.19: Interpolation of limit cycle amplitudes of pressure signal in point 4. From top to bottom: 0.1, 1, 10% case.

5.5 Control of the flame energy source term

Once gained some experience with a fixed temperature variation of the flame, the next step has been acting on the source term of the energy equation for the combustion region. The next steps are similar to the ones followed for the control of the flame temperature.

5.5.1 The steady case for a constant heat source

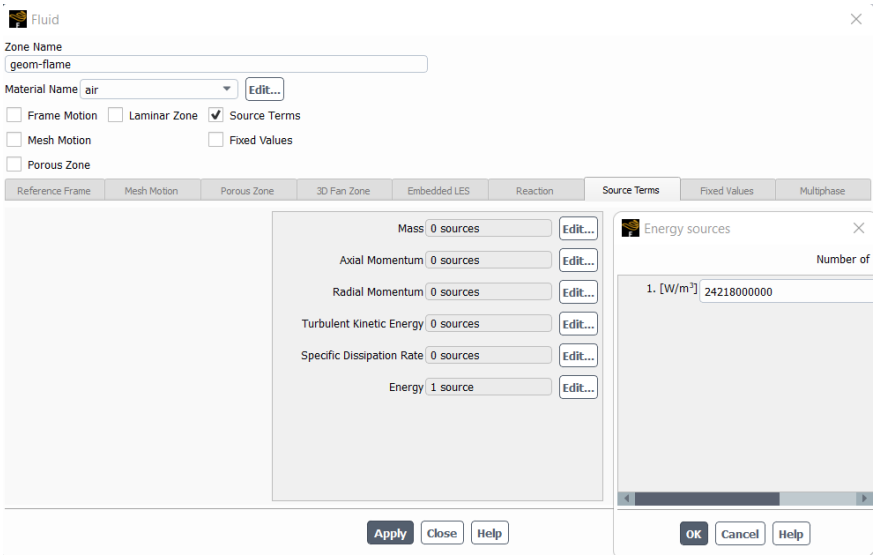

Figure 5.20: RANS simulation, general temperature distribution [K].

The first one has been finding a proper constant value for the source term of the energy equation, able to grant a temperature distribution in the combustion chamber around 2000 Kelvins. This first investigation has been conducted thanks to RANS simulations. After some attempts, a value of 24218000000 $\frac{W}{m^3}$ has been chosen as the right starting value. In figure 5.21, the reader can see the temperature distribution inside the all domain for the steady case of a constant heat source.

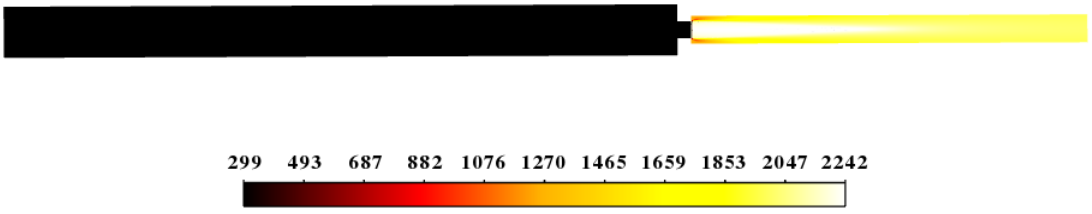

Figure 5.21: RANS simulation, static temperature distribution [K].

We can see that, after the potential core of the hot jet flow the temperature near the outlet is around 2000 K. We now consider the same locations used in section 5.4.1, table 5.1, in order to compare the mean results with the ones obtained with the TALOM approach. As one can observe in table 5.4, the results are very close to the ones of the table 5.2.

Area weighted average	Axial velocity [m/s]	p [Pa]	ρ [$\frac{kg}{m^3}$]	T [K]
1.5 m	3.172	105082	1.220	299.995
1.72 m	29.046	103946	1.210	299.328
2 m	73.718	101042	0.1811	1952.227
2.5 m	73.695	101046	0.1764	1995.825

Table 5.4: Results from the steady simulation for a constant heat source of 24218000000 $\frac{W}{m^3}$ for the flame energy equation.

The **net total heat transfer rate** provided by the model combustor is **-85971 W**, this value is negative because the heat flux is globally outgoing from the control volume.

5.5.2 The unsteady case for a constant heat source

In this subsection, we present the results for the unsteady case of a constant heat source of 24218000000 $\frac{W}{m^3}$ for the flame energy equation. The aim of this calculation is to have a better starting condition for future numerical tests and investigate the frequencies that characterized the unsteady case. The same setup and monitors of the URANS simulation of the fixed temperature case has been implemented for this test and the successive ones, please see section 5.4.2. It is important to point out that a CFL number with a value less than one is necessary to grant convergence, as a consequence a time step of $2.5e-5$ seconds has been set.
The software Fluent let us evaluate the overall sound pressure level (OASPL) as defined in section 2.1. So, in order to have an idea of the loudness of the model combustor during its operating condition, we have considered the trace of acoustic pressure sampled in points 1 and 5 (please check their coordinates at table 5.3) once reached a statistically steady condition. The OASPL results to be equal to 56 dB for point 1, similar to a normal conversation, and 9 dB for point 5.
In the following figures 5.22, 5.23 are presented a contour for the turbulent intensity and one for the axial velocity distribution.

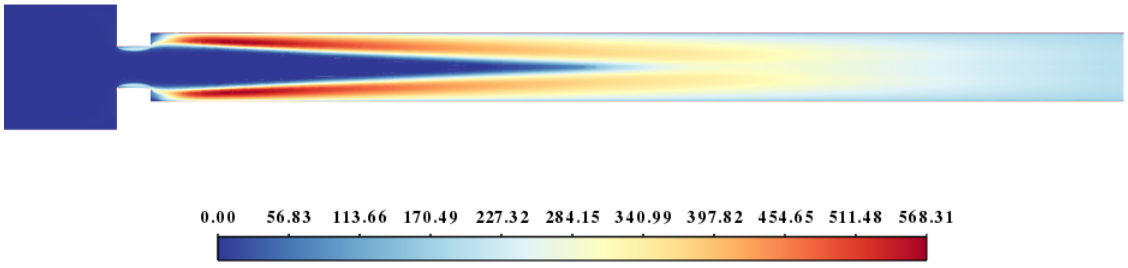

Figure 5.22: URANS simulation,turbulent intensity distribution [%].

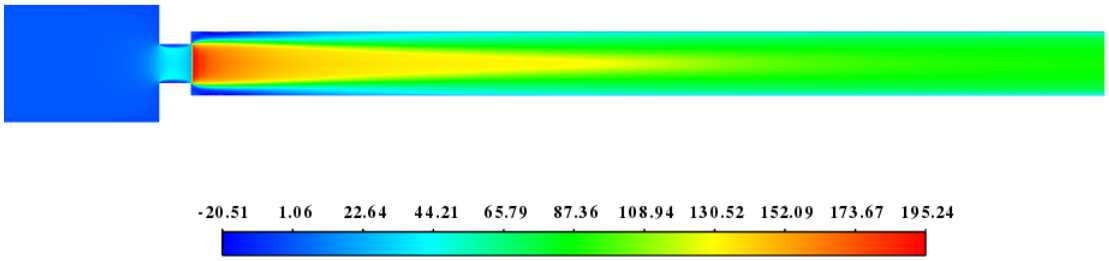

Figure 5.23: URANS simulation, axial velocity distribution [m/s].

Again, we can observe a similar pattern to the ones of the fixed temperature case. Once reached convergence, we cropped the signal for the total heat transfer rate from 0.7 to 0.93 seconds.

5.6 Unsteady heat addition

We now want to investigate the unstable behavior of the model combustor from a thermoacoustic point of view. with this intention, the first thing to do is to implement an unsteady heat addition model. Considering the source term of the energy equation of the flame zone, it has been added to the constant value of $2.4218 \cdot 10^{10} \frac{W}{m^3}$ a fluctuating term, yielding to a new formula of the type:

$$Q_{source} = 2.4218 \cdot 10^{10} - \beta \frac{\rho_{bf}\, c_{bf}^2}{(\gamma - 1)\, s_f} [u(d) - U(d)] \quad \left[\frac{W}{m^3}\right] \tag{5.2}$$

The fluctuating term of this formula aims at resembling the flame transfer function described in section 4.2.4, we chose this flame model because it resulted to be easier to implement on Ansys Fluent. β is a constant and it has been set equal to 1, 1.5, 1.6, 1.7, 2. The subscript *bf* stands for *before flame*, it represents the area-weighted average of density and sound speed profiles sampled at a distance of 1.7345 meters, right before the flame, which starts at 1.7345 meters. Instead of a time delay τ, which is hard to implement directly on the code, we have chosen a spatial delay d considering the instantaneous fluctuations of axial velocity, sampled not before the flame. This axial distance from the flame has been set equal to 5, 17, and 20 mm, as to distinguish three main cases, please see figure 5.24. The variation of the two parameters β and d gives brings to a total of 15 cases. Another important aspect is that the flame transfer function adds to the constant heat source term a fluctuating term, which in turn depends on a fluctuating axial velocity. This fluctuation is mimicked by considering the instantaneous area-weighted average of the axial velocity profile $u(d)$, sampled at a specific distance d during the URANS simulation, minus the area-weighted average of axial velocity obtained thanks to a RANS (steady) simulation at the same location, $U(d)$. The flame thickness is indicated with s_f, the utilized value is not the flame thickness defined in the mesh section (2.5 mm), s_f is obtained starting from the mean heat source term calculated with the TALOM approach, see subsection 4.2.1 ($\bar{q} = 22216000 \quad W/m^2$). Once assessed 24218000000 $\frac{W}{m^3}$ as the proper mean source term for having an almost uniform temperature of 2000 K at the end of the combustor,

s_f is obtained thanks to the ratio of these two values: $s_f = \frac{22216000 \quad W/m^2}{24218000000 \quad W/m^3} = 0.92$ mm.

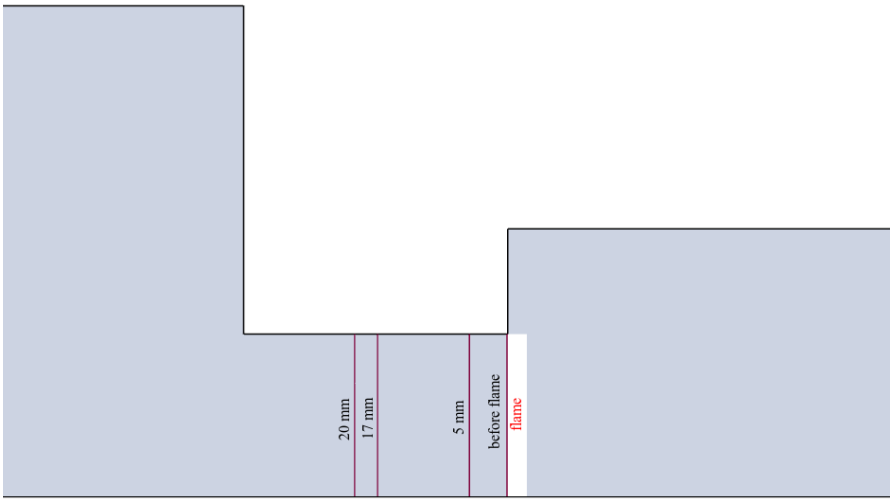

Figure 5.24: Sampling lines at different distances for the implementation of an unsteady heat addition.

5.7 Stable cases

With regard to the decaying cases, in the next sections are presented the results of the various numerical tests done for different distances d that represent a readaptation into a space delay of the time delay τ (the convection time from fuel injection to combustion), together with a variation of the constant β. Every simulation starts from the statistically steady condition obtained from the URANS simulation with a constant heat release rate provided by the flame (24218000000 W/m^3), together with a fluctuating term where a specific value of β and spatial delay d has been chosen. The same workflow is followed also for the analysis of the unstable cases. Once reached a statistically steady condition, from an acoustic point of view, the overall sound pressure levels measured in point 1 and 5 have an average value of 81 dB and 65 dB, respectively.

5.7.1 d = 5 mm

Considering the case for $d = 5$ mm, the first three simulations for β equal to 1, 1.5, and 1.6, have decayed to the statistically steady state characterizing the first simulation with constant heat source. In figure 5.25 is presented the mass flow rate and total heat

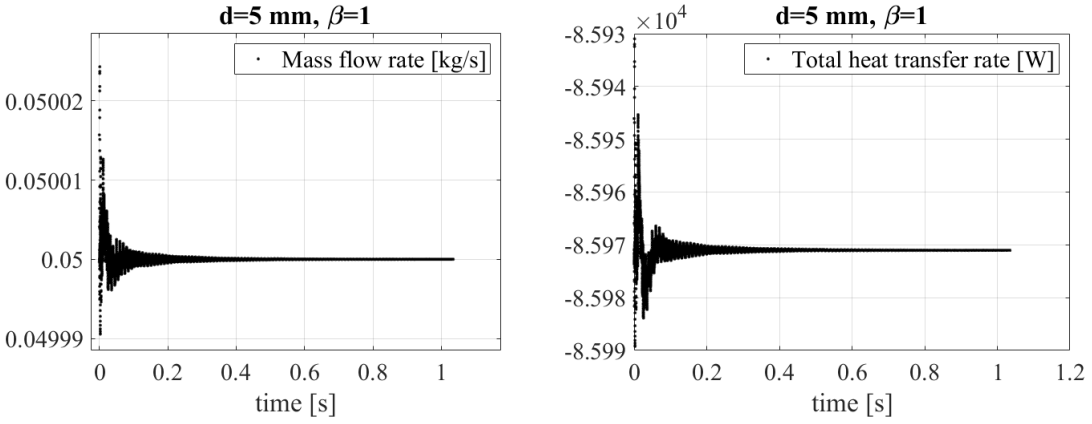

Figure 5.25: Mass flow rate and total heat transfer rate signals for d=5 mm and $\beta = 1$.

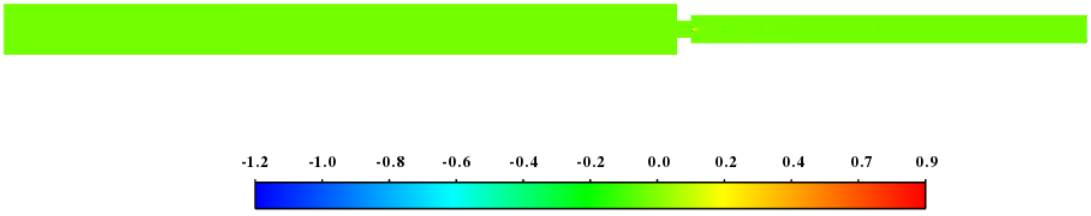

Figure 5.26: Acoustic pressure contour for d=5 mm and $\beta = 1$ [Pa].

transfer rate signals for the case of β equal to 1, the reader can see that are practically no fluctuations, and no limit cycle condition is reached. In figure 5.26 is presented a contour of the acoustic pressure inside the modeled combustor. Once reached a statistically steady condition, no pressure waves are detected, instead the value of the pressure fluctuations is almost zero everywhere. The same considerations can

be done for the case of β=1.5 and for β=1.6, figures 5.27, 5.28, 5.29, 5.30.
For the β=1.5 case, the simulation has been stopped earlier than the β=1 case, because it was already clear that a decay condition has been established.
Considering the β=1.6 case, the simulation has lasted longer and it has been stopped before the complete statistically steady condition, although a clear decay is notable. The longer simulation time results to be a sign of vicinity, in terms of the parameter β, to an unstable condition.

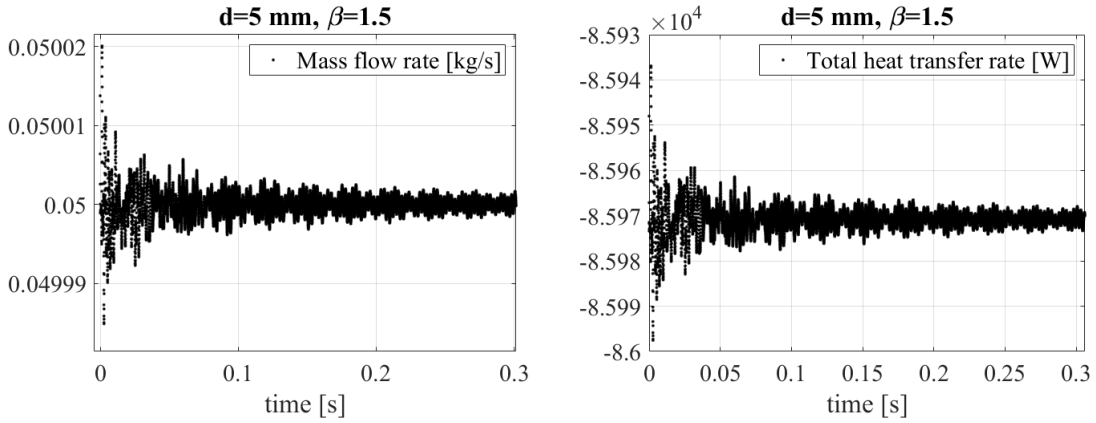

Figure 5.27: Mass flow rate and total heat transfer rate signals for d=5 mm and β = 1.5.

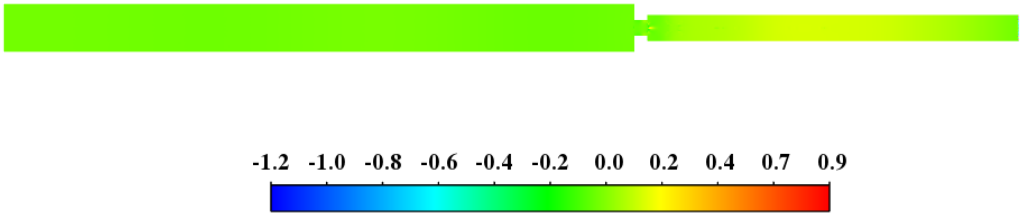

Figure 5.28: Acoustic pressure contour for d=5 mm and β = 1.5 [Pa].

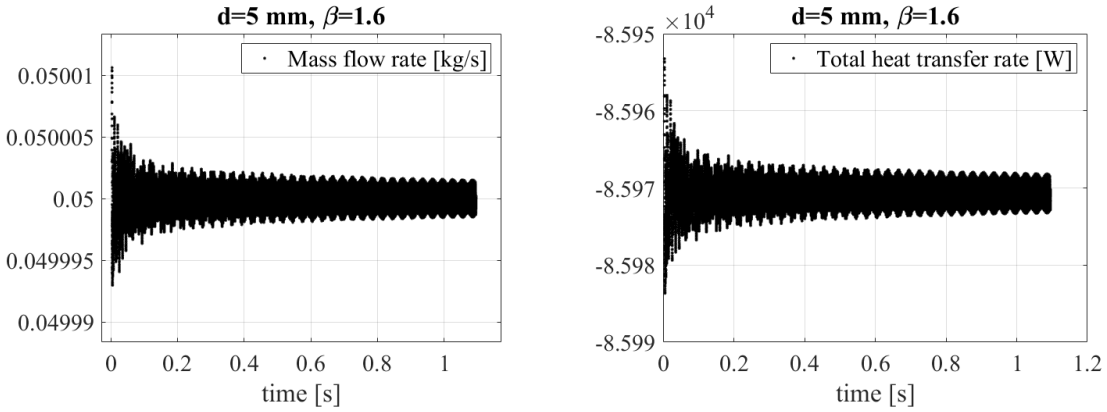

Figure 5.29: Mass flow rate and total heat transfer rate signals for d=5 mm and β = 1.6.

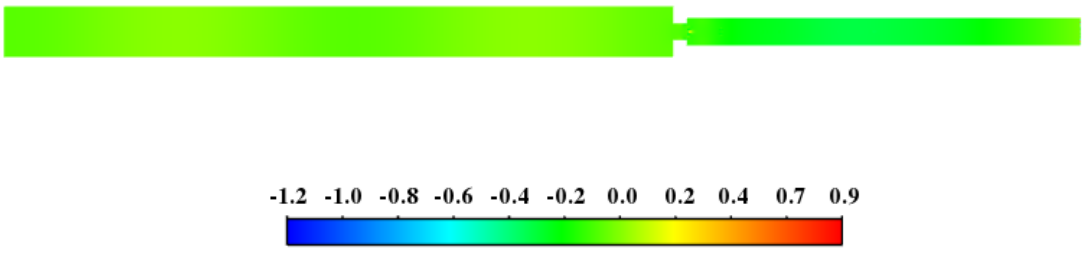

Figure 5.30: Acoustic pressure contour for d=5 mm and β = 1.5 [Pa].

5.7.2 d=17 mm

Analogous considerations can be done for the other distances. In the following figures are presented the decaying results for d=17 mm, please see figures 5.31-5.34. The main difference with the d=5 mm case is that there is decay just for β equal to 1 and 1.5. For the latter case, the simulation has been interrupted early, as soon as a decay condition has been detected.

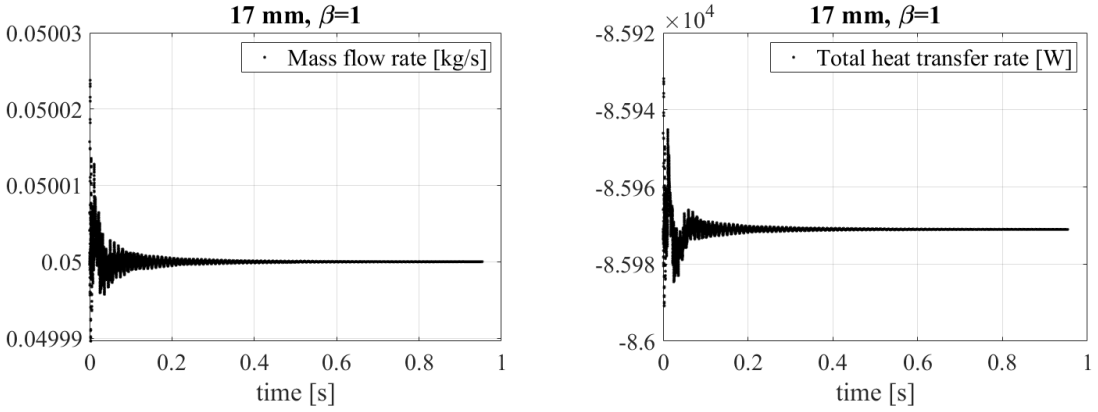

Figure 5.31: Mass flow rate and total heat transfer rate signals for d=17 mm and β = 1.

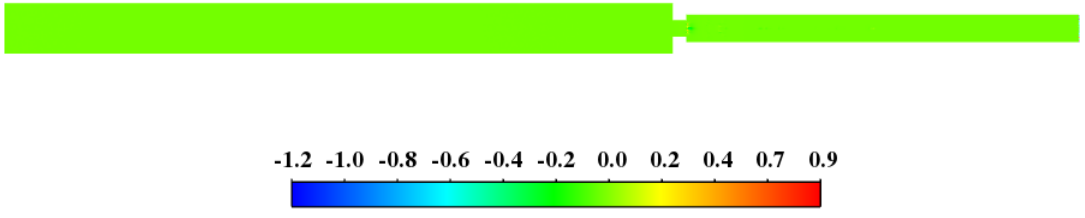

Figure 5.32: Acoustic pressure contour for d=17 mm and β = 1 [Pa].

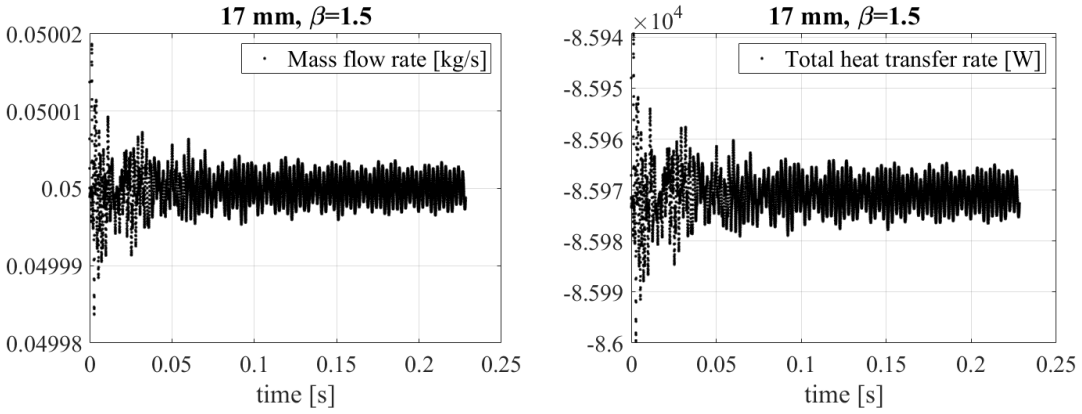

Figure 5.33: Mass flow rate and total heat transfer rate signals for d=17 mm and β = 1.5.

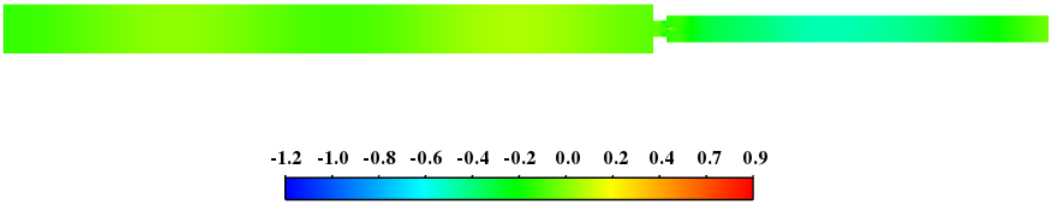

Figure 5.34: Acoustic pressure contour for d=17 mm and β = 1.5 [Pa].

5.7.3 d=20 mm

In the following figures are presented the decaying results for d=20 mm, please see figures 5.35-5.37. Likewise, for this condition, there is decay for β equal to 1 and 1.5.

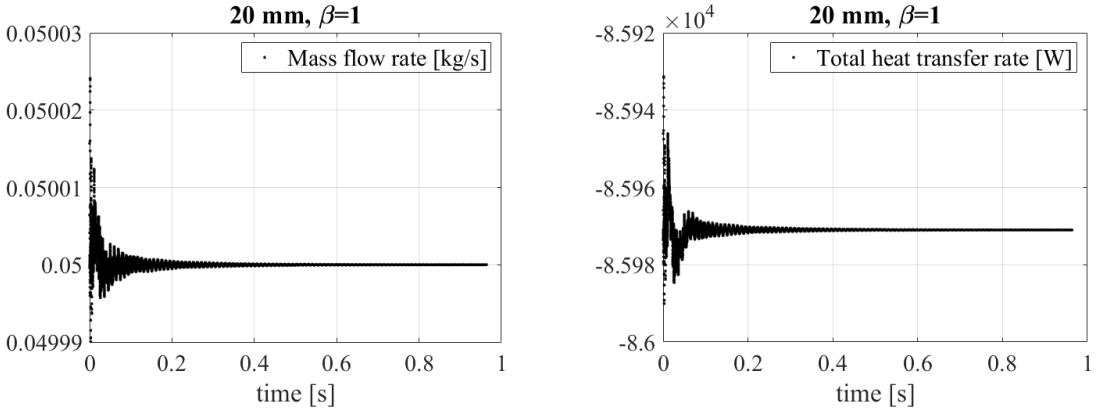

Figure 5.35: Mass flow rate and total heat transfer rate signals for d=20 mm and β = 1.

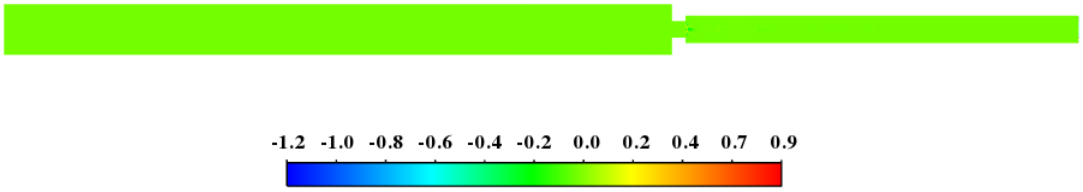

Figure 5.36: Acoustic pressure contour for d=20 mm and β = 1 [Pa].

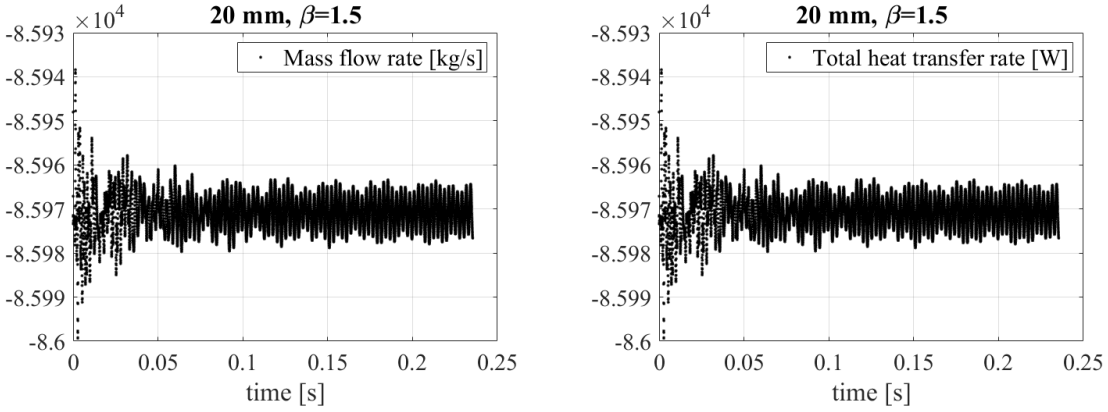

Figure 5.37: Mass flow rate and total heat transfer rate signals for d=20 mm and β = 1.5.

5.8 Unstable cases

With the aim of finding an unstable condition of the model combustor, the parameter β has been raised more for every of the three main cases. In the following subsections are presented the principal results for each of the numerical tests, in the next section, the focus goes on the limit cycle condition, analyzed and quantified employing the acoustic energy.
Once reached the limit cycle condition, from an acoustic point of view, the overall sound pressure levels measured in point 1 and 5 have an average value of 156 dB and 146 dB, respectively, which are way over the threshold of pain.

5.8.1 d=5 mm

Switching the parameter β from 1.6 to 1.7 has lead to significant outcomes, in this situation a limit cycle condition is reached. The same can be said for the β=2 case. The first transient signal proposed is the volume-average temperature of the flame zone, intending to correlate this value with the fixed temperature cases of section 5.4. For d equal to 5 millimeters, the first unstable case found is when switching from β=1.6 to β=1.7, and also going from 1.7 to β=2, figure 5.38.
For the first case, d=5 mm and β=1.7, the flame temperature starts to have significant fluctuations from one second; at around 1.4 s the limit cycle condition is reached and the peak-to-peak amplitude is about 650 K. Please note that for these cases the heat provided by the flame is controlled, not its temperature, so it is normal to have a starting value of 1250 K, this is because the flow passes through the flame, heats up, and then arrives at 2000 K in the successive combustion chamber. For the β=2 case, similar conclusions can be drawn. Here the peak-to-peak amplitude of the limit cycle is of the order of 1100 K and this state is achieved earlier, from 0.5 s. Concerning the previous case, for β equal 2, we also observe more oscillations in the signal.

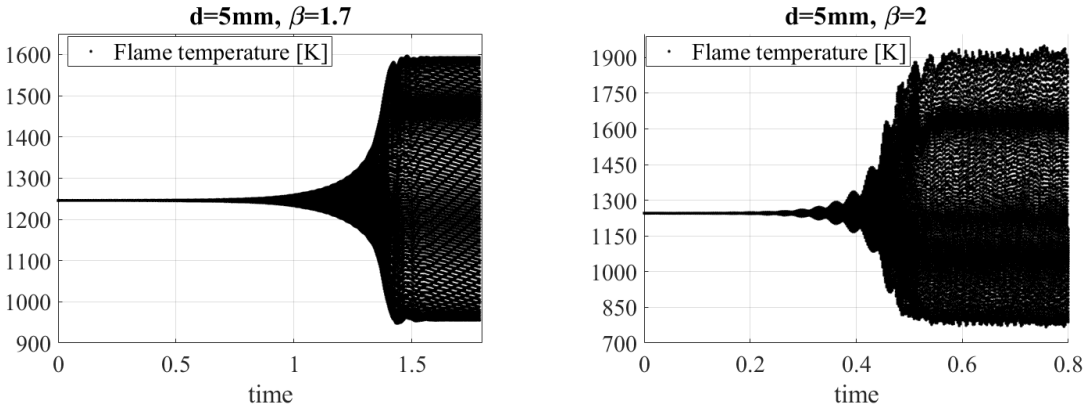

Figure 5.38: Signals for the temperature volume-average of the flame zone for d=5 mm, β = 1.7, and β = 2 [K].

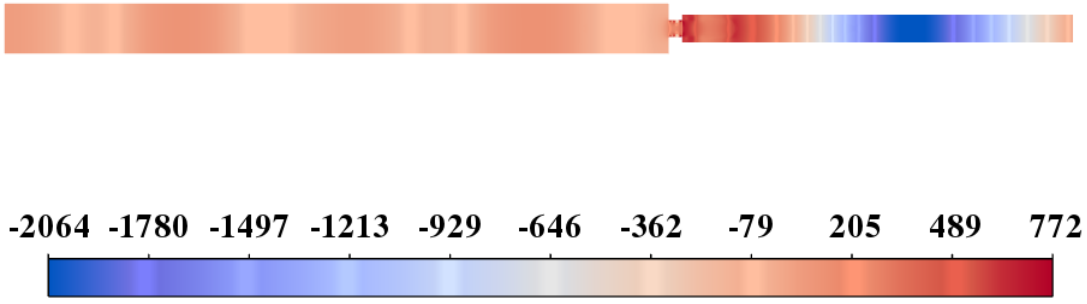

Figure 5.39: Acoustic pressure contour for d=5 mm and β = 1.7 [Pa].

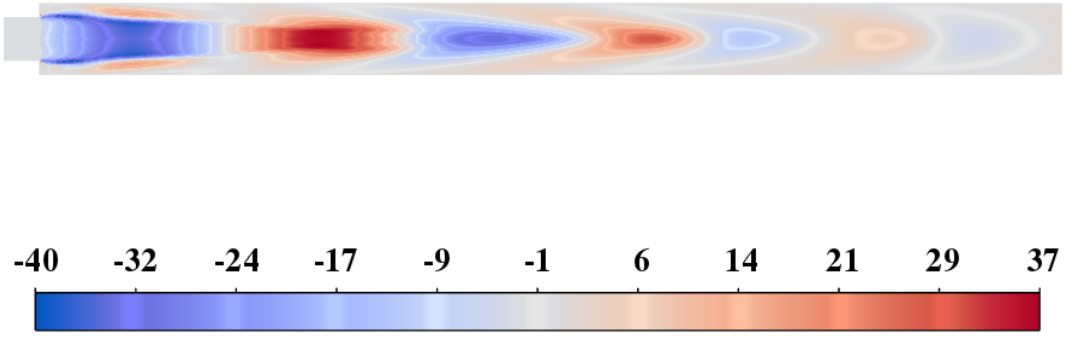

Figure 5.40: Temperature fluctuations contour for d=5 mm and β = 1.7 [K] (sections 2 and 3).

In figures 5.39, and 5.40 are presented the contours of the acoustic pressure and temperature fluctuations inside the modeled combustor, for d=5 mm and β = 1.7 . These contours are extracted at the end of the corresponding numerical simulation, when the limit cycle is well established. The first contour highlights the pressure waves, in the first section three of them are clearly distinguishable, and in the combustion chamber, only one strong wave is present. In the second contour, the reader can observe multiple portions of hot and cold fluid outgoing in the combustor, the fluctuations are higher the closer to the flame. Finally, a varicose configuration is notable, this is probably due to the axisymmetric flow condition imposed.

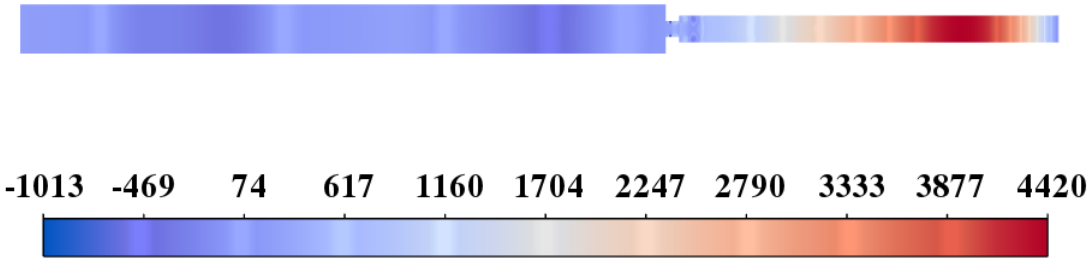

Figure 5.41: Acoustic pressure contour for d=5 mm and β = 2 [Pa].

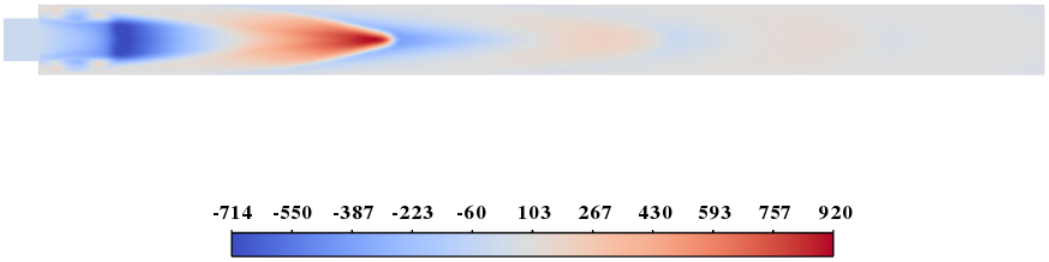

Figure 5.42: Temperature fluctuations contour for d=5 mm and β = 2 [K] (sections 2 and 3).

In figures 5.41, 5.42, are presented equivalent contours for the pressure and temperature oscillations for the β=2 case. Again, one can see two pressure waves inside the plenum and one stronger compression wave in section three. This is also emphasized in figure 5.43, where the acoustic pressure distribution on the axis of the model combustor is plotted. It is a clear representation of a modeled combustion instability, with a robust pressure wave downstream of the modeled flame.

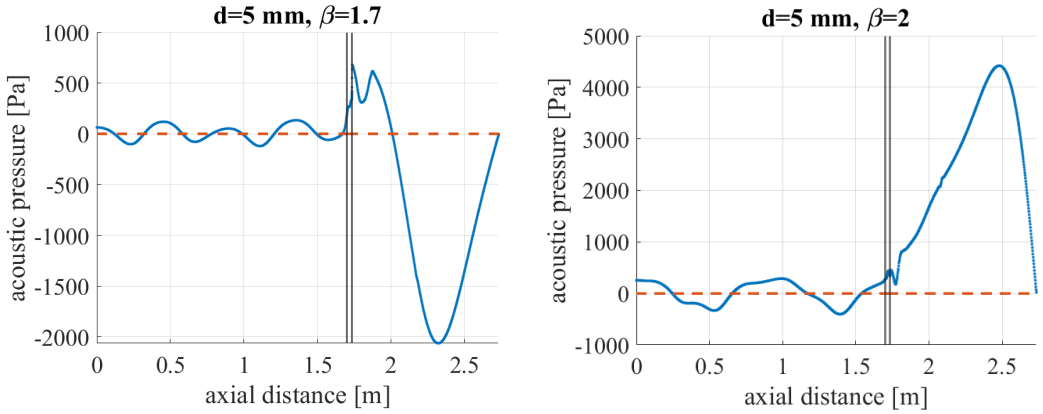

Figure 5.43: Plot of the acoustic pressure distribution along the axis of the combustor for d=5 mm, β = 1.7, and β = 2 [Pa].

5.8.2 d = 17 mm

The next case presented is for d=17 mm. For this spatial delay, a stable limit cycle configuration is achieved by setting β equal to 1.6, 1.7, and 2. The larger the β, the earlier the instability takes effect, together with larger temperature fluctuations. The β=2 case is characterized by limit cycle oscillations which tend to be more unstable. It could be reasonable to justify this behavior because the code may find difficulties in obtaining convergence.

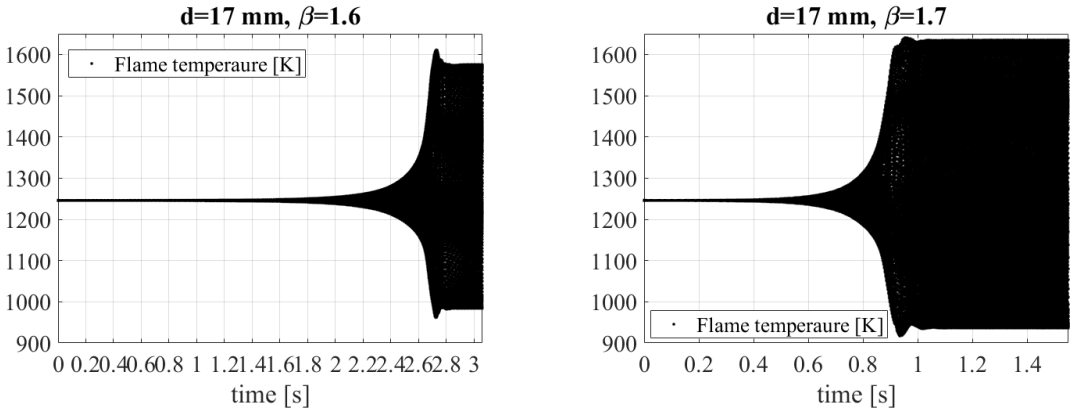

Figure 5.44: Signals of the temperature volume-average of the flame zone for d=17 mm, $\beta = 1.6$, and $\beta = 1.7$ [K].

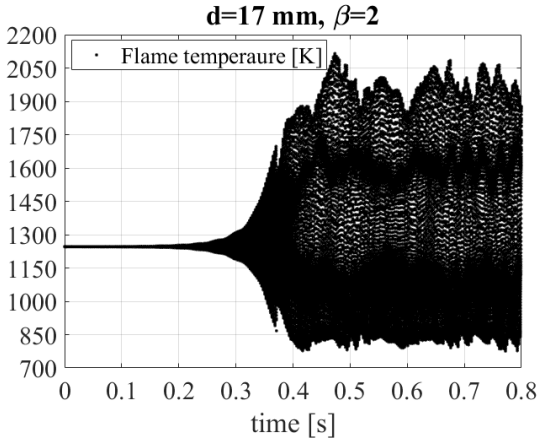

Figure 5.45: Signal of the temperature volume-average of the flame zone for d=17 mm and $\beta = 2$ [K].

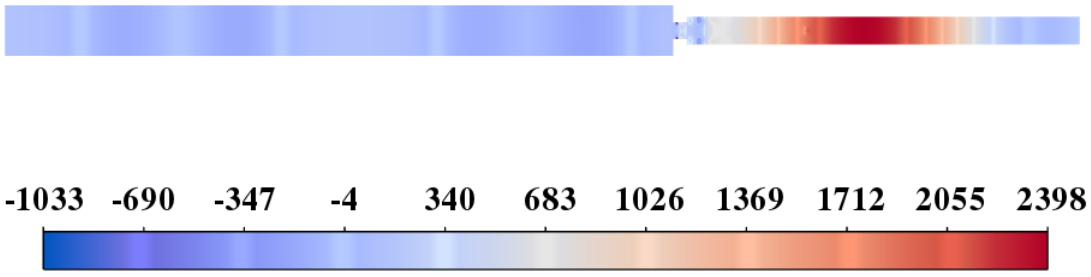

Figure 5.46: Acoustic pressure contour for d=17 mm and $\beta = 1.6$ [Pa].

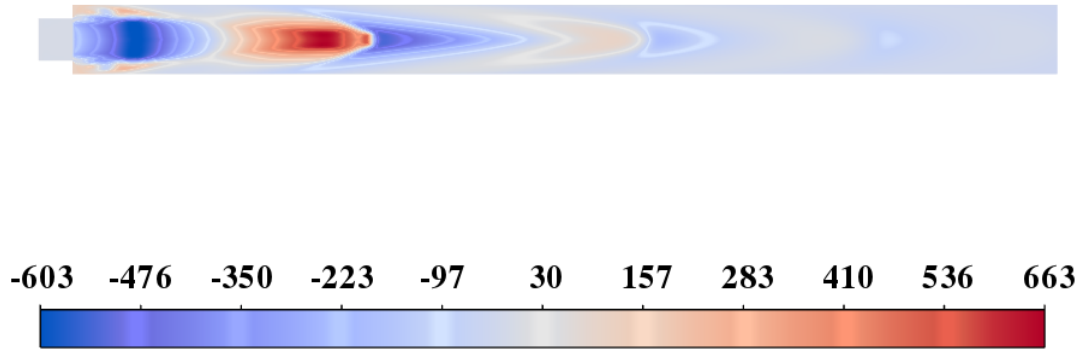

Figure 5.47: Temperature fluctuations contour for d=17 mm and β = 1.6 [K] (sections 2 and 3).

In figures 5.46, 5.48, and 5.50 are illustrated similar contours for the acoustic pressure for β equal to 1.6, 1.7, and 2, with d= 17 mm. Together with this, in figures 5.47, 5.49, and 5.51 are presented the temperature fluctuations contours. Again, these reported contours are extracted from the last instant of each numerical simulation.

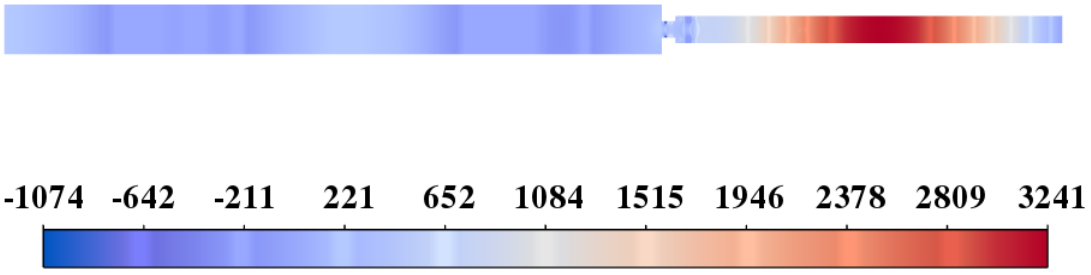

Figure 5.48: Acoustic pressure contour for d=17 mm and β = 1.7 [Pa].

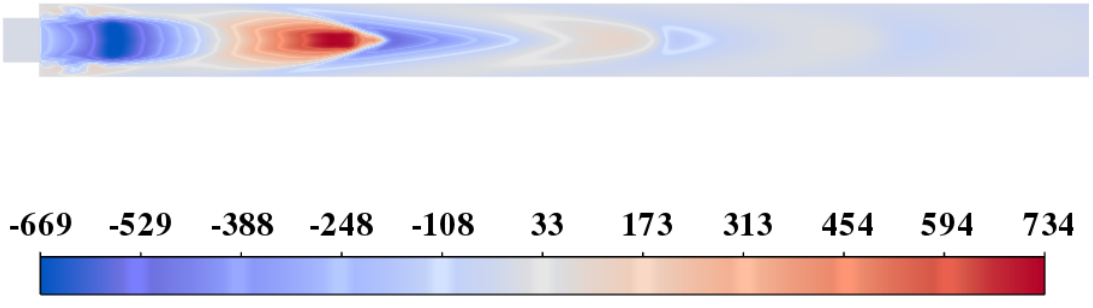

Figure 5.49: Temperature fluctuations contour for d=17 mm and β = 1.7 [K] (sections 2 and 3).

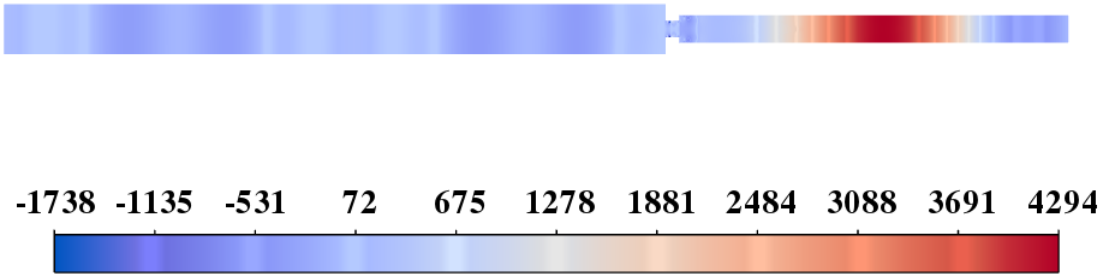

Figure 5.50: Acoustic pressure contour for d=17 mm and β = 2 [Pa].

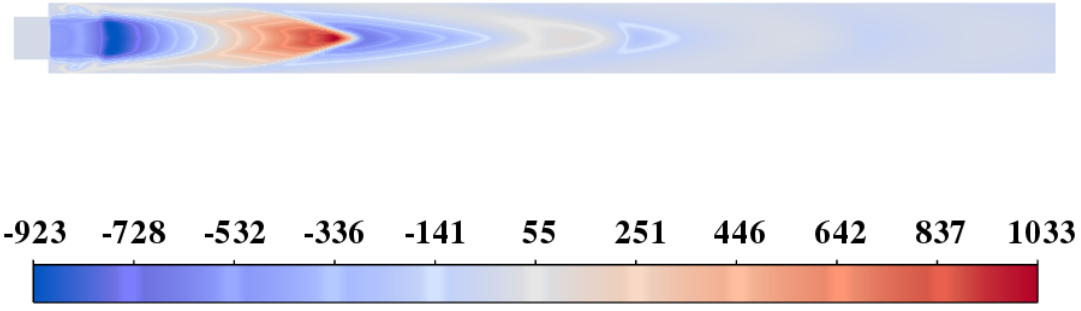

Figure 5.51: Temperature fluctuations contour for d=17 mm and β = 2 [Pa] (sections 2 and 3).

Finally, the plots of the acoustic pressure registered on the modeled combustor axis, are displayed in figures 5.52, 5.53, the vertical lines in grey represent the intersections plenum-premixer, premixer-combustion chamber, respectively. Here one can see that the waveforms in the plenum are different wit respect to the previous case of d set equal to 5 millimeters. Moreover, as reasonable, the pressure amplitudes in the third section are larger for a larger β.

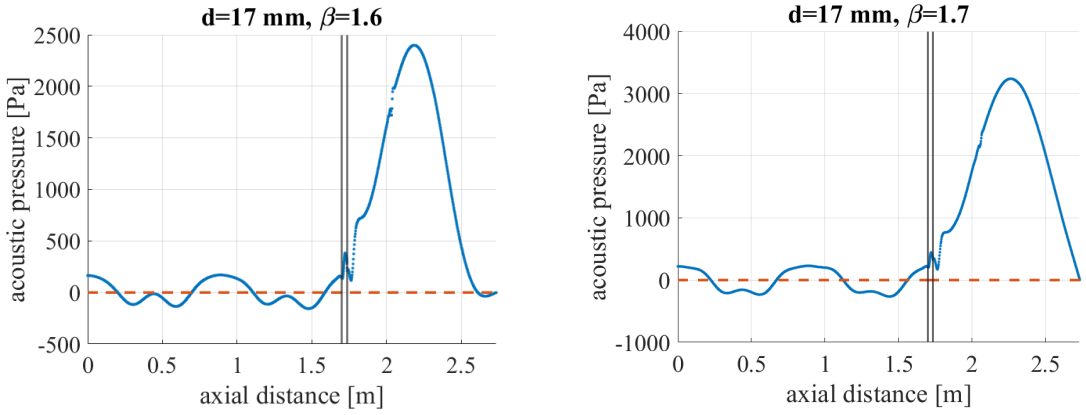

Figure 5.52: Plot of the acoustic pressure distribution along the axis of the combustor for d=17 mm, β = 1.6, and β = 1.7 [Pa].

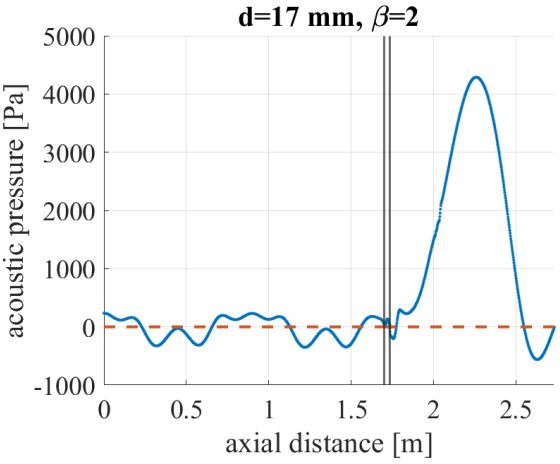

Figure 5.53: Plot of the acoustic pressure distribution along the axis of the combustor for d=17 mm and β = 2 [Pa].

5.8.3 d = 20 mm

The last investigation involves the spatial delay *d*=20 mm, the furthest position from the flame where is flow variables are sampled. The successive plots and contours are similar to the previous results of the other numerical tests. The flame temperature oscillations are close to the ones of the *d*= 17 mm case, again for β=2 the oscillations result to be more unstable. For all the three β cases, the pressure contours highlight two distinguishable acoustic waves inside the combustion chamber, to a smaller extent this is also clear in the acoustic pressure distributions along the modeled combustor axis , please see figures 5.62, 5.63. CHECK!!!

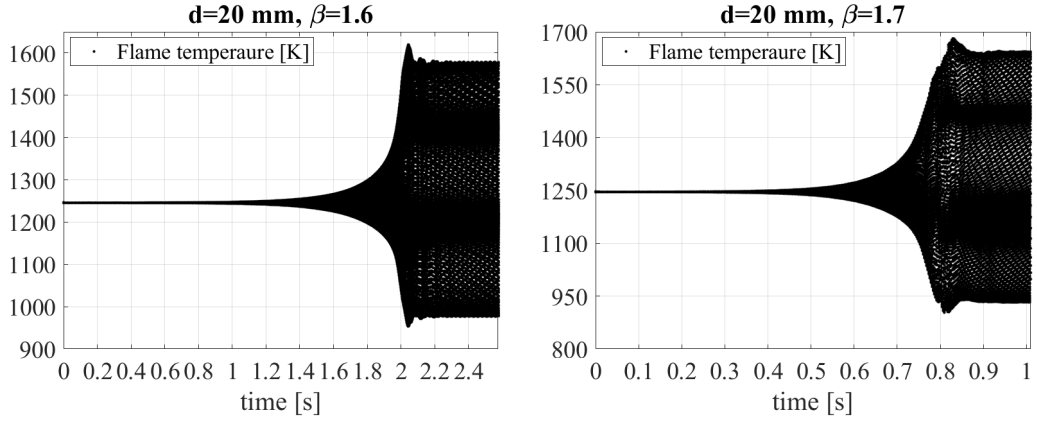

Figure 5.54: Signals of the temperature volume-average of the flame zone for d=20 mm, β = 1.6, and β = 1.7 [K].

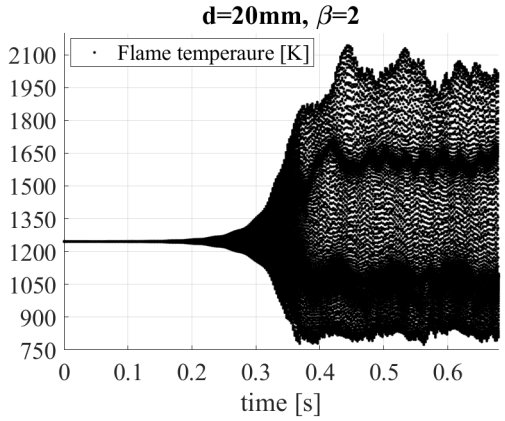

Figure 5.55: Signal of the temperature volume-average of the flame zone for d=20 mm and $\beta = 2$ [K].

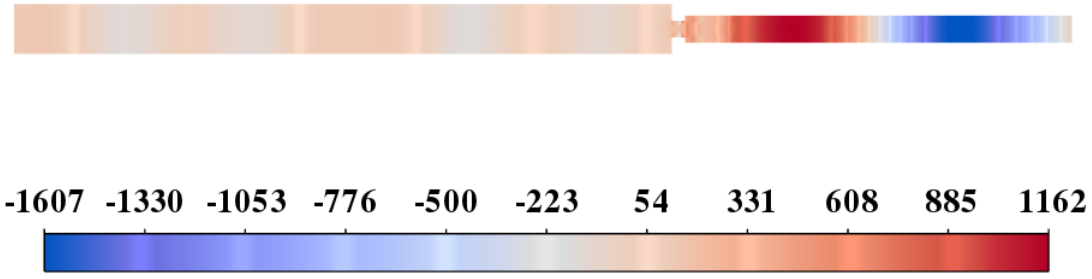

Figure 5.56: Acoustic pressure contour for d=20 mm and $\beta = 1.6$ [Pa].

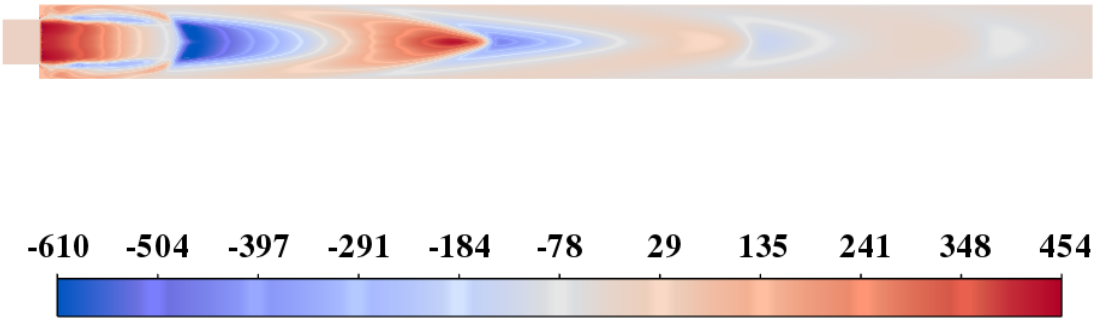

Figure 5.57: Temperature fluctuations contour for d=20 mm and $\beta = 1.6$ [K] (sect. 2 and 3).

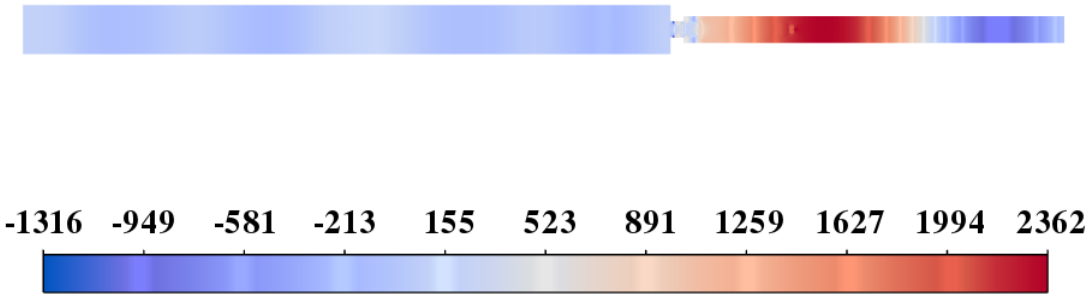

Figure 5.58: Acoustic pressure contour for d=20 mm and β = 1.7 [Pa].

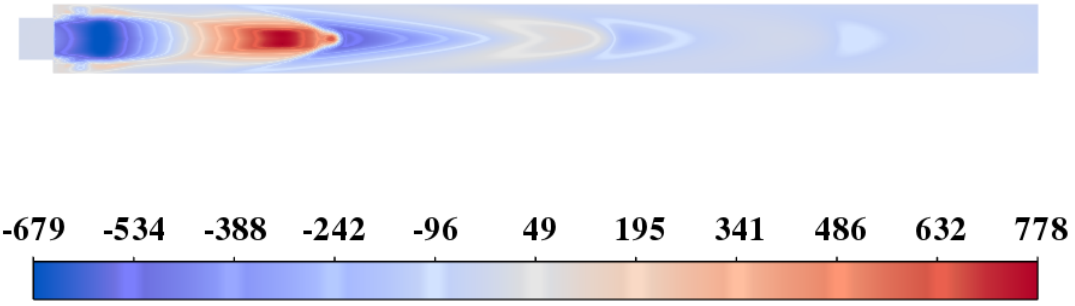

Figure 5.59: Temperature fluctuations contour for d=20 mm and β = 1.7 [K] (sect. 2 and 3).

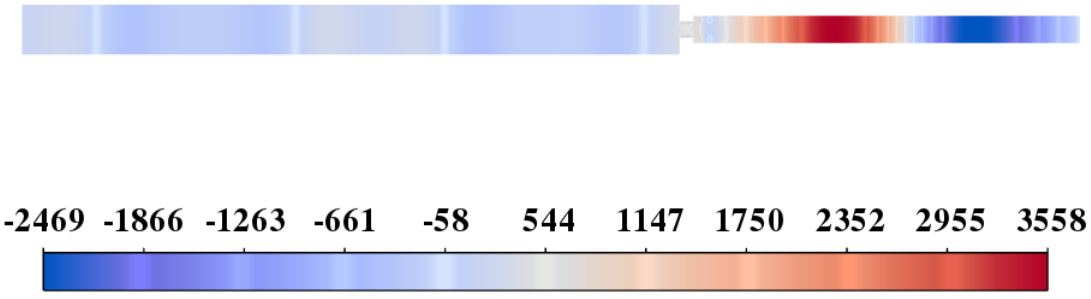

Figure 5.60: Acoustic pressure contour for d=20 mm and β = 2 [Pa].

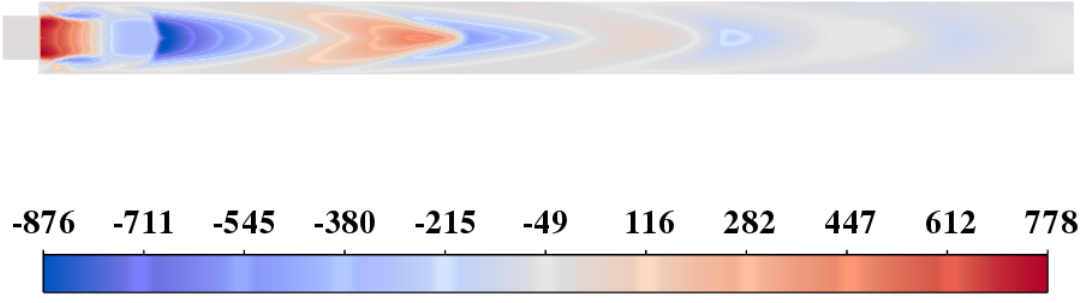

Figure 5.61: Temperature fluctuations contour for d=20 mm and β = 2 [K] (sect. 2 and 3).

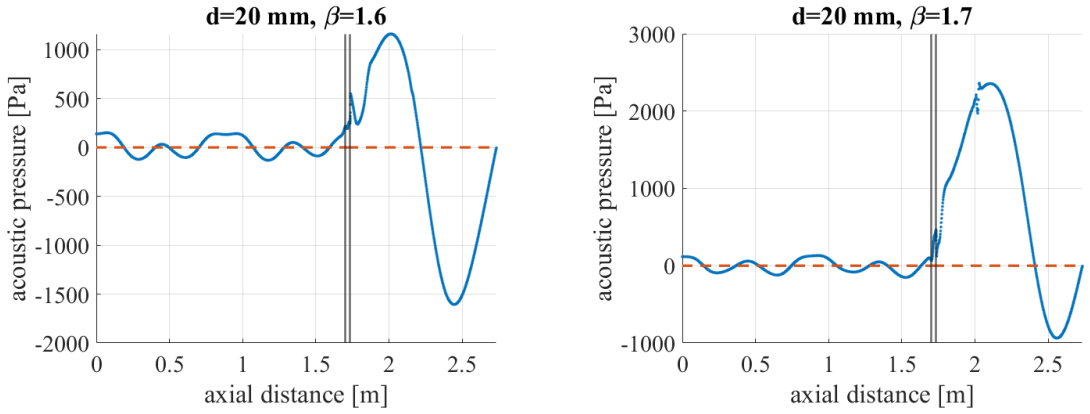

Figure 5.62: Plot of the acoustic pressure distribution along the axis of the combustor for d=20 mm, β = 1.6, and β = 1.7 [K].

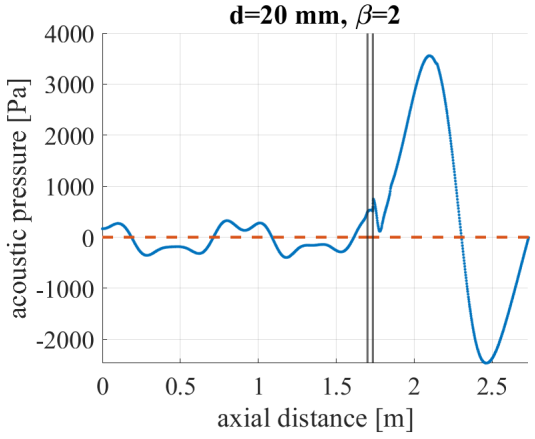

Figure 5.63: Plot of the acoustic pressure distribution along the axis of the combustor for d=20 mm and β = 2 [Pa].

5.9 Further analysis on the unstable cases

In this section, a comparison between the three space lags for a given value of β is firstly presented. In figure 5.64, are shown the flame temperature signals for the unstable cases obtained for β equal to 1.7 and 2, already presented in the previous section. This let us understand the influence of the space lag d. For both values of the constant β, the closer to the flame is the sampling for studying the combustion instability, the longer it takes to reach a limit cycle condition, together with reduced fluctuations. One can also notice that increasing the value of β leads to a drastic reduction in the time needed for instability to build up, with bigger peak-to-peak amplitudes.

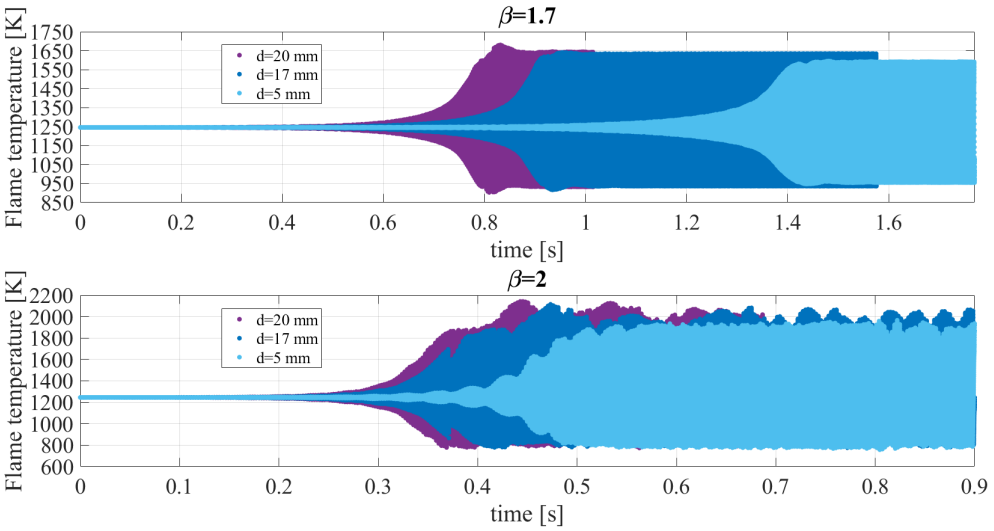

Figure 5.64: Unstable signals of the temperature volume-average of the flame zone [K] (β=1.7, β=2).

The different numerical tests are now examined and analysed by means of the acoustic energy. For this purpose, we recall the definition given in section 2.3, whose formula is reported hereinafter for completeness.

$$W_{acoustic} = W_{potential} + W_{kinetic} = \iiint_V \frac{p'^2}{2\bar{\rho}\bar{c}^2}\, dV + \iiint_V \frac{1}{2}\bar{\rho}u'^2\, dV \quad [J] \qquad (5.3)$$

The first investigation involves the calculation of the growth rates of the acoustic energy signals. The case for d=17 mm and β=1.6 is considered to explain how the growth rate has been calculated, please see figure 5.65.
Once concluded the simulation, fig.5.65.a, the first step to follow is to do the logarithm of the signal, fig. 5.65.b. This will highlight a linear trend, corresponding to exponential growth or decay of the acoustic energy. The initial part of the monitor is not taken into account, because it shows the filtering of the disturbance by the system. After this, the first linear portion of the signal is cropped, and separately analyzed. The next step is illustrated in fig. 5.65.c, where the upper and lower envelope

of the cropped signal are defined. The points of the envelopes are both interpolated with a first-degree polynomial, from which we obtain the lines' slope. The two coefficients of the two polynomials, representing their slope, are respectively averaged, and consequently, the growth rate of the signal is extracted. Finally, in 5.65.d it is plotted the exponential function that represents the exponential progression of the acoustic energy. An analogous approach can be applied to the decaying cases.

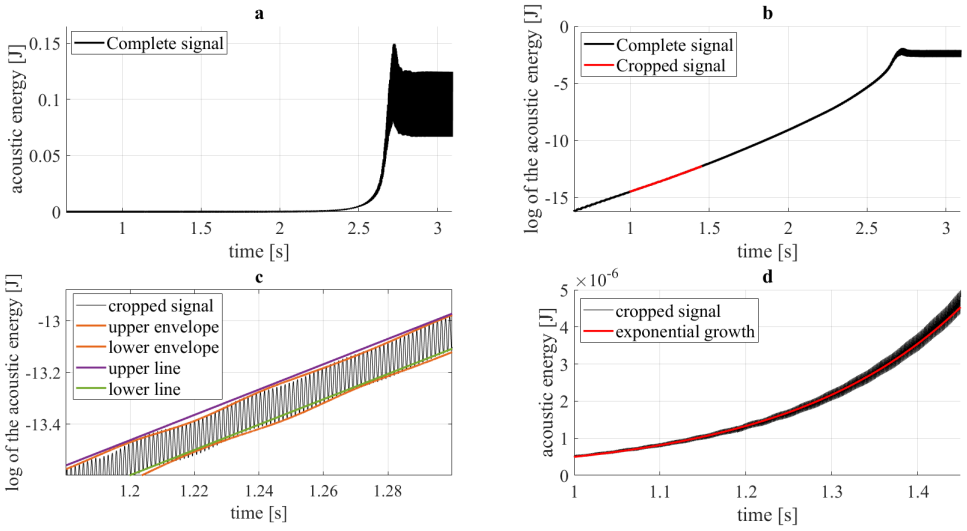

Figure 5.65: Determination of the growth rate of a specific acoustic energy signal.

In figure 5.66 are reported the growth rates of the monitored acoustic energy for the various numerical tests. The reader can see that, given a specific space delay, increasing the value of the parameter β leads to a progressive gain in the growth rate. As we have investigated, between β equal to 1.5 and 1.6 all three cases transit from a decaying condition to an unstable one, it is legitimate to think that this is also valid for other space lags that lay between 5 and 20 millimeters. In addition, the bigger the space delay the greater the consecutive growth rate.

If we now want to compare these results with the growth rates calculated in section 4.2.4 thanks to the linear theory, we first have to keep in mind that we are dealing with an energy that is proportional to the square of velocity and pressure, so this is why here the growth rates are divide by two.

In addition, by doing a Fast Fourier Transform (FFT) of the developing signal, we see that they grow with a main frequency very close to 400 Hz, similar to the one characterizing the limit cycle condition.

What it is possible to conclude is that these growth rates result to be much smaller than the ones calculated with the linear theory, please see figures 4.7, 4.8. Moreover close to 400 Hz, for both β equal to 1.7 and 2, decaying eigenmode are found. This highlights a strong discrepancy with the linear solutions, although the comparison is done between results obtained with a time lag and not a space lag.

The main reason for this discrepancy could be explained by focalizing on the mean flow analyzed on Ansys Fluent. Unlike the mean flow of section 4.2, where we already found a strong sensibility to the mean field, here we deal with a fluid that is

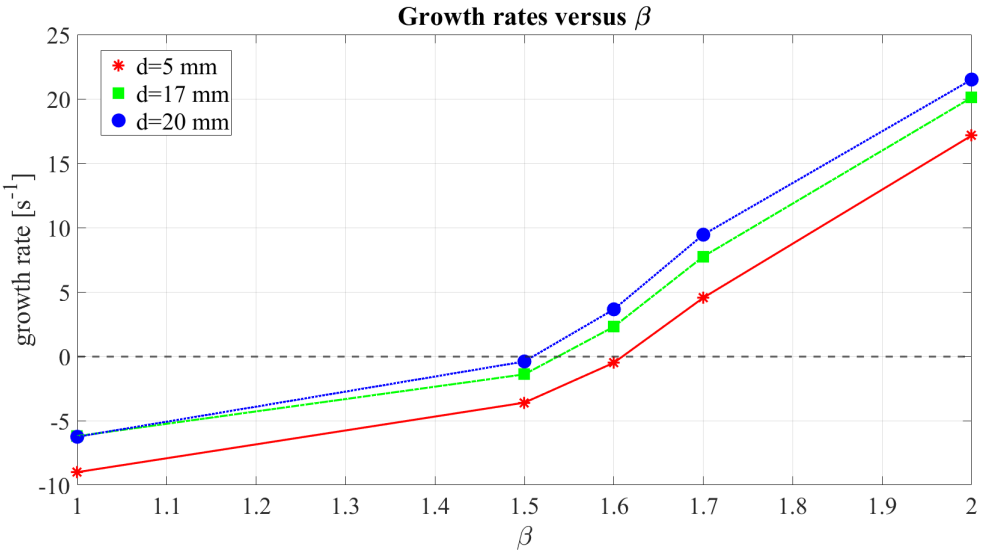

Figure 5.66: Growth rates of acoustic energy divided by two.

treated as viscous, that has turbulence, and also presents flow separation. Viscosity, for example, tend to extend the temporal scales.

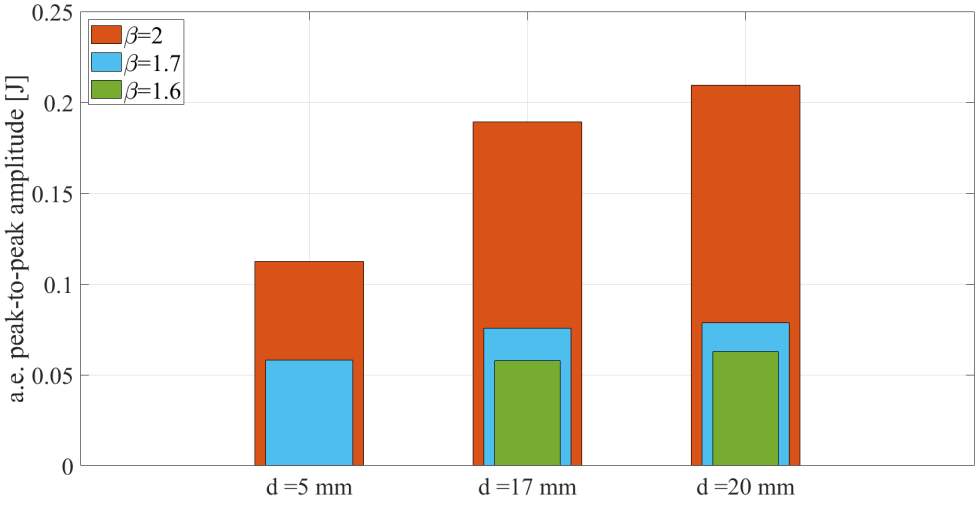

Figure 5.67: A.e. peak-to-peak amplitude (LC) vs distance from the flame.

Next, the focus goes on the limit cycle condition. The results obtained from the previous simulations are now reorganised and summarized in figure 5.67, where the the limit cycle's amplitude of the acoustic energy is plotted as a function of the space lag d, with β set as parameter. It is clear to see that switching to a bigger space lag, which means that the flow variables are sampled further from the flame, grants a growth in the limit cycle amplitude. In addition, as one would expect, increasing the value of the constant β correspond to larger limit cycle amplitudes.
Finally, a Fast Fourier Transform of each limit cycle signal has been done to highlight

the frequencies that characterize the oscillations. In figure 5.68, on the y-axis is plotted the power spectral density of the signal (PSD), which is a measure of the signal's power content, and on the x-axis are plotted the frequencies of the signal. The reader can see that all the limit cycles are almost characterized by the same frequencies, independently of the space lag or the value of β. The main frequency is around 385 Hz, moreover the first and third harmonics are visible.

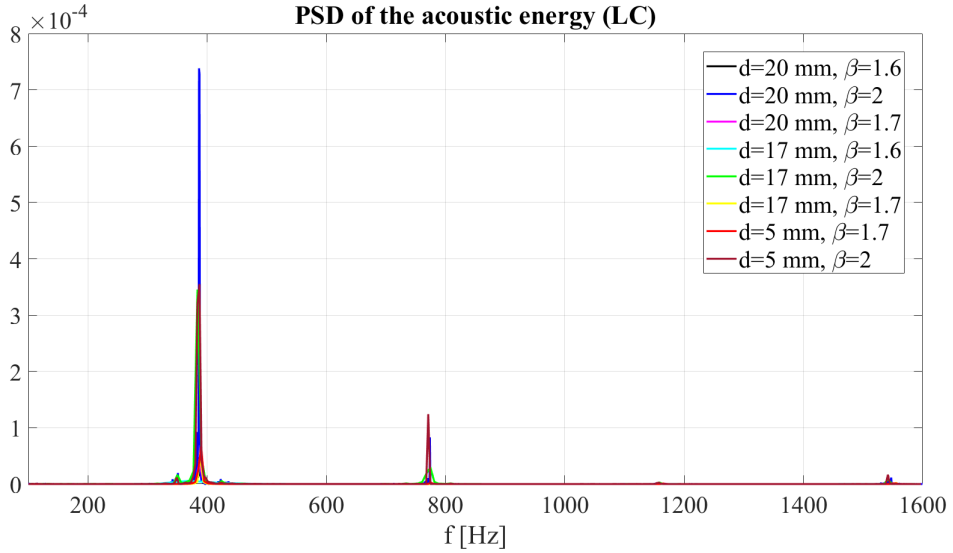

Figure 5.68: Power spectral density of the limit cycle signals of acoustic energy.

5.10 Bifurcations diagrams

In this paragraph we present the bifurcation diagrams computed for all the three cases. The investigation aims to find the type of bifurcation, whether supercritical or subcritical. For further definitions, please check section 3.5.2.
When reached a limit cycle state, the square root of acoustic energy is used to make a comparison between the different peak-to-peak amplitudes. The same approach adopted in section 5.4.3 has been used to calculate the limit cycle amplitude. In figures 5.69, 5.70, and 5.71, are presented the bifurcation diagrams defined for each space lag, with the square root of the peak-to-peak amplitude of the acoustic energy limit cycle on the vertical axis. The sample points are interpolated with a Piecewise Cubic Hermite Interpolating Polynomial (PCHIP).
In order to define this type of diagram, we have repeated the simulations starting from the limit cycle condition of the previous case. Firstly, we have done this by raising the value of β (forwards), and then by reducing it starting back from the β=2 condition. We chose β as a control parameter, which represents the amount of unsteady heat release rate, summed to the mean contribution, provided by the flame. In all the three cases, the reader can distinguish a subcritical bifurcation diagram. For d = 5 mm the bistable region extends from β=1.3-1.9, the backwards calculations show a clear hysteresis, with smaller limit cycle amplitudes. Moreover, switching from β=1.6 to 1.7, drives the system from a zero amplitude condition to a limit cycle state. Similar conclusions can be drawn for the two other space lags, d=17 mm and

d=20 mm. Here, the bistable region extends from β=1.9-1.2.

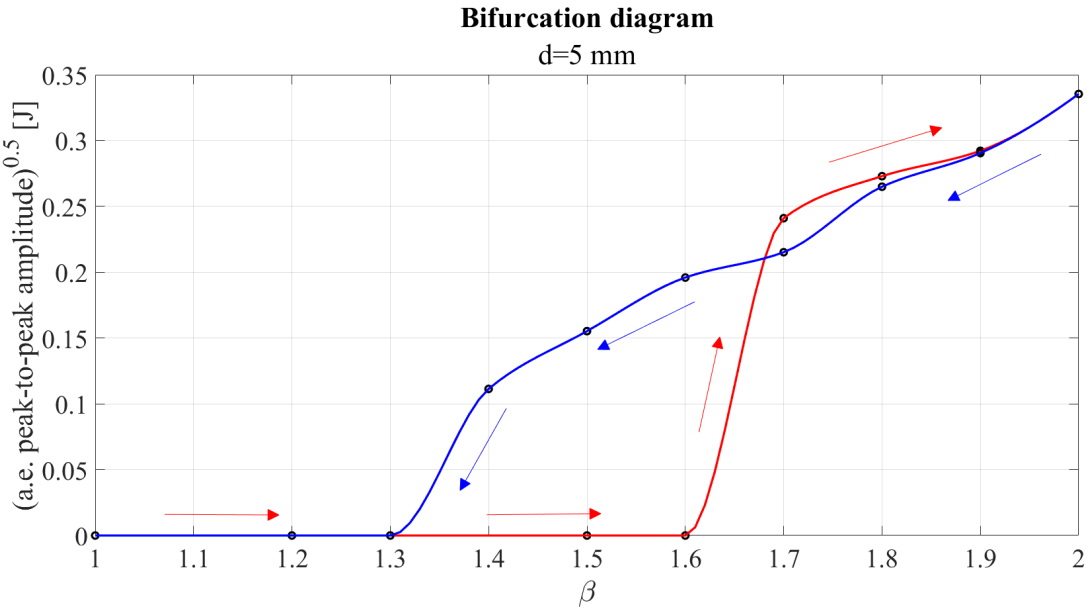

Figure 5.69: Bifurcation diagram, d=5 mm.

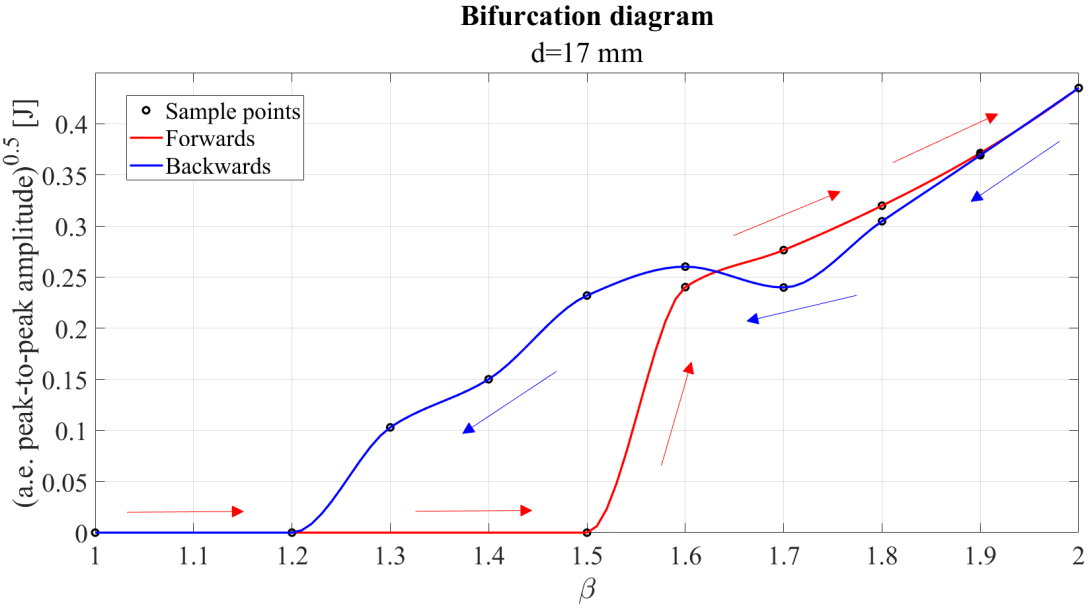

Figure 5.70: Bifurcation diagram, d=17 mm.

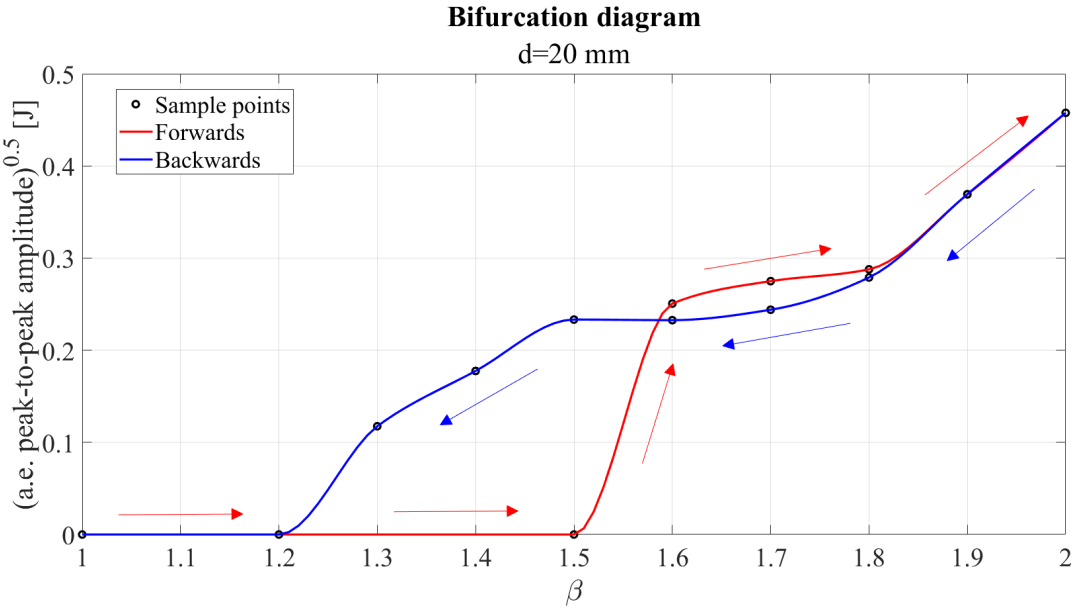

Figure 5.71: Bifurcation diagram, d=20 mm.

6 How to reduce thermoacoustic instabilities?

To control or even eliminate thermoacoustic instabilities, the coupling between acoustic waves and unsteady heat release should be broken.
The combustion instabilities can be controlled through two main techniques, using the *passive control* or the *active control*.
The passive control techniques tend to modify the combustor design changing the relationship between the acoustic waves and the unstable heat release rate; this coupling has to be interrupted by two different ways: the flame puts less acoustic energy in the acoustic mode of the combustor prone to instability, reducing the susceptibility of the combustion process to the acoustic excitation, or the combustor damping is increased removing the acoustic wave energy.
Reducing the susceptibility of the combustion process may include changes in the fuel injection system and in the combustor geometry, whereas the removal of energy of the acoustic wave may be achieved by devices and acoustic cavities; two common damping geometries employed in gas turbines are Helmholtz resonator and quarter-wave resonator. Usually these devices must be tuned to the frequency of the thermoacoustic instabilities to achieve significant mitigation and they must be designed at the locations where the pressure is maxima to adsorb a lot of energy [29, 30].
In recent years, hybrid methods such as adaptive-passive devices have been proposed to overcome this drawback, for examples:

- a tunable and variable volume Helmholtz resonator with a robust control algorithm [31];
- perforated combustor liners [32];
- perforated skin of the liner combined with the volume of the backing forms smaller annular Helmholtz resonators;
- acoustic radiator that actively produces acoustic waves in response to the pressure pulsations [33];
- insertion of a porous disk in the combustor design or porous annular ring at the dump plane of the swirl-stabilized LPM combustor.

The last configuration of a porous insert is effective in mitigating combustion noise and thermoacoustic instability, without negatively affecting NOx and CO emissions. Porous insert can absorb a fraction (about 30%) of the acoustic energy. Thus, the thermoacoustic instability is mitigated thanks to the presence of the porous insert which decreases the driving force of instability and increases the acoustic damping of the system.
One of the main problem about this technique is that the passive control techniques tend to be efficient only over a limited range of operating conditions and they are ineffective at low frequencies because oscillations are very difficult to be damped.

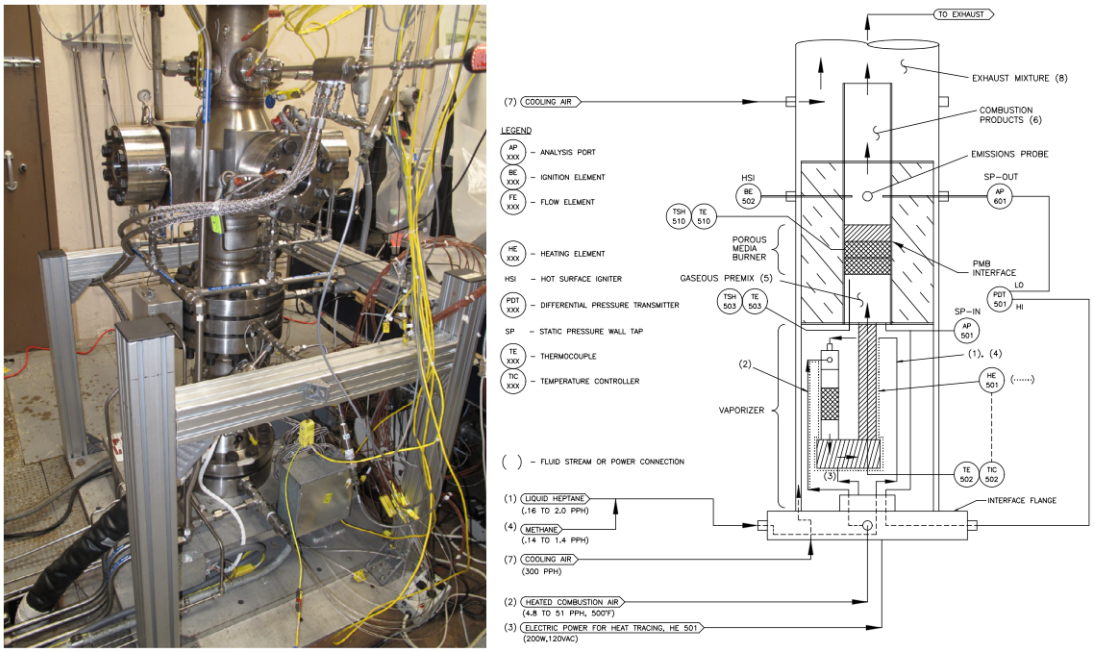

Figure 6.1: Example of experimental test of lean premixed pre-vaporized liquid-fuel combustion in porous media burners: image of experimental facility and schematic of porous media burner PMB test hardware [34].

The active control typically alters the equivalence ratio or reactant flow rates to avoid the phase relationship between heat release rate and pressure fluctuations and thus, avoid combustion instabilities.
Active controls have great potential to stabilize combustors even at off-design conditions, they are very 'adaptive'. They could be classified into open- or closed-loop configurations, which involve a feedback control configuration.
A dynamic actuator is applied to modulate some system parameters, which is responding to a sensor's measurement. Typical sensors include microphones, pressure transducers, or photomultipliers. These sensors capture the combustor's condition in real-time. This information is then supplied to a designed controller, that determines an actuation signal, which is used to drive the dynamic actuator. The actuator 'perturbs' the state of the combustion system in a manner which prevents the onset or mitigates the combustion instability [35].
Two main active control designs can be developed: modal based control and non modal based control.
The first one requires detailed knowledge of the system; this model is designed with the actuators and the sensors. The active control based on this model can provide strong guarantees that the system will not become unstable. It can be optimized for one or more operating points.
The second one can be universally applied but there is no guarantee that the model will work. The system is considered a black box and its behavior has to be learnt both as offline and online identification.
The best active control technique could be multiple modes.
The sensors, as microphones and piezo-electric transducers, can be used to measure acoustics quantities at some distances; we need to capture fluctuations that it is not

easy with other sensors, like thermocouples.
Some examples of actuators are:

- the loud speakers, that can be used to product *antisound*, but they have the disadvantages of they require a lot of power, they do not work correctly in a very hot and dirty environment;
- the fuel injectors, that can be produced fluctuating heat release rate.

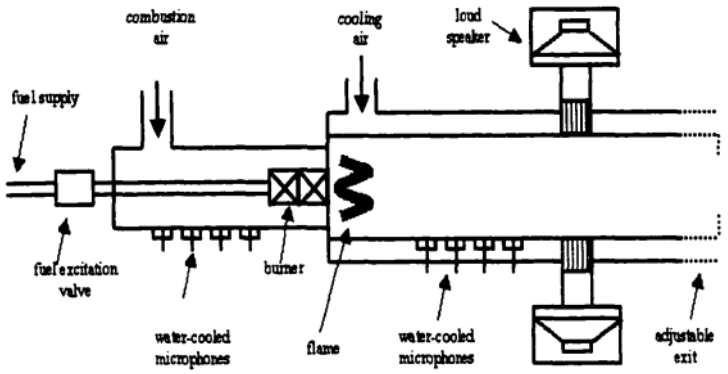

Figure 6.2: Combustor Test Setup: example of loud speakers and other devices for active control.

7 Implementation of a porous medium

7.1 Brief recap on porous media

Porous media are solid and heterogeneous materials having voids, called pores, in their microstructure and they can be passed through by fluids in motion.

Figure 7.1: High porosity ceramic material.

Porosity is one of the most important parameters of this type of materials, and it's defined as follow:

$$\epsilon = \frac{V_p}{V_{tot}} \tag{7.1}$$

It's a fraction of the volume of void spaces V_p over the total volume V_{tot}, so its value is between 0 and 1.
The permeability of a porous medium is another relevant quantity, it's a function of the type of material, and also other parameters like stress, temperature, ... etc.
According to Darcy's law, reported below, the effective fluid permeability k and fluid pressure gradient determine the flow rate:

$$Q = \frac{k \cdot A \cdot \Delta P}{\mu \cdot L} \tag{7.2}$$

where Q is the volumetric flow rate $[m^3/s]$, k is the permeability $[m^2]$, A is the area $[m^2]$, ΔP is the pressure drop [Pa], μ is the dynamic viscosity of the fluid $[Pa \cdot s]$ and L is a given distance [m].
The permeability is governed by the size and distribution of pores along with the

defects present in the material's microstrucdesigns
Reducing the porosity and pore size decreases permeability, thereby increasing the mechanical strength of the porous media, like ceramic ones.
To better understand this property, the following formula reports the Kozeny–Carman equation, which correlates the permeability with the size and distribution of pores:

$$k = {\Phi_s}^2 \cdot \frac{\epsilon^3 \cdot {D_p}^2}{150 \cdot (1-\epsilon)^2} \tag{7.3}$$

where Φ_s is the sphericity of the particles and D_p is the average particle diameter [m].

7.2 Applications of porous media in combustion technology

Porous media are used in combustion technology and typically in order to better control flame stabilization and other aspects. Typically two different porous disks are located before and after the flame.
The two zones are respectively called *combustion zone* and *preheating zone*. The first zone is made up of a material with larger pore sizes, high radiation and combustion characteristics; while the second one is made up of a material with low conduction capabilities and smaller pore size.

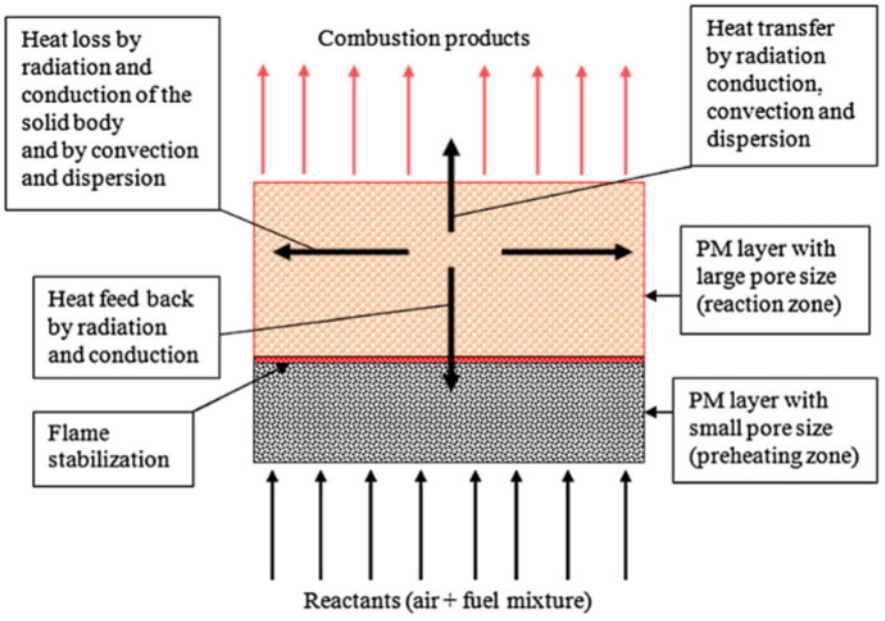

Figure 7.2: Schematic of a porous burner.

The disk located in the combustion zone has to support heat recirculation through the porous media.
The disk placed in the preheating zone is made up of a porous material characterized by a low thermal conductivity and small pore size in order to avoid the phenomenon of flashback.
The choice of the material that will used in the preheating zone is fundamental for the

overall combustion performance and pollutant formation, because these aspects are governed by the length of the pores and the burner's heat recirculation capabilities. The phenomenon of heat recirculation is one of the most crucial factors that gives porous burners interesting characteristics over the free flame burners, indeed a porous burner uses both radiation and conduction to support the enhanced heat transfer, in addition convection is improved because of the higher surface area. However this aspect needs to be controlled, because an increase in heat exchange produces an increase in the flame speed. Furthermore, the preheating zone allows the mixture to reach a temperature that can sustain chemical reactions [36].
It is necessary to control two different parameter: the porosity ϵ and the particle diameter D_p. Higher porosities mean larger pores, but less number of pores to allow flame propagation, whereas lower porosities provide higher rates of energy transfer through the solid.
So it's important to study the correct equilibrium between this two quantities in order to optimize the porous material properties and to control flame stabilization and radiation efficiency together [37, 38].
Combustion in porous media has been identified as a promising technology for achieving higher burning rates, extending flammability limits and reducing emissions.
The characteristics of combustion within porous media are:

- excellent stability behaviour;
- ability to burn leaner and hotter than a free flame;
- lower NO_x emissions associated with the low gas temperatures at lean conditions;
- extension of the flammability limit at leaner conditions;
- faster flame speeds;
- possibility to operate free from combustion-induced noise;
- no cooling requirement for the combustor itself;
- PMB's design can ensure the anchor of the flame.

This properties testify a wide variety of possible applications of porous media, for example in internal combustion engines, gas turbines and propulsion, heat exchangers, hydrogen production, liquid fuel combustion and many others.

7.3 Ceramic materials for porous media

The selection of the correct porous material is central, among the high-performance materials stand out the ceramic ones.
In particular, for the porous ceramic media (PCM) the selection of the right material is one of the most significant burner design factors, due to the fact that thermophysical properties play a vital role to achieve desired performance characteristics [36].
Ceramic materials have a large surface-to-volume ratio and this favors direct heat exchange, moreover, the high porosities minimize the pressure drop.
Alumina, Silicon carbide, and Zirconia are generally the three main materials selected for their applicability in porous burner technology, thanks to their intrinsic characteristics such as high thermal shock resistance, high chemical stability, excellent creep resistance, higher melting points, high porosity, high durability, good radiative properties, easy availability, and lower costs.

7.3.1 Alumina

Alumina Al_2O_3 can be employed in environments with high operating temperatures, as high as 1900 °C. This peculiarity promotes its use in porous burner applications, in particular, an application in the preheating zone. On the other hand, it has moderate thermal shock resistance and low thermal conductivity characteristics.

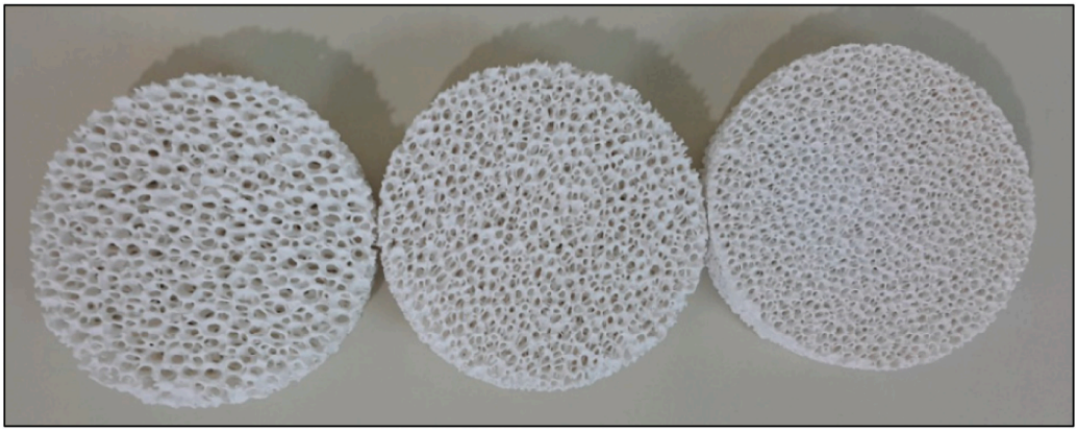

Figure 7.3: Al_2O_3 based PCFs (Porous Ceramic Foams).

7.3.2 Silicon carbide

Silicon carbide SiC has excellent heat transfer properties and good thermal shock characteristics, however, this material creates a silicon layer that reduces the corrosion resistance of the material under extreme operating conditions.
With that being said, as compared to Al_2O_3, it is the most used material thanks to its higher heat transfer coefficient, because it supports better rates of heat transfer through radiation and conduction.
Silicon carbide SiC can be employed in operating temperatures of 1750 °C.
These ceramic foams are used in numerous fields, such as energy, aerospace, metallurgy, machinery, environmental, chemistry, and medical fields, for many applica-

tions as filters, membranes, thermal insulators, or heat exchangers, sound-absorbing material, capacitors, damping buffers, sensors, catalysts and catalyst carriers, and many others.

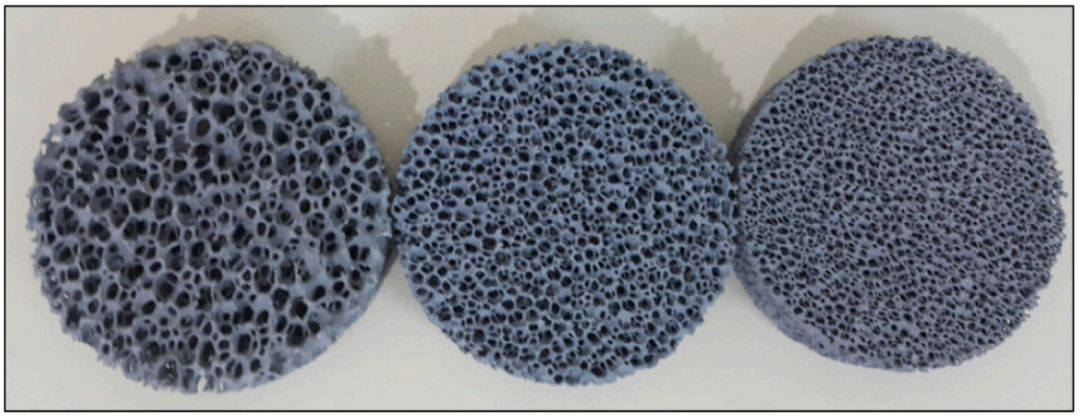

Figure 7.4: SiC lamellae.

7.3.3 Zirconia

Zirconia ZrO_2 can be employed in operating temperatures as high as 1800 °C, thanks to its high thermal conductivity.
One major limitation of using ZrO_2 as PCM in burner applications is the relatively high cost of the material. Finally, Zirconia exhibit relatively low thermal conductivities among ceramic materials.

7.4 Case for a porous medium located before the flame

The next section is based on a new case, characterized by the implementation of a porous medium located before the flame of the combustor model.
The purpose of this section is to investigate the behavior of the thermoacoustic instabilities, flow quantities, and other parameters.
It is expected that the porous medium will damp the thermoacoustic instabilities, on the other hand, one should take into account that this will cause an additional pressure loss due to the presence of this physics barrier in the flow.
Again, the numerical tests are conducted using the commercial software Ansys for computational fluid dynamics.
The workflow is similar to the nonlinear analysis conducted in section 5. Firstly, it is required to introduce in the control volume a new geometry, in order to define and locate the porous medium. Afterwards, a new mesh is properly adapted to the case. Subsequently, the code settings come, here, it is important to focus on the porous zone and how the software will model it. Finally, the numerical results are post-processed.

7.4.1 Geometry

The geometry of the model combustor is the same as the previous case, where no porous medium was implemented (figure 5.1).
The only difference is that now the geometry has a new section added in the premixer duct in order to model the porous zone.
Below, it is reported the zoomed geometry of the porous zone marked in orange.

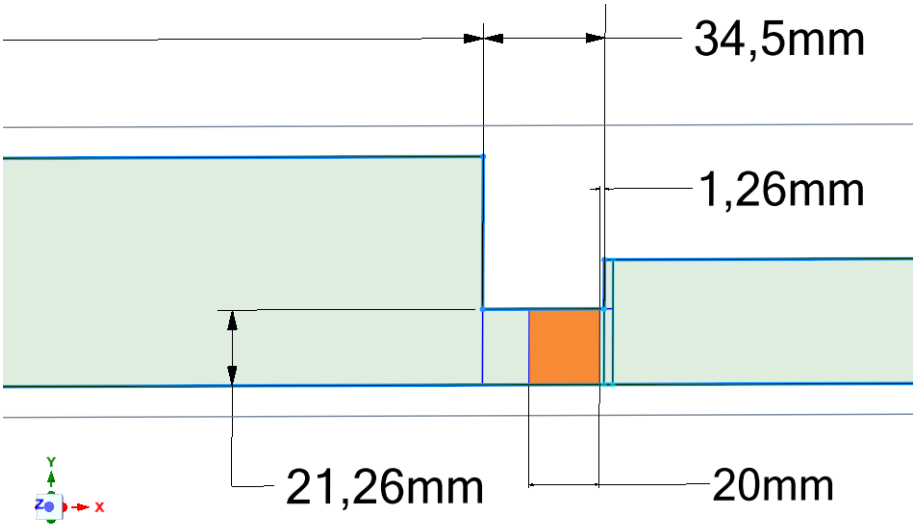

Figure 7.5: Geometry of the porous medium case localized before the flame.

The porous septum has the same radius as the premixer and has a thickness of 20 mm. These dimensions are related to a similar case found in literature that is taken as reference, where we impose the same ratio between the two respective dimensions, radius and thickness [39].

The porous medium is localized just before the flame's position, but the outlet section of the porous zone doesn't coincide with the flame's region inlet. There is a small gap of 1,26 mm between the porous zone and the flame.
This is related to the fact that it is better not to choose the same line to impose simultaneously two different conditions.

7.4.2 Mesh

The second step is the mesh. As in the previous case, an unstructured mesh with triangular elements has been designed. The number of cells is 127677, and the minimum orthogonal quality is equal to 0.45323.
In the following figure, it's reported a zoom on the premixer duct (section 2), where the porous zone is highlighted in yellow and the flame region is highlighted in red.

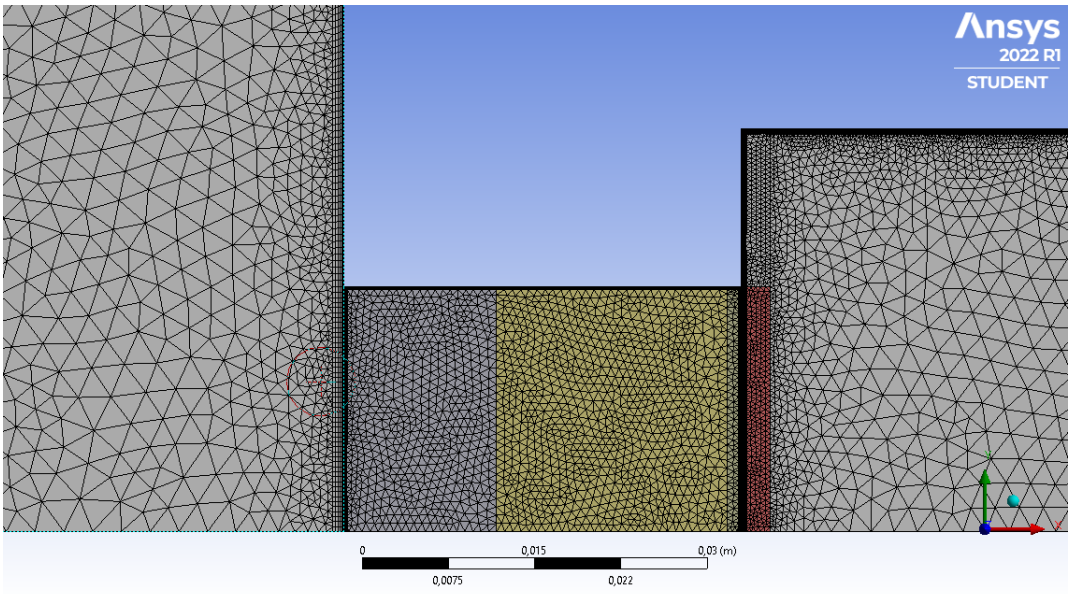

Figure 7.6: Mesh of the porous medium localized before the flame.

7.4.3 Setup of the simulation

The flame energy source is controlled by imposing at first a constant heat source equal to 24218000000 $\frac{W}{m^3}$ and then implementing an unsteady heat addition model, which takes into account a fluctuating term.
The porous zone is set in Fluent under *cell zone conditions*; in particular, it is necessary to define some porous properties, which characterize the porous medium. These parameters are the viscous resistance, the inertial resistance, and the fluid porosity. As a first approximation, for the heat transfer option it is set an equilibrium condition, which means that the solid and fluid parts of the porous are at the same temperature. This hypothesis is reasonable thanks to the porous medium location, which is before the flame, and so the global influence of convective and conductivity heat, in terms of the total heat transfer rate, is negligible.

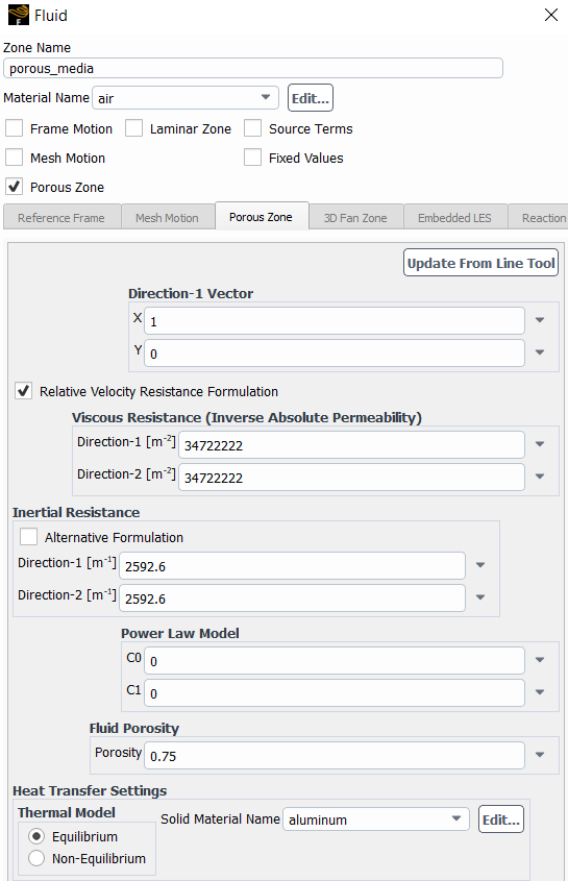

Figure 7.7: Cell zone condition for the porous medium case localized before the flame.

The permeability is evaluated using the equation 7.3 and the inertial loss coefficient in each component direction can be identified as follows:

$$C_2 = \frac{3.5 \cdot (1 - \epsilon)}{D_p \cdot \epsilon^3} \tag{7.4}$$

where Φ_s is the sphericity of the particle, D_p is the mean particle diameter and ϵ is the fluid porosity [40].
The particle sphericity is imposed equal to 1 by hypothesis, so the inclusions are considered spherics. Porosity is chosen equal to 0.75, this is due to the fact that in literature porosity usually has a value between 0.6 to 0.9. Consequently, we have decided 0.75 as a reasonable value, generally used in applications like this one.
In Fluent, it is necessary to set the viscous resistance, which is the inverse of the permeability $1/\alpha$, and the inertial resistance, which is the coefficient C_2; those values are respectively $34722222\,m^{-2}$ and $2592.6\,m^{-1}$.
This case of study is developed using a flame energy source term and the followed steps are similar to the previous case without the porous medium: a steady case and an unsteady case for a constant heat source, followed by the implementation of the same unsteady heat addition model.
The aim of this is to evaluate and compare the results with the previous ones.

7.4.4 The steady case for a constant heat source

The first step is to run a RANS simulation, initialized at the inlet, with a constant value of 24218000000 $\frac{W}{m^3}$ as the source term of the energy equation for the flame zone. After about 1000 iterations, convergence is reached.
In table 7.1 are presented the results for the area-weighted average of some flow properties, like temperature, density, pressure, and axial velocity profiles. They are sampled in correspondence of the four reference lines located at 1.5, 1.72 (this one is now inside the porous medium), 2, and 2.5 meters.

Area weighted average [m]	**Axial velocity [m/s]**	$p[Pa]$	$\rho\ [\frac{kg}{m^3}]$	$T[K]$
1.5	2.574	129305	1.502	299.996
1.72	24.981	121044	1.407	299.682
2	73.814	100974	0.180	1962.759
2.5	73.669	101046	0.176	2000.721

Table 7.1: RANS results for a constant heat source.

The net total heat transfer rate provided by the model combustor is **-85974 W**, this value is negative because the heat flux is globally outgoing from the control volume.
In the next three figures are presented some contours resulting from the current numerical test, the reader can observe the static temperature distribution, the static pressure distribution, and a zoom localized on the porous medium of the static pressure distribution.
The static temperature contour is similar to the previous one, where the maximum and minimum values are the same.

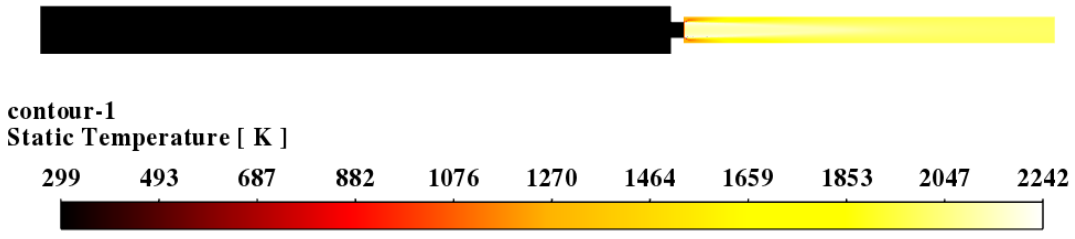

Figure 7.8: RANS simulation, static temperature distribution.

There is a pressure drop before and after the porous medium which is plotted along the porous medium axis (fig 7.11). At the inlet of the porous medium, the static pressure is equal to 27473.7 Pa, and at the outlet is 3461.9 Pa, so the pressure drop results in 24011.8 Pa.

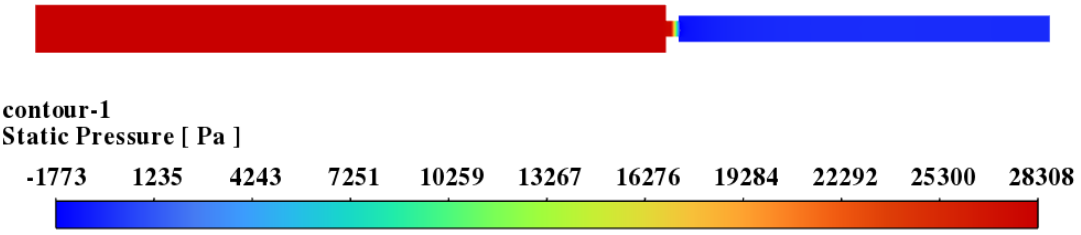

Figure 7.9: RANS simulation, static pressure distribution.

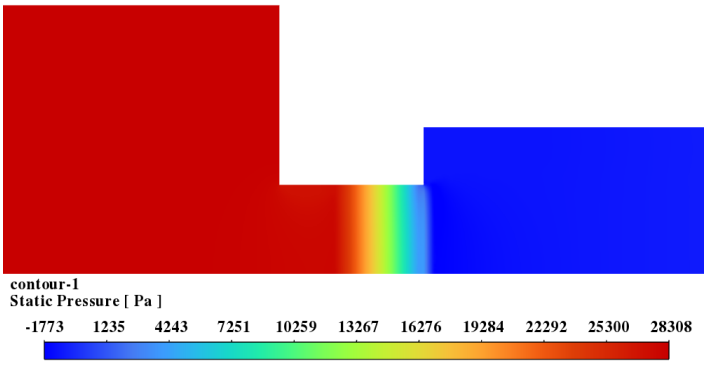

Figure 7.10: RANS simulation, zoom static pressure distribution.

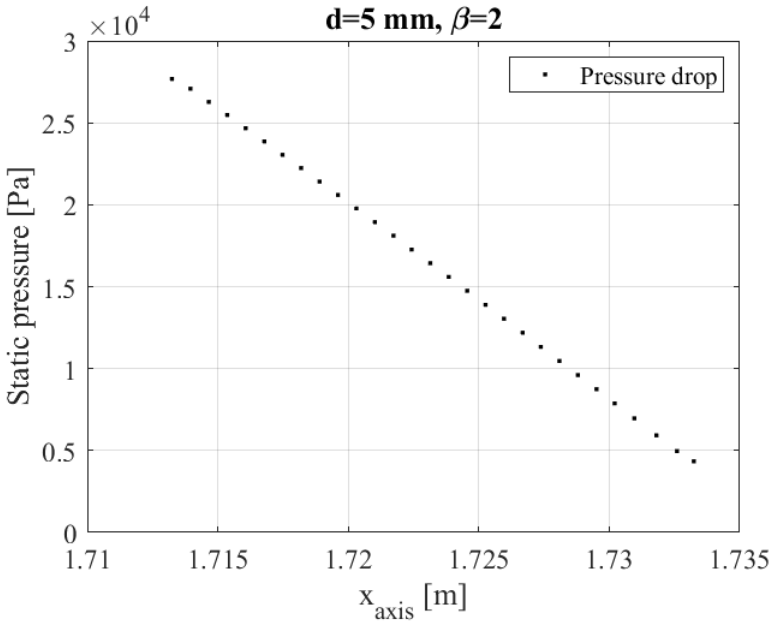

Figure 7.11: Pressure drop along the porous medium x-axis.

7.4.5 The unsteady case for a constant heat source

The unsteady case for a constant heat source is running in order to have a better starting condition for the URANS simulations.
The constant heat source doesn't change for the flame energy equation. Some modifications are implemented, for example, the simulation becomes transient and the fractional step method is used; it is also necessary to set a time step, which allows to control the CFL number and to keep it under 1.
The following figures, 7.12 and 7.13, report two contours, one for the turbulent intensity and one for the axial velocity distribution.

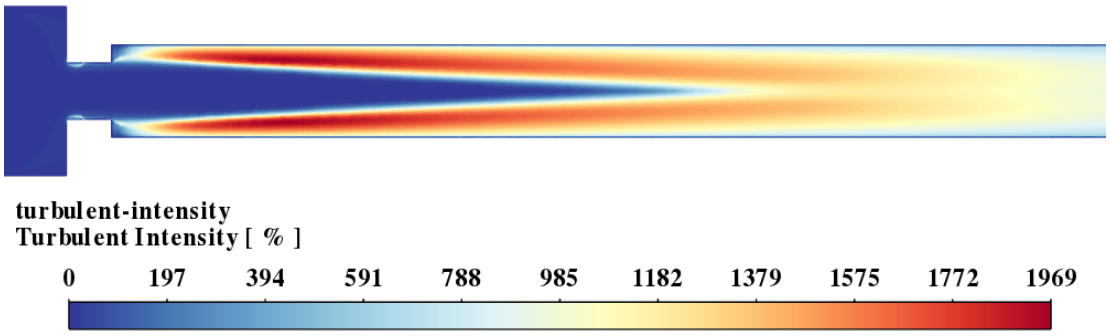

Figure 7.12: URANS simulation, turbulent intensity [-].

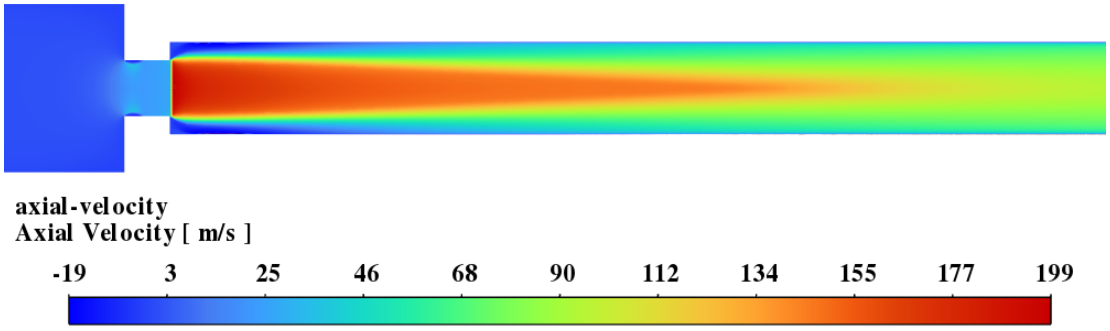

Figure 7.13: URANS simulation, axial velocity distribution [m/s].

It is interesting to see the formation of two distinct separation bubbles, one in the second duct before the porous medium, and one at the beginning of the combustor chamber, this is due to a local reduction of turbulent intensity and axial velocity. Indeed, the wall shear stress goes to zero in these locations and it can also be seen that velocity vectors reverse their directions; these features confirm the presence of separation bubbles.

7.4.6 Unsteady heat addition

The following step is to investigate the unstable behavior of the combustor model, so it is implemented an unsteady heat addition model described by the equation 5.2.

The aim of this subsection is to test the porous medium in order to control if it works properly. The main purpose is to damp thermoacoustic instabilities, and, as a result, limit the value of β for which we expect to trigger instability.
The following table presents the main results of these simulations. As the parameter d increases, which means that the spatial delay before the flame grows, there is a decrement in the area-weighted average of axial velocity obtained from the corresponding RANS simulation, used to calculate the axial velocity fluctuations. This is a direct consequence of the pressure drop imposed by the porous septum. None the less, there is an increment of the limit value of β, namely the value of the constant above which the system becomes unstable.
The limit value of β grows with the spatial delay d because the porous medium significantly affects velocity fluctuations, which are smaller further from the flame where pressure is higher. Consequently, the value of β for which the system becomes unstable needs to be greater, in equation 5.2 the fluctuating term depends on two main contributions: the constant β and the axial velocity.
We also have to keep in mind that thermoacoustic instabilities occur if the acoustic driving is greater than the damping effect (Rayleigh criterion).
Thanks to this investigation of the limit values of β, we have obtained a range of values that contains β_{lim} and those ranges are reported in the table 7.2, together with the area-weighted averages of axial velocity from the RANS simulations, sampled at the corresponding distance d.

$d\,[mm]$	**Axial velocity [m/s]**	$\beta_{inf} < \beta_{lim} < \beta_{sup}$
5	27.6367	15 - 20
17	24.4010	25 - 30
20	23.7176	25 - 30

Table 7.2: URANS results with flame model implementation.

Figures 7.14 and 7.15 show mass flow rate and total heat transfer rate signals as representative examples of the decaying behavior for $\beta = 2$. The reader will remember that for this value of β the original case without porous medium becomes unstable. So, for this case the porous medium works fine.

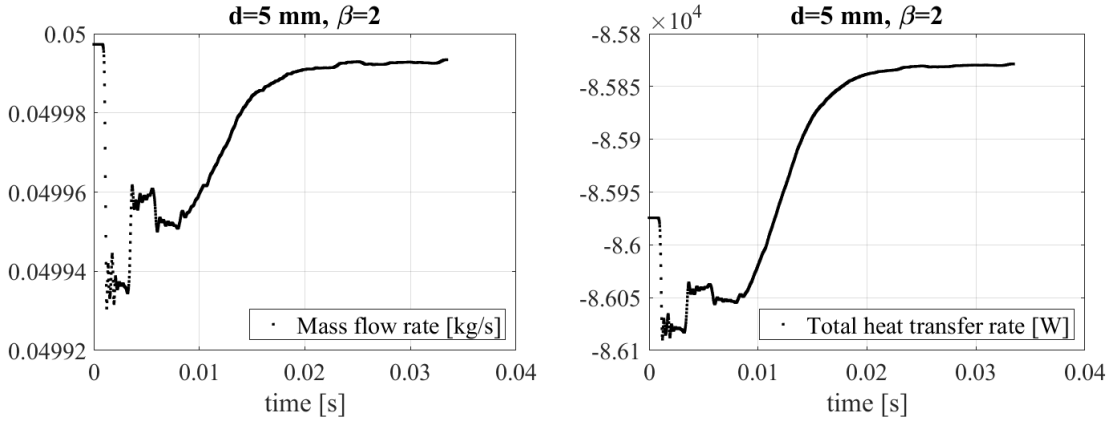

Figure 7.14: Mass flow rate and total heat transfer rate signals for d=5 mm and $\beta = 2$.

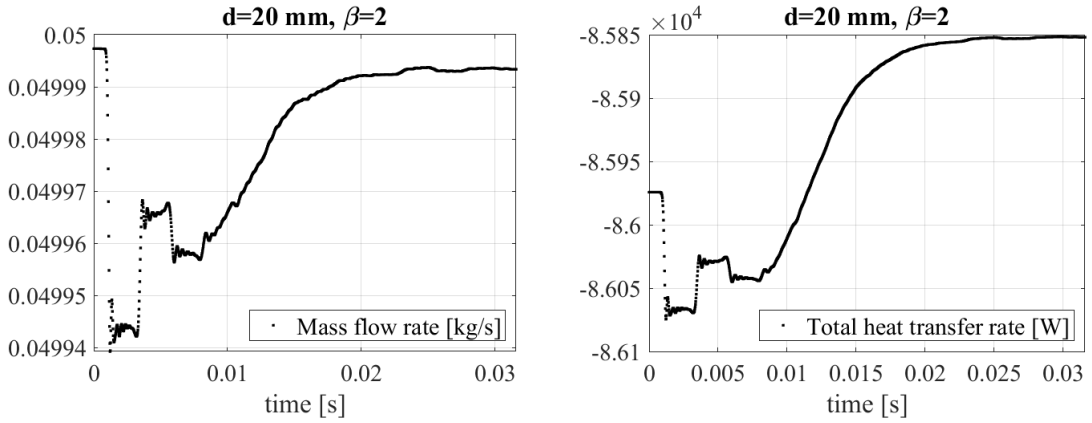

Figure 7.15: Mass flow rate and total heat transfer rate signals for d=20 mm and $\beta = 2$.

In the next figure 7.16, are shown the acoustic energy signals for $d = 5mm$ and $d = 20mm$.
These plots are characterized by an exponential growth, which means that an unstable condition is triggered, unfortunately the code is unable to converge and so the limit cycle condition isn't achieved.

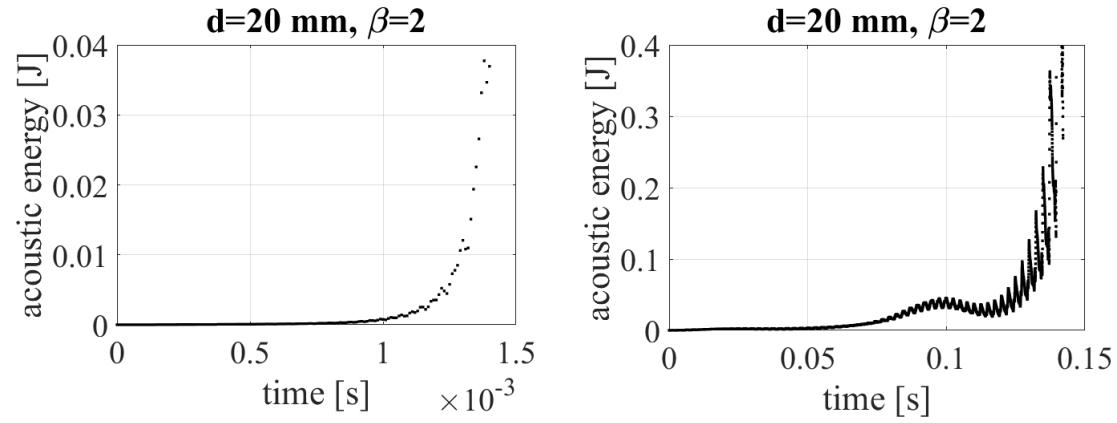

Figure 7.16: Acoustic energy signals for d=5mm, $\beta = 20$ and d=20 mm, $\beta = 30$.

The next table shows the results from the unsteady simulation varying the porosity in order to study its effect on the other flow quantities. In this parametric study, the spatial delay d is fixed equal to 20 mm. This choice is related to the fact that the 20 mm case has the biggest growth rates and limit cycle amplitudes among the other cases.
Increasing porosity translates into an increment of the void spaces, and as a consequence, the pressure drop between the porous medium decreases and, at the same time, the axial velocity increases. The value of β_{lim} decreases as porosity increases. This is related to the fact that, considering the fluctuating term in equation 5.2, the axial velocity fluctuating contribution becomes bigger, thus a smaller value of β_{lim} is sufficient to trigger instability.

Porosity [-]	Permeability [m^2]	Inertial coefficient [m^{-1}]	Axial velocity [m/s]	ΔP [Pa]	$\beta_{inf} < \beta_{lim} < \beta_{sup}$
0.75	$2.88 \cdot 10^{-08}$	2592.6	23.7176	24 012	25-30
0.85	$1.16 \cdot 10^{-07}$	1068.6	26.4118	10 505	15-20
0.9	$3.11 \cdot 10^{-07}$	600.1	27.4552	5 991	5-10

Table 7.3: URANS results with flame model implementation and varying porosity.

7.5 Case for a porous medium located after the flame

This section presents the implementation of a porous septum inside the combustion chamber duct. It is located after the flame in three different positions in order to investigate the influence of the medium's location on thermoacoustic instabilities.

7.5.1 Geometry

The porous medium has different dimensions with respect to the previous case; in particular, it has the same radius as section 3 and a thickness of 33 mm.
Three case are now defined, with the porous septum localized in three different positions:

- configuration 1 - at 250 mm from the flame's position, figure 7.17;
- configuration 2 - at 500 mm from the flame's position, figure 7.18;
- configuration 3 - at 750 mm from the flame's position, figure 7.19.

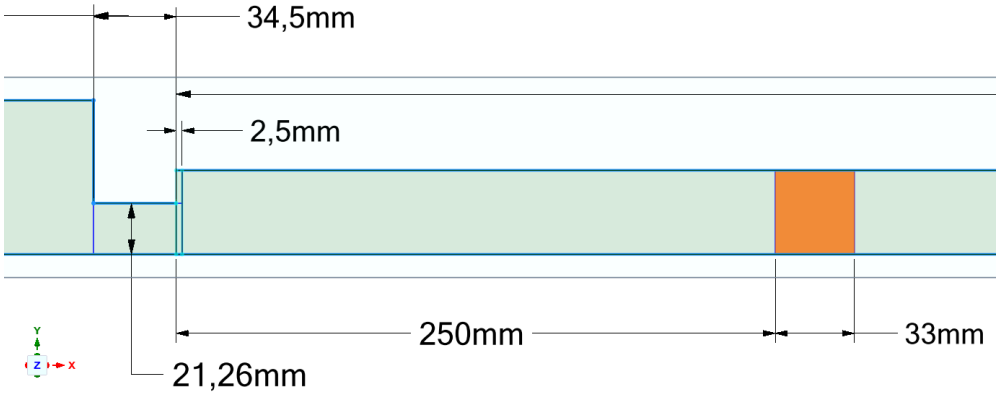

Figure 7.17: Geometry of the porous medium localized at 250 mm from the flame.

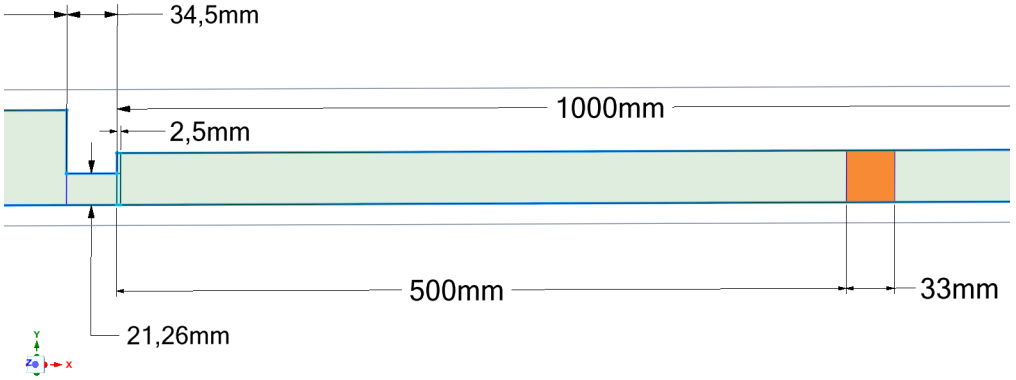

Figure 7.18: Geometry of the porous medium localized at 500 mm from the flame.

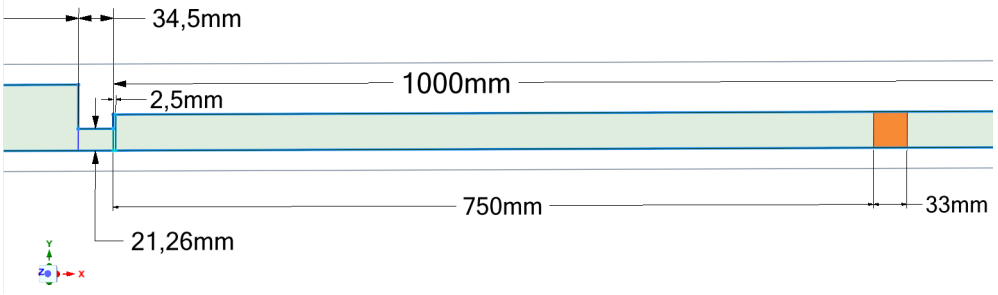

Figure 7.19: Geometry of the porous medium localized at 750 mm from the flame.

7.5.2 Mesh

Again, an unstructured mesh with triangular elements has been designed for these new porous medium configurations. The number of cells is 127860, and the minimum orthogonal quality is equal to 0.5053.
In figure 7.20 is presented a zoom of the porous medium mesh, which is finer than the other regions of the combustion chamber in order to better model and investigate this case.

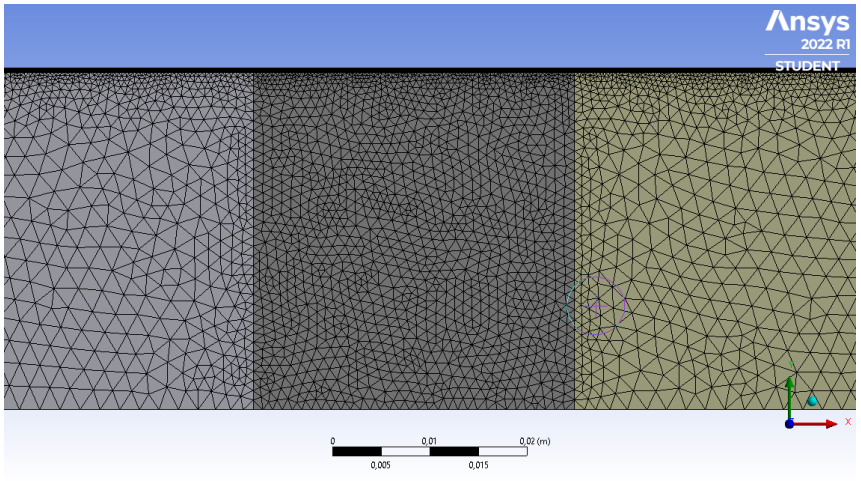

Figure 7.20: Mesh of the porous medium case localized after the flame.

7.5.3 Setup of the simulation

The general setup is the same as the previous porous medium case.
The only difference is about the porous cell zone condition. Viscous resistance, inertial resistance, and fluid porosity are equal to the previous chosen values, what has been modified are the heat transfer settings.
There are two thermal models for a porous zone: the equilibrium model, the one used for the previous case, which assumes thermal balance, that is fluid and solid environments have the same temperature during the simulation. The other option is to choose the non-equilibrium model, which assumes thermal imbalance, so the solid part can have a different temperature or heat flux compared to the fluid zone [40].
For this case, the non-equilibrium model is chosen in order to better predict and model heat transfer in the porous medium during a possible instability . Indeed, the septum is localized after the flame, thus one cannot overlook that the temperature levels in the combustion chamber are higher, so this implies that it cannot be assumed a constant temperature between the fluid and the solid parts.
As a consequence, for the next simulations, where the porous medium and the fluid flow are not assumed to be in thermal equilibrium, a dual cell approach is used. In such approach, a solid zone that is spatially coincident with the porous fluid zone is defined, and this solid zone only interacts with the fluid by means of heat transfer.
Silicon carbide is the selected material for the solid porous zone and its properties are presented below, please see figure 7.21.

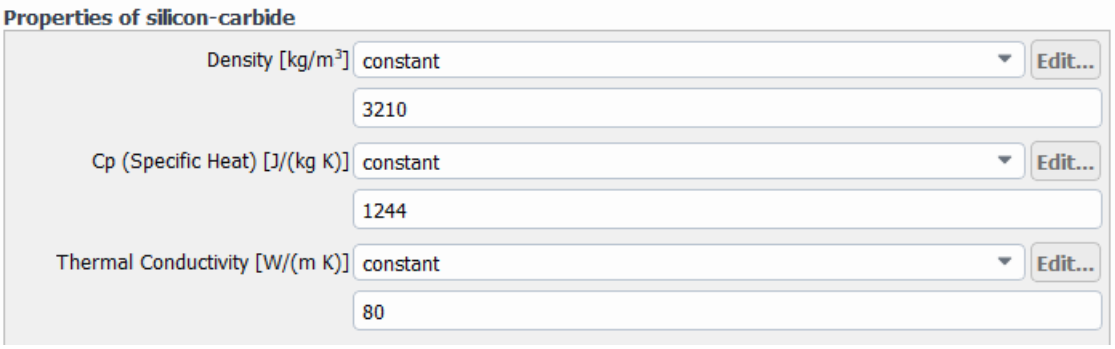

Figure 7.21: Thermophysical properties of silicon carbide.

The conservation equations for energy are solved separately for the fluid and solid zones, and the source term due to the non-equilibrium thermal model is defined as:

$$\dot{Q}_{source} = h_{fs} \cdot A_{fs} \cdot (T_f - T_s) \tag{7.5}$$

where T_f and T_s are respectively the temperature of the fluid and the temperature of the solid medium. Two other important parameters need to be implemented in the non-equilibrium thermal model, as the porous medium material has to be defined: the heat transfer coefficient for the fluid/solid interface h_{fs} and the interfacial area density A_{fs}, defined as the ratio of the area of the fluid-solid interface to the volume of the porous zone.

The interfacial area density A_{fs} is calculated thanks the following formula:

$$A_{fs} = \frac{6\,\epsilon}{D_p} \tag{7.6}$$

where in this case it is equal to 5625.
The convective heat transfer h_{fs} in porous materials is still a formal and complex subject due to the intricate microstructure and the heterogeneity of the pores. The enhancement of heat transfer in porous media can be achieved by two major mechanisms. Firstly, ligaments orientated normally to the flow direction provide tortuous pathways to enhance the flow mixing and promoting vortices. Secondly, boundary layer disruption increases the fluid turbulence.
In order to evaluate h_{fs}, the porous medium is considered as a black box and, as a measure of the amount of energy transferred from the fluid to the solid matrix or vice versa, it is taken into account the Number of Transfer Units (NTU).
The NTU is evaluated from the experimental results presented in the paper [41] against the permeability based Reynolds number Re_k, which can be defined as:

$$Re_k = \frac{\rho_f \cdot V_f \cdot \sqrt{K}}{\mu_f \cdot \epsilon} \tag{7.7}$$

where ρ_f is the fluid density, V_f is the fluid velocity, K is the permeability, μ_f is the fluid dynamic viscosity and ϵ is the porosity.
In our work, all the flow quantities are evaluated thanks to an area-weighted average computed at a distance of 500 mm from the flame, for the case without porous medium. The value of Re_k results 47.5 thus, by taking into account figure 7.22, the NTU can be set equal to 5.

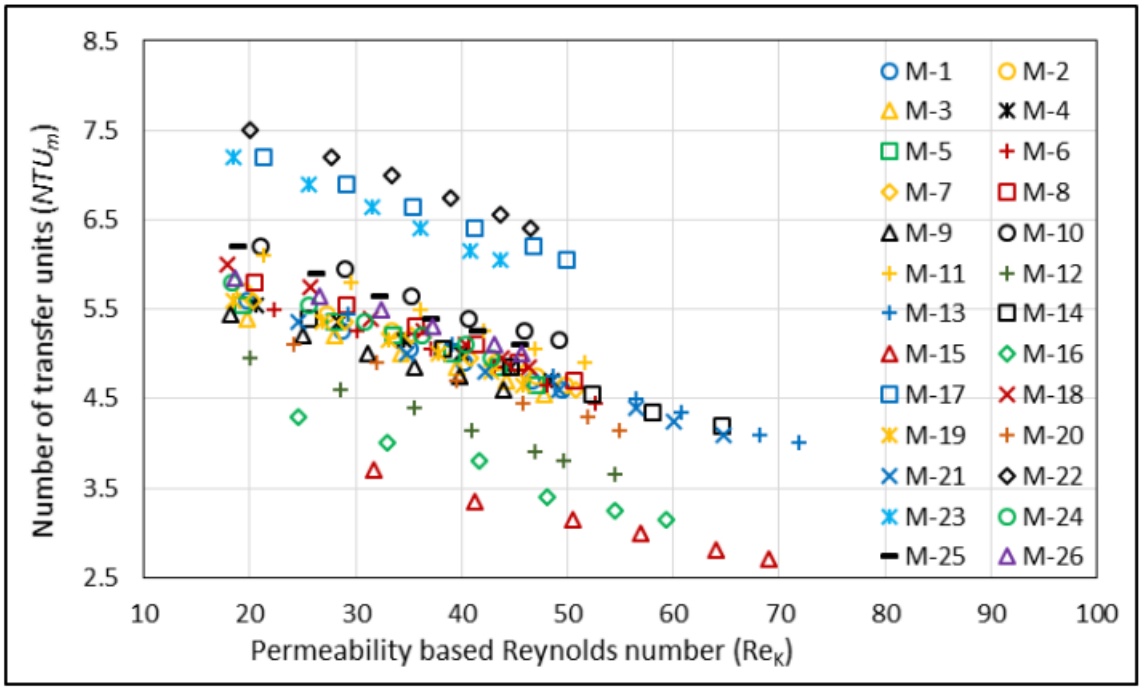

Figure 7.22: Heat transfer coefficient against permeability based Reynolds number.

The heat transfer coefficient can be expressed in terms of NTU, as follows:

$$h_{fs} = \frac{NTU \cdot \dot{m}_f \cdot C_f}{A_h} \tag{7.8}$$

where $\dot{m}_f$ is the fluid mass flow rate, C_f is the fluid specific heat and A_h is the heat transfer area (calculated multiplying A_{fs} by the fluid volume).
The heat transfer coefficient h_{fs} is calculated and then setted equal to 350 $W/(m^2\,K)$.
The final heat transfer settings are shown in the next figure 7.23.

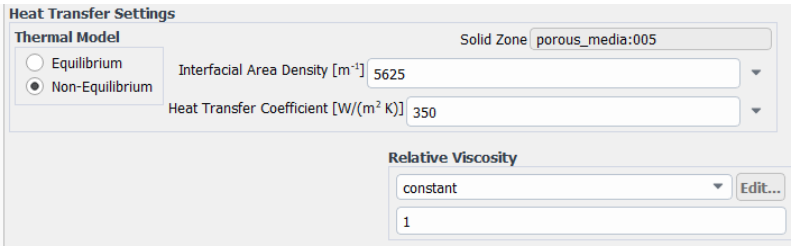

Figure 7.23: Cell zone condition for the porous medium case localized after the flame.

7.5.4 Unsteady heat addition

The steady and unsteady simulations for a constant heat source aren't presented for this case because the results are very close to the ones of subsections 7.4.4, 7.4.5. The unsteady heat addition model described by equation 5.2 is implemented to investigate the porous medium behavior after the flame. The constant β and the spatial delay d are respectively fixed equal to 2 and to 20 mm.
The results are presented varying the septum position in order to find the best configuration to reduce thermoacoustic instabilities. With reference to paragraph 7.5.1, configurations 1 and 2 reach a limit cycle condition, as it can be seen in figures 7.24 and 7.25. Instead, the last porous medium configuration has decayed, reaching a stable condition.

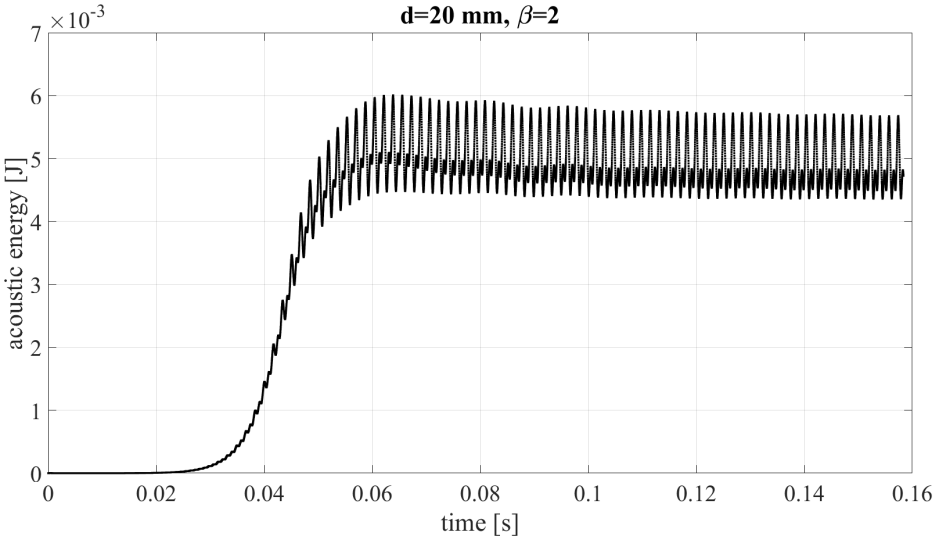

Figure 7.24: Acoustic energy signal for the porous medium at 250 mm from the flame.

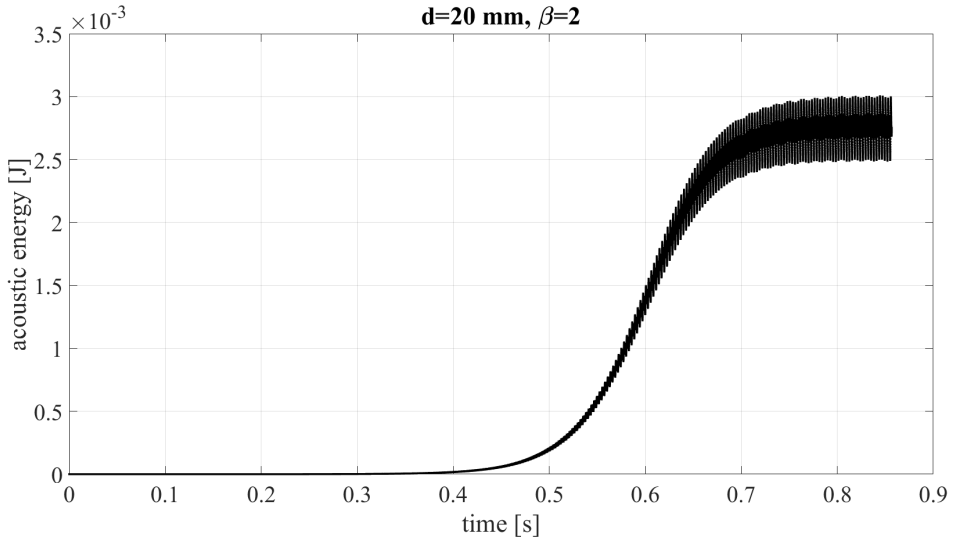

Figure 7.25: Acoustic energy signal for the porous medium at 500 mm from the flame.

From an acoustic point of view, the overall sound pressure levels measured in point 1 and 5 for the case of the porous medium at 250 mm from the flame have an average value of 145 dB and 116 dB, and for the other case the values are respectively equal to 138 dB and 116 dB.
The limit cycle amplitudes of acoustic energy signals are reported in the following table, where they are compared with the results of the previous case ($\beta = 2$ and $d = 20\,mm$), but without the porous septum. Although the first two setups develop a thermoacoustic instability, the limit cycle amplitude results to be two or three orders of magnitude smaller than the reference case. The third configuration is a decayed case, here, the system is stabilized thanks to the presence of the porous medium.

Case	**Limit cycle amplitude [*J*]**
Without porous medium	$2.1 \cdot 10^{-1}$
Configuration 1	$1.3 \cdot 10^{-3}$
Configuration 2	$4.8 \cdot 10^{-4}$
Configuration 3	0

Table 7.4: Limit cycle amplitudes of the acoustic energy with and without the porous medium.

In the following figure 7.26, are presented the flame temperature signals of the first two unstable cases compared with the case without porous medium.

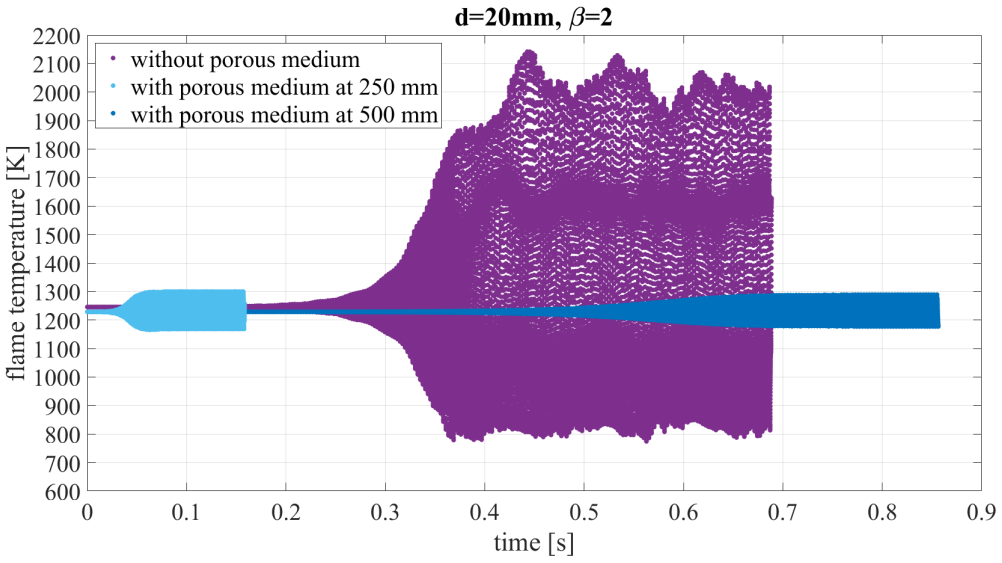

Figure 7.26: Unstable signals of the temperature volume-average of the flame zone [K].

Finally, in addition to the analysis of these two unstable cases, it is reported the power spectral density of the acoustic energy signal in figure 7.27, obtained by doing the FFT of the limit cycles to point out the frequencies of the signal.
The main frequencies are different from the previous case (385 Hz), please see figure 5.68. The main frequency for the case of the porous medium localized at 250 mm from the flame is about 580 Hz and for the other case is 350 Hz.
The y-axis values are lower than the ones plotted in figure 7.27; this means that the signal's power has been reduced thanks to the presence of the porous medium.

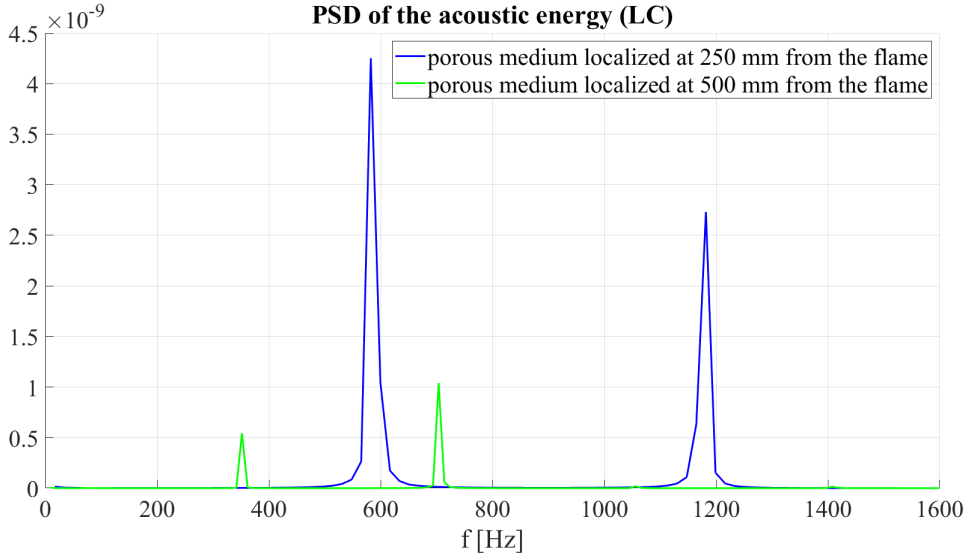

Figure 7.27: Power spectral density of the limit cycle signals of acoustic energy.

One can also notice that introducing a porous medium into the combustion chamber leads to a radical reduction of the fluctuations, e.g. in pressure and temperature.

Moreover, the closer to the flame is the porous medium, the lower it takes to reach a limit cycle condition.
When the limit cycle is well established, some data are extracted at the end of the corresponding numerical simulation and then they are post-processed.
In figures 7.28, 7.29 and 7.30 are presented the plots of acoustic pressure inside the modeled combustor, for $d = 20\,mm$ and $\beta = 2$.
Please note that these plots are extracted at a generic instant during the limit cycle condition.

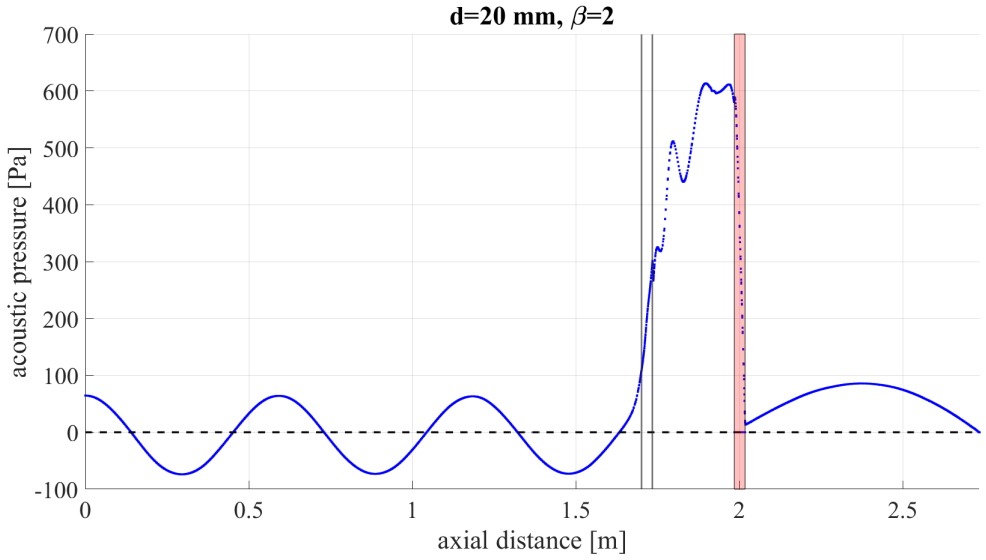

Figure 7.28: Plot of the acoustic pressure distribution along the axis of the combustor - case 1.

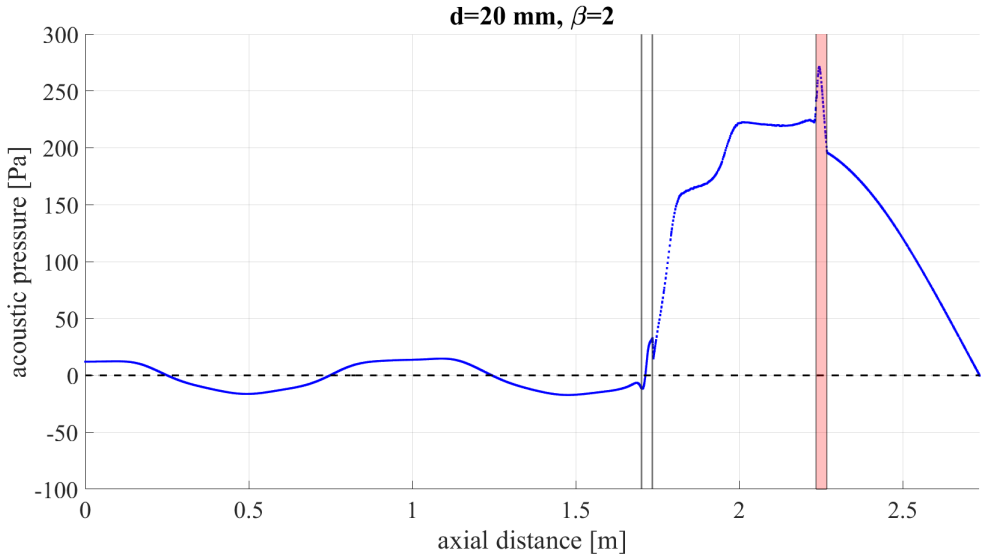

Figure 7.29: Plot of the acoustic pressure distribution along the axis of the combustor - case 2.

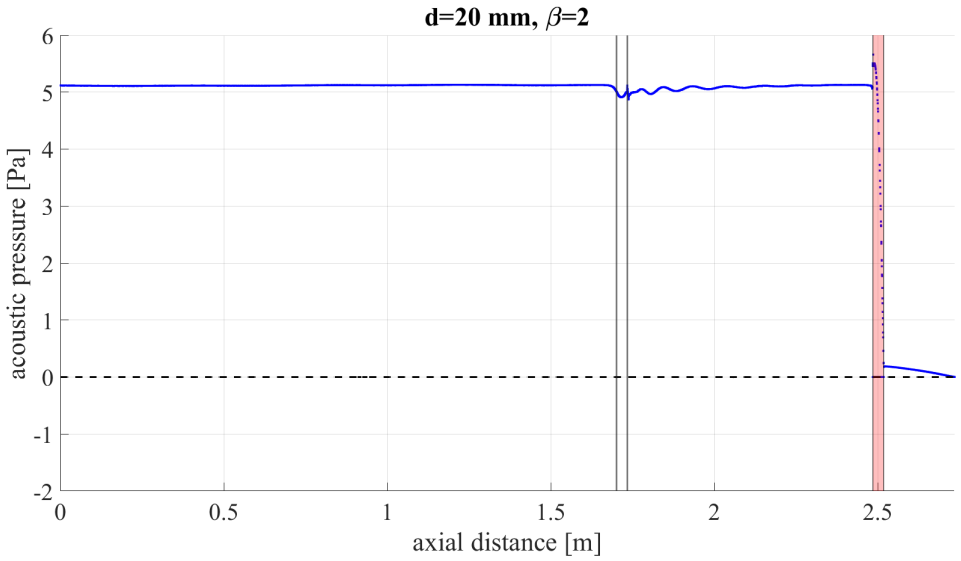

Figure 7.30: Plot of the acoustic pressure distribution along the axis of the combustor - case 3.

The red area represents the porous medium, where acoustic pressure quickly decreases through.
Referring to figure 5.43 where the values of acoustic pressure along the combustor's axis are plotted for the case without the porous medium, in the following figures it can be noticed that the porous septum damps the compression wave present in section three, please see the y-coordinate. The further the porous medium from the flame, the stronger is the reduction of acoustic pressure.
In figures 7.31, 7.32 and 7.33 are presented the plots of the temperature fluctuations inside the modeled combustor, again sampled along the axis, for $d = 20\,mm$ and $\beta = 2$. Also in this instance, they compared with the results from the previous case without porous medium.

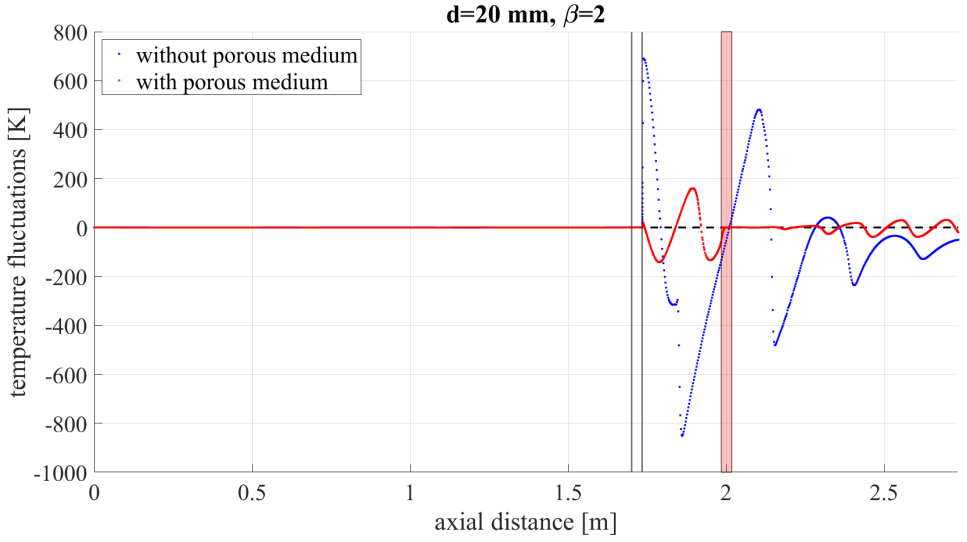

Figure 7.31: Plot of the temperature fluctuation distribution along the axis of the combustor - case 1.

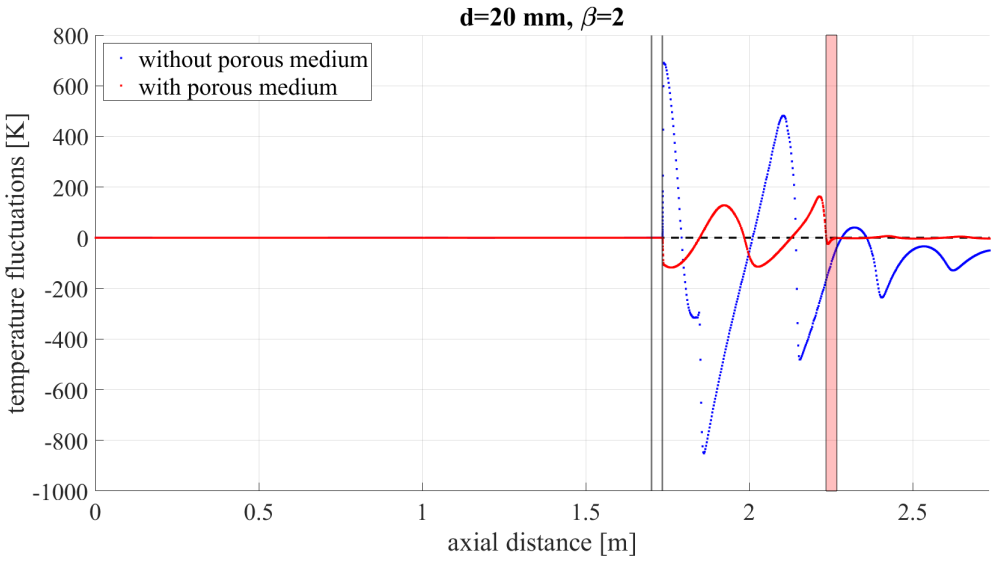

Figure 7.32: Plot of the temperature fluctuation distribution along the axis of the combustor - case 2.

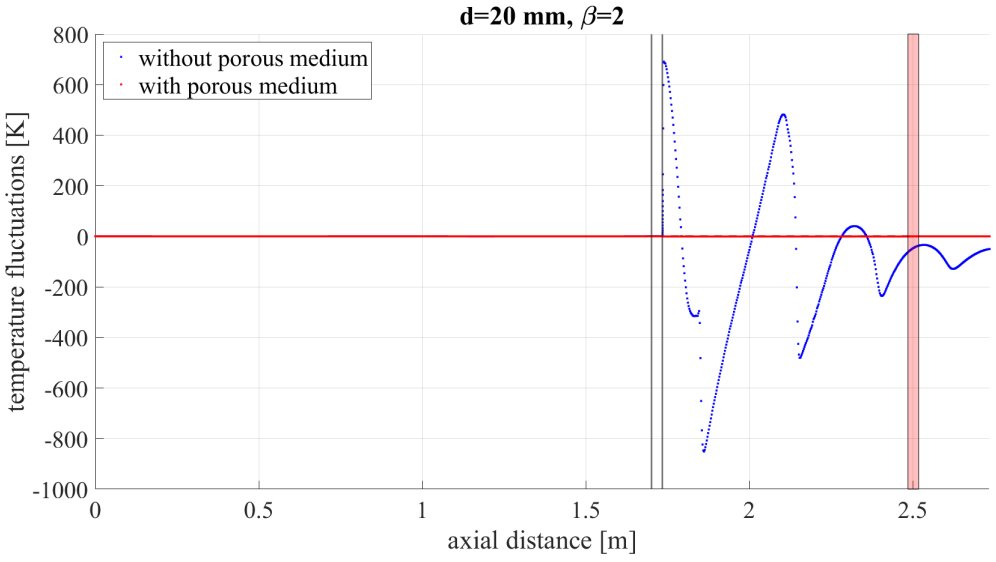

Figure 7.33: Plot of the temperature fluctuation distribution along the axis of the combustor - case 3.

One can also notice that after the porous disk the temperature fluctuations go to zero thanks to the strong damping. In the third configuration, the porous medium completely cuts off the oscillations.
The best configuration seems to be the third one, taking into account the strong reduction of the limit cycle amplitude, pressure and temperature fluctuations.

8 Implementation of a Helmholtz Resonator

8.1 Brief recap on Helmholtz Resonator

The Helmholtz resonator or Helmholtz oscillator is composed of two main parts: a rigid container of gas, an enclosed volume nearly spherical in shape, and a small neck or port, which communicates with the outside through a small opening.

Figure 8.1: A selection of Helmholtz resonators, at Hunterian Museum and Art Gallery in Glasgow.

The Helmholtz resonance is the phenomenon of air resonance in a cavity, such as when one blows across the top of an empty bottle. When air is forced into a cavity, the pressure inside increases; when the external force pushing the air into the cavity is removed, the higher-pressure air inside will flow out. Due to the inertia of the moving air, the cavity will be left at a pressure slightly lower than the outside, causing air to be drawn back in. This process repeats, with the magnitude of the pressure oscillations increasing and decreasing asymptotically after the sound starts and stops.
The resonant angular frequency is given by:

$$f_o = \frac{c}{2\pi} \cdot \sqrt{\frac{A_o}{l_o V_o}} \tag{8.1}$$

where f_0 is the resonance frequency $[Hz]$, c is the speed of sound $[m/s]$, A_o is the cross-sectional area of the neck $[m^2]$, l_o is the length of the neck [m] and V_o is the volume of air in the cavity $[m^3]$ [42].

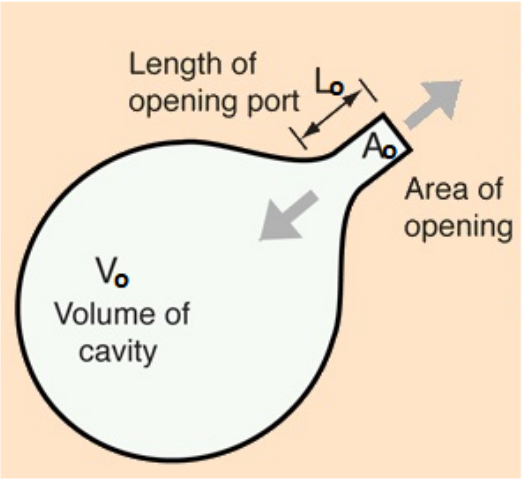

Figure 8.2: Simple design of a Helmholtz resonator.

8.2 Applications of Helmholtz Resonator in combustion technology

As previously said, low NO_x combustors are often associated with combustion instabilities which can cause structural damage to the engine.
Helmholtz resonators are commonly used to damp incident acoustic waves in many applications.
They have the advantage that they require a relatively small volume to damp oscillations at the relatively low frequencies found in combustion systems and thus provide a useful damping mechanism for combustion oscillations.
To control oscillations, they must directly communicate with the combustor itself. The need to incorporate the Helmholtz resonator, so that it can communicate with the combustion chamber, places strong constraints upon the opening dimension, the neck length, and the volume of the Helmholtz resonator [43].

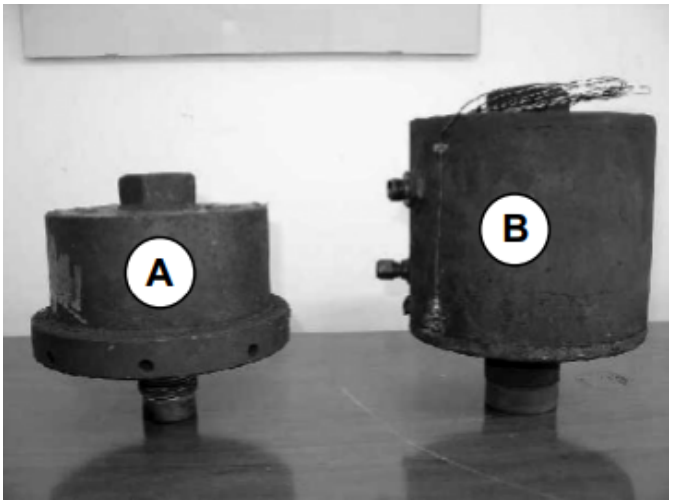

Figure 8.3: Two types of Helmholtz-resonators tested in an annular gas turbine combustor [44].

The application of Helmholtz resonators has also some disadvantages related to the fact that it tends to be efficient in a small frequency range, it generally does not respond to changes in the operating conditions and if the resonance frequency is not the right one, an amplification behavior of the thermoacoustic instabilities may occur.
The optimum damping of the eigenmodes is obtained when the resonance frequency f_o of the resonator is aligned with the natural frequency of the uncoupled combustor system.
According to the above considerations, when a Helmholtz resonator is applied to a combustion chamber, it must be tuned to the frequency that has to be damped in the combustor [45].

8.3 Case for a Helmholtz resonator located after the flame

This section presents the implementation of a Helmholtz resonator located 500 mm from the flame. Three different configurations have been designed, fixed in space, changing the neck's dimensions keeping constant the volume of the cavity.

8.3.1 Geometry

The sizing is developed thanks to the formula 8.1, fixing the resonance frequency equal to 385 Hz, which is the frequency that the Helmholtz resonator has to damp. The speed of sound is evaluated as an area weighted average in a line located in the same position as the resonator. The cross-sectional area of the neck and the volume of the cavity are calculated as follows:

$$A_o = 2\pi \cdot d_n \cdot R_{comb} \tag{8.2}$$

$$V_o = 2\pi^2 \cdot r_{cavity}^2 \cdot R_{tot} \tag{8.3}$$

where d_n is the "diameter" of the neck, R_{comb} is the radius of the combustor in section 3, r_{cavity} is the radius of the cavity and R_{tot} is the sum of R_{comb}, l_o and r_{cavity}.
The neck's dimensions d_n and l_o are varied, in order to obtain a resonance frequency equal to 385 Hz and to keep the volume of the cavity V_o fixed to 0.01 m^3, thus the r_{cavity} changes. Three different configurations are now defined and all of these are localized at 500 mm from the flame's position.
Furthermore, the second configuration 8.1, the intermediate one, is designed in the same three different positions from the flame, as the porous disk in figures 7.17, 7.18, 7.19, in order to deepen the influence of the resonator's position in the combustor chamber.

CASE	Figure	d_n [mm]	l_o [mm]	r_{cavity} [mm]	H. r. distance [mm]
1	8.4	6.8	20	65	500
2	8.5	15	45	60	500
3	8.6	24	70	55	500
4	-	15	45	60	250
5	-	15	45	60	750

Table 8.1: Configurations of the Helmholtz resonator.

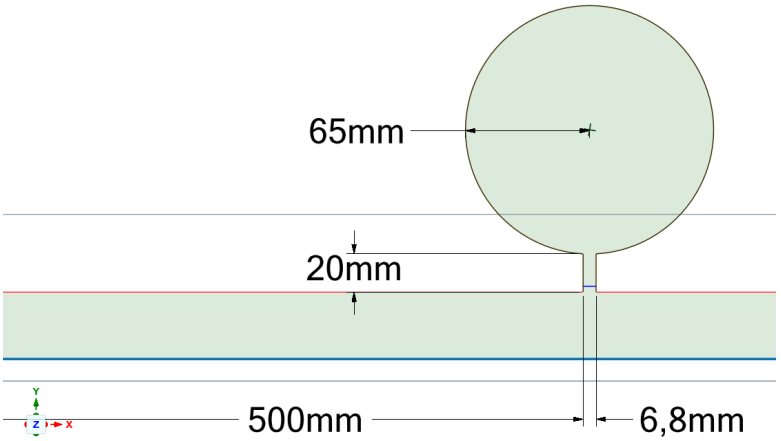

Figure 8.4: Geometry of the Helmholtz resonator: CASE 1.

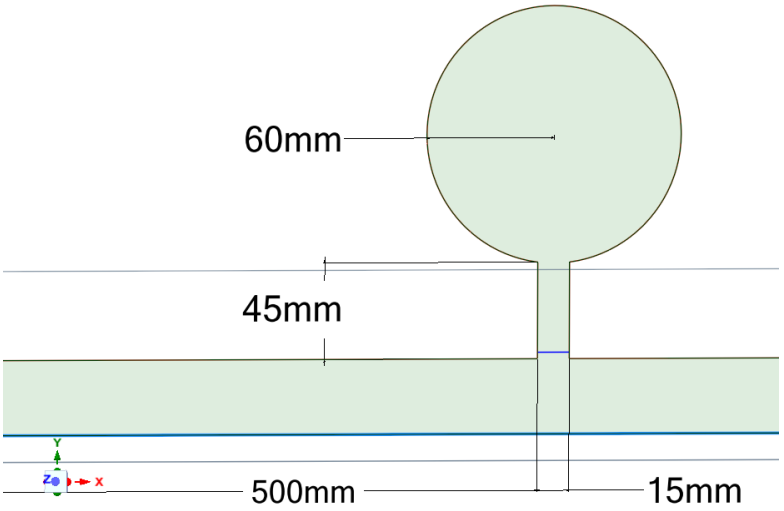

Figure 8.5: Geometry of the Helmholtz resonator: CASE 2.

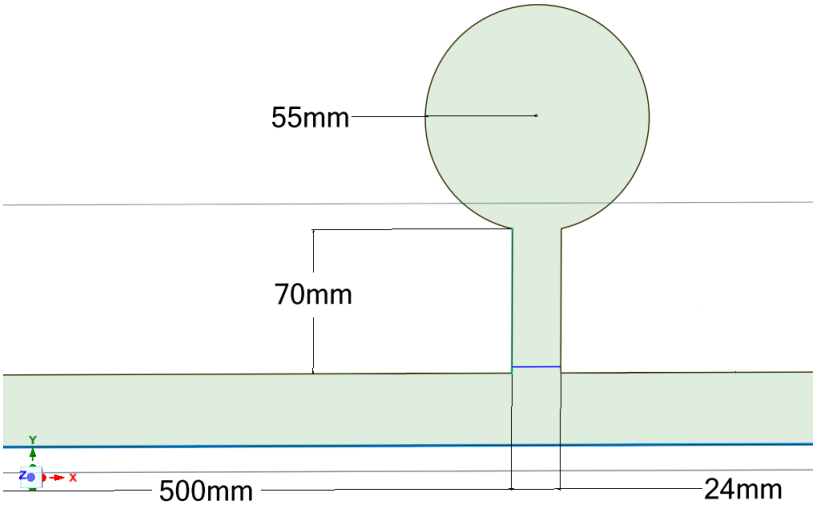

Figure 8.6: Geometry of the Helmholtz resonator: CASE 3.

8.3.2 Mesh and setup of the simulation

The second step is the mesh. Again, an unstructured mesh with triangular elements has been designed. The number of cells is 104190, and the minimum orthogonal quality is equal to 0.25668.
The mesh resonator detail is presented in the next two figures. The resonator's inlet is refined using face sizing, in particular, the chosen setting is a sphere of influence with a radius of 0.02 m and an element size smaller than the other parts equal to 0.0008 m.
The setup of the simulation using Fluent is exactly the same as the primary case.

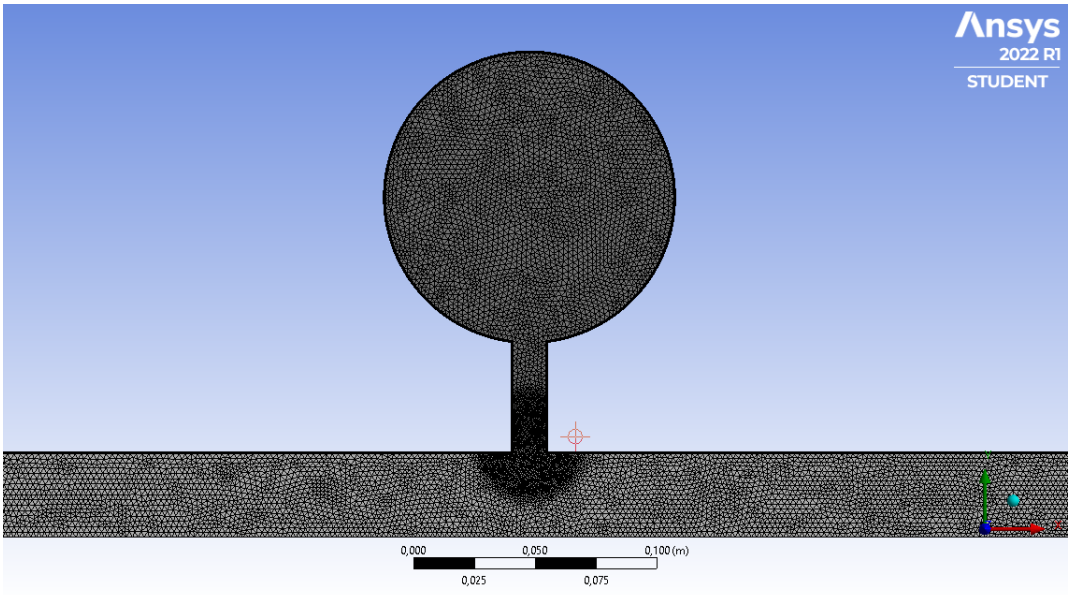

Figure 8.7: Mesh of the Helmholtz resonator.

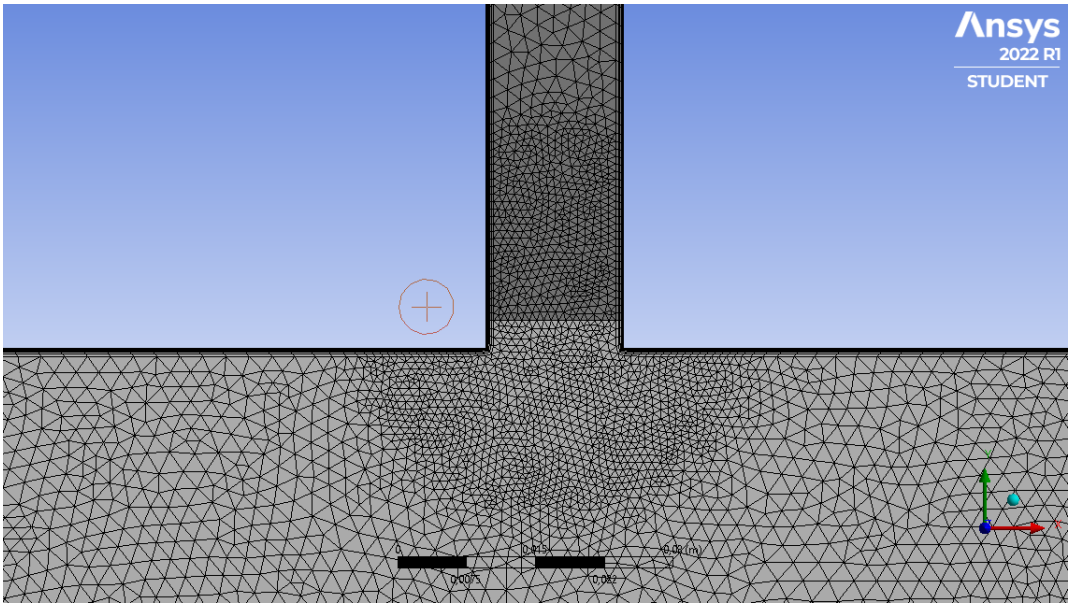

Figure 8.8: Zoom mesh of the Helmholtz resonator.

8.4 The steady and unsteady case for a constant heat source

The first two steps of the investigation have been conducted thanks to a RANS and a URANS simulations, fixing a constant value of the heat source term equal to 24218000000 W/m^3.
The steady case is initialized using a standard initialization from the inlet, which aligned the value of static temperature at 300 K.
As a result of the RANS simulation, we note that the static temperature contour isn't uniform in section 3. In particular, inside the Helmholtz resonator, the temperature is about 300 K thus the heat equilibrium condition isn't reached; this aspect is related to the fact that the velocity is approximately zero inside the resonator, so the heat transfer occurs only thanks to diffusion.
In order to correctly initialize the combustor model, it is used a patch initialization for the Helmholtz resonator which speeds the heat equilibrium condition, imposing this area at the initial temperature of 1900 K, please see figure 8.9.
This setting allows to have a correct initialization of the simulation, note the RANS result in figure 8.10.

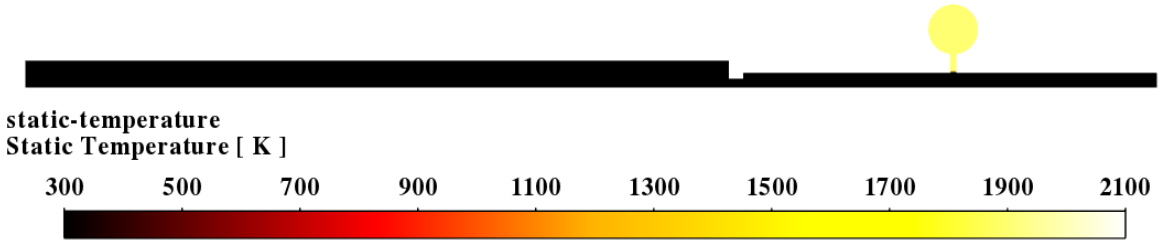

Figure 8.9: Initialization, static temperature distribution.

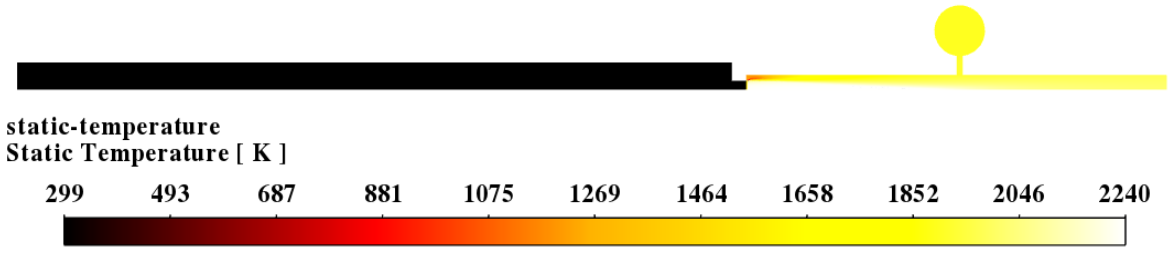

Figure 8.10: RANS simulation, static temperature distribution.

Now the simulation becomes transient, the fractional step method is set and then the unsteady case for a constant heat source is running in order to have a better starting condition for the URANS simulations.
In the following figures 8.11, 8.12 are presented a contour for the turbulent intensity and one for the axial velocity distribution. The behavior is very similar with the previous case and inside the Helmholtz resonator both the turbulent intensity and the axial velocity tend to zero, except for the resonator's inlet where there's a recirculation zone.

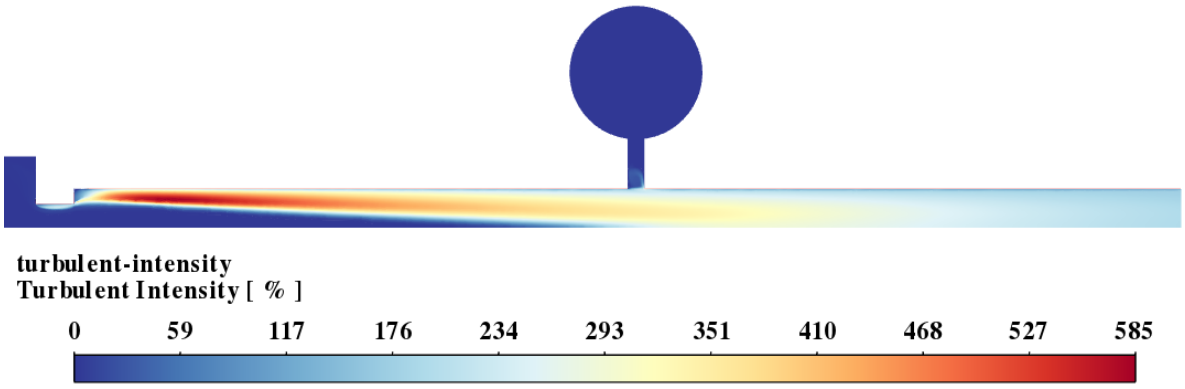

Figure 8.11: URANS simulation, turbulent intensity distribution.

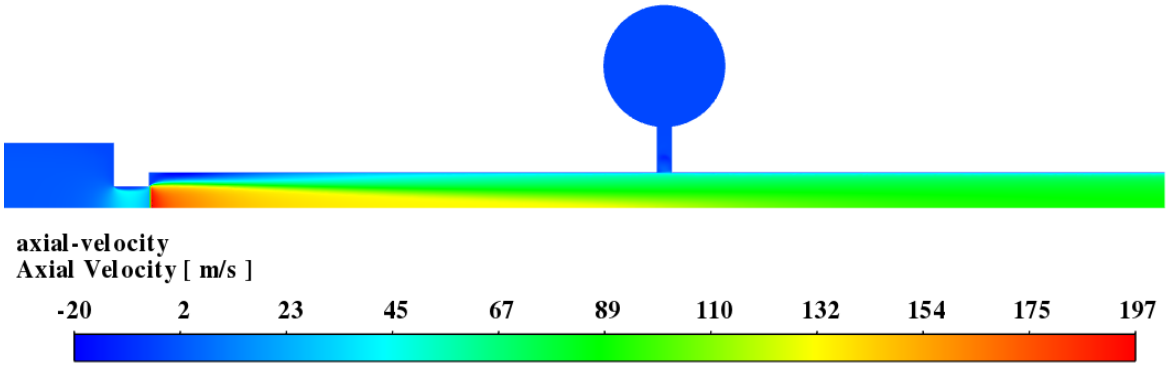

Figure 8.12: URANS simulation, axial velocity distribution.

As before, we can evaluate the overall sound pressure level (OASPL), in order to have an idea of the loudness of the model combustor during its operating condition. We have considered the trace of the acoustic pressure, when a statistically steady condition is reached, sampled in point 1 and 5. The OASPL results to be equal to 36 dB for point 1 and 17 dB for point 5.

8.4.1 Unsteady heat addition

This section aims to investigate the unstable behavior of the new combustor model, redesigned with the Helmholtz resonator, a device used to damp the thermoacoustic instabilities.
The source term implemented is the one used for the previous cases (5.2), fixing the spatial delay d equal to 20 mm and β equal to 2.
The first three cases 8.1 have decayed and they reach a stable condition, thus this result proves that, varying the neck's dimensions but keeping costant the value of the resonance frequency, the system works correctly.
Figures 8.17 and 8.18 present respectively the signal of the acoustic energy, the mass flow rate and the total heat transfer rate only for the Helmholtz resonator configuration number 2. The other two configurations are not reported because the trends are almost identical to the ones presented.

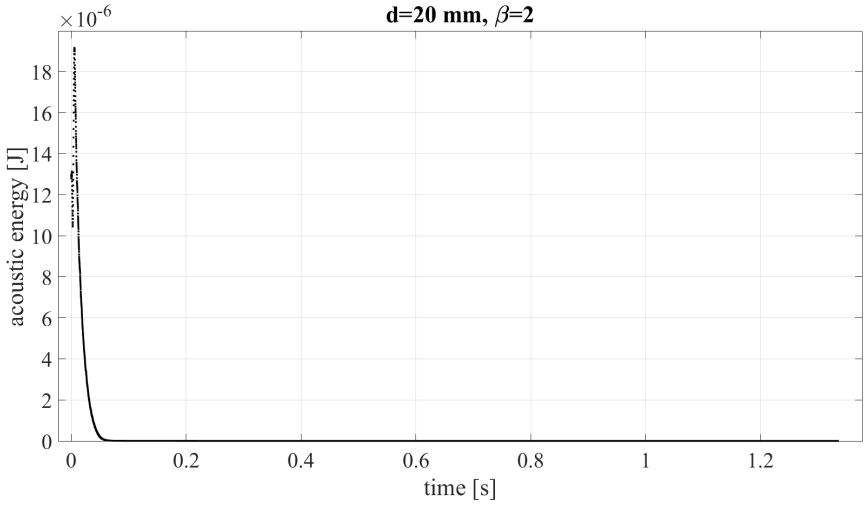

Figure 8.13: Signal of the acoustic energy for d=20 mm and $\beta = 2$.

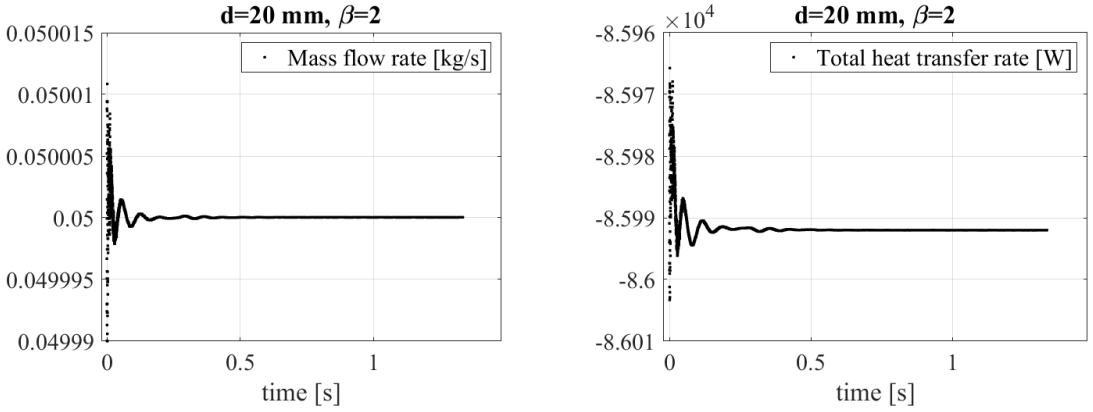

Figure 8.14: Mass flow rate and total heat transfer rate signals for d=20 mm and $\beta = 2$.

The following contours present the acoustic pressure distribution 8.19 and a comparison between this decayed case and the previous unstable case 8.21, using the same scale, to highlight the reduction and the strong damping of the pressure fluctuations. When the convergence condition is well established, some data are extracted at the end of the corresponding numerical simulation and then they are post-processed. Note that these contours are extracted at a generic instant, but remembering that fluctuating waves are stationary so the amplitude can change but not their positions.

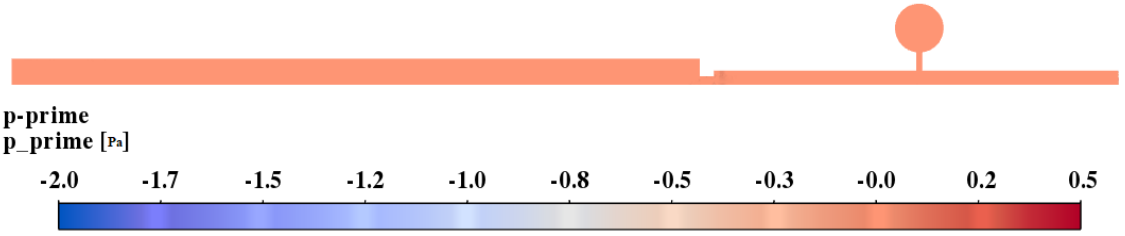

Figure 8.15: Acoustic pressure contour for d=20mm and $\beta = 2$ (CASE 2).

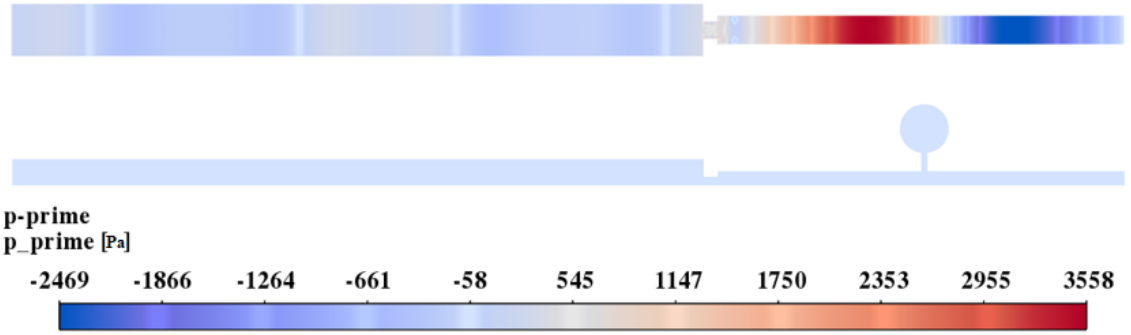

Figure 8.16: Comparison between the acoustic pressure contour for d=20mm and $\beta = 2$ with the Helmholtz resonator (CASE 2) and without.

Now, it's interesting to analyze the influence of the resonator's position in the combustion chamber. In particular, the last two cases in table 8.1 become unstable, but only the case 4 reach a limit cycle condition; for the case 5 the code diverges, thus the limit cycle condition isn't achieved.

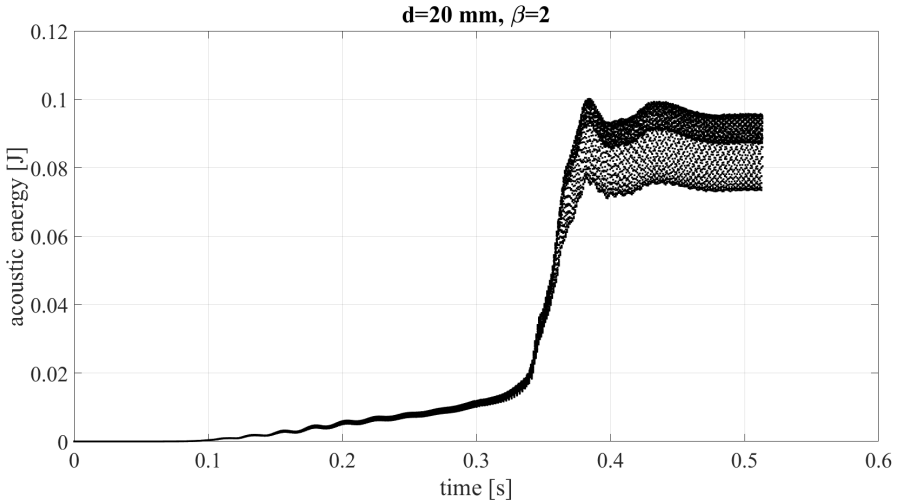

Figure 8.17: Signal of the acoustic energy for d=20 mm and $\beta = 2$.

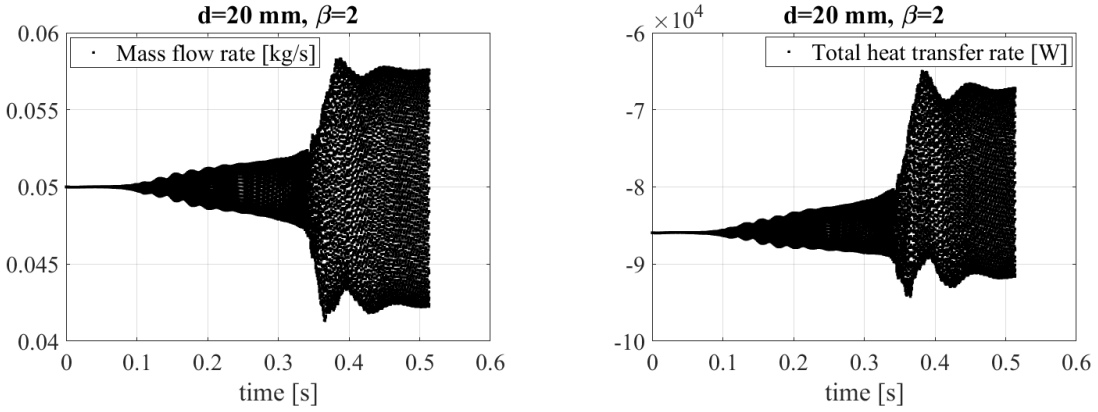

Figure 8.18: Mass flow rate and total heat transfer rate signals for d=20 mm and $\beta = 2$.

The previous figures present the signals of the acoustic energy, the mass flow rate, and of the total heat transfer rate, for the case 4.
As for the second configuration of the Helmholtz resonator design, the acoustic pressure contours are presented below.
Although the system becomes unstable, we see a reduction in the pressure fluctuations in comparison to the original unstable case.

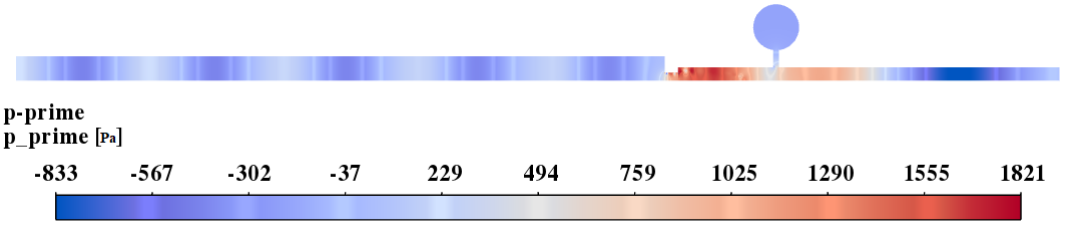

Figure 8.19: Acoustic pressure contour for d=20mm and $\beta = 2$ (CASE 4).

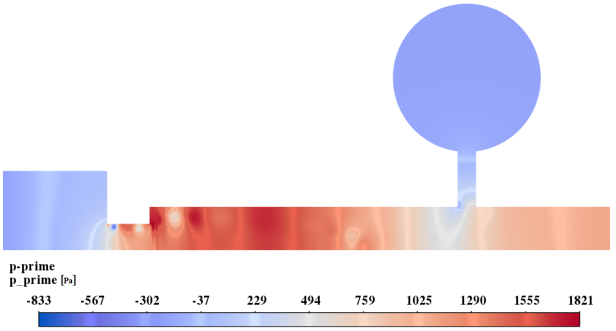

Figure 8.20: Zoom of the acoustic pressure contour for d=20mm and $\beta = 2$ (CASE 4).

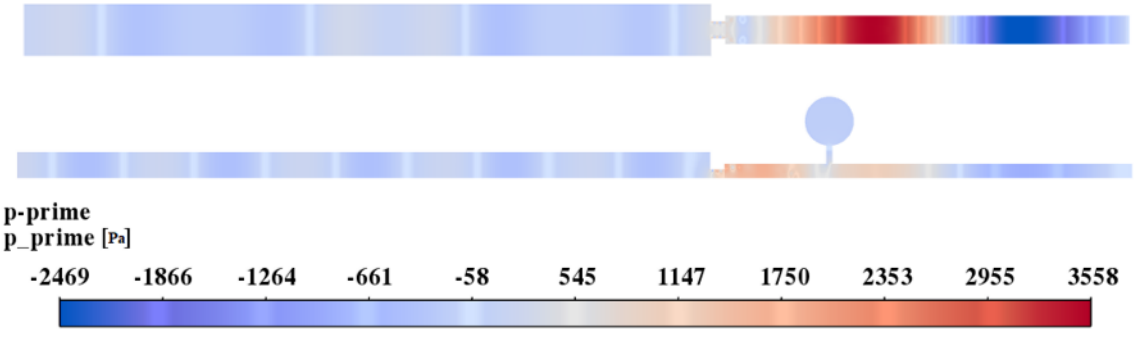

Figure 8.21: Comparison between the acoustic pressure contour for d=20mm and $\beta = 2$ with the Helmholtz resonator (CASE 4) and without.

From an acoustic point of view, the overall sound pressure levels measured in point 1 and 5 have an average value of 162 dB and 144 dB.
Finally, we can summarize and compare the unstable results, in particular the limit cycle amplitudes, for the initial case, the porous medium case and the Helmholtz

resonator case, by fixing the position of the damper devices at 250 mm from the flame.
The most efficient device is the porous medium, but we need to take into account that the porous septum causes more pressure losses than the Helmholtz resonator, thus it can be a good choice.

Case	**Limit cycle amplitude [*J*]**
Original case	$2.1 \cdot 10^{-1}$
Porous medium 250 mm from the flame	$1.3 \cdot 10^{-3}$
Helmholtz resonator 250 mm from the flame	$2.2 \cdot 10^{-2}$

Table 8.2: Comparison of the limit cycle amplitudes of the acoustic energy.

9 Conclusions

The purpose of this thesis is to analyze the thermoacoustic behavior of a simple modeled combustor for gas turbine applications.
In the first section of this work, we have learnt something about the modal analysis for this kind of problems. Additionally, we have understood the strong sensitivity that flame models can display, and that one should be fairly confident about the parameters to employ in the model, before fully trusting the results.
Next, as concerns, the Ansys Fluent analysis, dealing with this complex problem, and having to face various difficulties, has given us the opportunity to learn more about this CFD software. For example, we have learnt how to model a flame, and how to implement an unsteady heat release rate directly related to some flow variables. Moreover, although we have run only URANS simulations, that model all the turbulent scales, it has been an advantageous surprise to see that, a turbulence model like the $k-\omega$ SST is capable of determining and computing a limit cycle state.
With regards to the necessity to damp thermoacoustic oscillations, once found the right conditions that trigger instability, two damper devices are studied.
We have learnt how to size them and how to set up a simulation with a porous medium and a Helmholtz resonator.
In addition, we have seen that porous diaphragms located before the flame successfully damp thermoacoustic instabilities for many unstable states; on the contrary, porous sects located after the flame, if not positioned in the right spot, mostly reduce the peak-to-peak amplitude of limit cycle states, without completely eliminating the oscillations.
Helmholtz resonators are characterized by much smaller pressure losses than porous media; if the sizing is accurate and their position is the correct one, they work very well.
In conclusion, as future improvements some other flame models can be implemented on Ansys Fluent, some new active or passive control devices can be simulated, and some experimental tests deserve to be developed to verify the results obtained.

References

[1] A. P. Dowling and S. R. Stow. Acoustic analysis of gas turbine combustors. *Journal of propulsion and power*, 19(5):751–764, September–October 2003.

[2] T. C. Lieuwen. Unsteady combustor physics. *Cambridge University Press*, 2012.

[3] A. P. Dowling and A.S. Morgans. Feedback control of combustion oscillations. *Annual Review of Fluid Mechanics*, 37:151–182, 2005.

[4] D. Dutta and J. K. Bhattacharjee. Limit cycle oscillations. *Vibration Problems ICOVP-2007 (Part of the Springer Proceedings in Physics book series)*, 126:125–135, 2016.

[5] Polifke W. Thermoacoustic system modelling and stability analysis: conventional approaches. *Workshop on Advanced Instability Methods, IIT Madras, Chennai, India*, 2009.

[6] A. Cattanei. Dispense di aeroacustica. A.A. 2015-16.

[7] B.T. Chu and L. S. G. Kovásznay. Non-linear interactions in a viscous heat-conducting compressible gas. *Journal of Fluid Mechanics*, 3(05):494 – 514, February 1958.

[8] W. Polifke. Combustion instabilities. *Von Kármán Institute Lecture Series*, March 2004.

[9] A. Michalke. On spatially growing distur- bances in an inviscid shear layer. *Journal of Fluid Mechanics*, 23 (3):521–544, 1965.

[10] S. Ducruix, D. Durox, and S. Candel. Non-linear interactions in a viscous heat-conducting compressible gas. *Centre National de la Recherche Scientifique and Ecole Centrale de Paris*.

[11] W. Polifke and C. Lawn. On the low-frequency limit of flame transfer functions. *Combustion and Flame*, 151:437–451, 2007.

[12] A. Bottaro. Turbulence and CFD models, part one. A.A. 2021.

[13] K. Balasubramanian and R. Sujith. Thermoacoustic instability in a Rijke tube: Non-normality and nonlinearity. *Physics of Fluids*, 20(4), 2008.

[14] R. Sujith, M. Juniper, and P. Schmid. Non-normality and nonlinearity in thermoacoustic instabilities. *International Journal of Spray and Combustion Dynamics*, 8, 2016.

[15] S. Strogatz. Nonlinear dynamics and chaos. *Westview Pres*, 2001.

[16] F. E. C. CulicK. Combustion instabilities in liquid-fueled propulsion systems. *AGARD Conference Proceedings*, 450, 1988.

[17] B. T. Chu and L. S. G. . Kovasznay. Non-linear interactions in a viscous heat-conducting compressible gas. *Journal of Fluid Mechanics*, 3:494 – 514, 1958.

[18] S. Hemchandra. Dyamics of turbulent premixed flames in acoustic fields. *PhD thesis, Georgia Institute of Technology,*, 2009.

[19] A. P. Dowling. Nonlinear self-excited oscillations of a ducted flame. *Journal of Fluid Mechanics*, 346(1):271–290, 1997.

[20] A. P. Kelley and C. K. Law. Nonlinear effects in the extraction of laminar flame speeds from expanding spherical flames. *Journal of Fluid Mechanics*, 346(1):271–290, 1997.

[21] N. Karimi, M. J. Brear, S.H. Jin, and J. P. Monty. Linear and non-linear forced response of a conical, ducted, laminar premixed flame. *Combustion and Flame*, 156(9):1844–1851, 2009.

[22] T. Schuller, D. Durox, and S. Candel. A unified model for the prediction of laminar flame transfer functions: comparisons between conical and v-flame dynamics. *Combustion and Flame*, 34(1-2):21–34, 2003.

[23] Shreekrishna, S. Hemchandra, and T. Lieuwen. Premixed flame response to equivalence ratio perturbations. *Combustion Theory and Modelling*, 14(5):681–714, 2010.

[24] C. Jahnke and F. Culick. Application of dynamical systems theory to nonlinear combustion instabilities. *Journal of Propulsion and Power*, 10:508–517, 1994.

[25] N. Ananthkrishnan, S. Deo, and F. Culick. Reduced-order modeling and dynamics of nonlinear acoustic waves in a combustion chamber. *Combustion Science and Technology*, 177:1–27, 2005.

[26] M. Juniper. Triggering in thermoacoustics. *International Journal of Spray and Combustion Dynamics*, 4(3), 2012.

[27] A. A. Mancini and H. C. Mongia. Mixer assembly for gas turbine engine combustor. *(General Electric Co) Patent*, US8171735B2, 2005.

[28] F. Giannetti and P. Luchini. Structural sensitivity of the first instability of the cylinder wake. *Journal of Fluid Mechanics*, 581:167–197, 2007.

[29] J. Kornegay, D. Depperschimdt, and A.K. Agrawal. Passive control of thermoacoustic instability in different length combustors using a high-strength metallic porous insert. *ASME Turbo Expo 2015: Turbine Technical Conference and Exposition*, 2015.

[30] R. Corá, C.A. Martins, and P.T. Lacava. Acoustic instabilities control using helmholtz resonators. *Applied Acoustics*, 77:1–10, 2014.

[31] J.M. De-Bedout, M.A. Franchek, R.J. Bernhard, and L. Mongeau. Adaptive-passive noise control with self-tuning helmholtz resonators. *J of Sound Vibration*, 202:109–123.

[32] J.D. Eldredge, A.P. Dowling, and P.T. Lacava. The absorption of axial acoustic waves by a perforated liner with bias flow. *Journal of Fluid Mech.*, 485:307–335.

[33] R. Kashani and J. Monfort. Low-frequency thermo-acoustic instability mitigation using adaptive-passive acoustic radiators. *ASME Paper GT*, 46642, 2011.

[34] S. Sobhani, J. Legg, D.F. Bartz, and J.J. et al Kojimac. Experimental investigation of lean premixed pre-vaporized liquid-fuel combustion in porous media burners at elevated pressures up to 20 bar. *Applied Acoustics*, 212:123–134, 2020.

[35] Zhao. Dan, Lu Zhengli, Zhao He, Li X.Y., Wang Bing, and Liu Peijin. A review of active control approaches in stabilizing combustion systems in aerospace industry. *Progress in Aerospace Sciences*, 97:35–60, 2018.

[36] S. Chalia, M. Kumar Bharti, P. Thakur, A. Thakur, and S.N. Sridhara. An overview of ceramic materials and their composites in porous media burner applications. *ELSEVIER - Ceramics International*, 47:10426–10441, 2021.

[37] E. Noordally, J.M. Przybylskil, and J.J. Witton. Porous media combustors for clean gas turbine engines. *United States Navy, Office of Naval Research Naval International Co-operative Opportunities in Science and Technology Program*, 2004.

[38] M.M. Kamal and A.A. Mohamad. Combustion in porous media. *Journal of Power and Energy*, pages 220–487, 2006.

[39] S.S. Su, S.J. Hwang, and W.H. Lai. On a porous medium combustor for hydrogen flame stabilization and operation. *International Journal of Hydrogen energy*, 39:21307–21316, 2014.

[40] Ansys fluent academic research, release 2021, help system, ansys fluent theory guide, ansys, inc.

[41] A.F. Abuserwal. Pressure drop and forced convective heat. *The University of Sheffield*, 2017.

[42] S. Hubbard and A. P. Dowling. Acoustic resonances of an industrial gas turbine combustion system. *ASME Journal of Engineering for Gas Turbines and Power*, 123:766–773, 2001.

[43] I.D.J. Dupère and A.P. Dowling. The use of helmholtz resonators in a practical combustor. *ASME Journal of engineering FOR gas turbines and power*, 127:268–275, 2005.

[44] J. Lepers, B. Prade, G. Pollarolo, W. Krebs, P. Flohr, and A. Ferrante. Investigation of thermoacoustic stability limits of an annular gas turbine combustor test-rig with and without helmholtz resonators. *ASME Turbo Expo 2005: Power for Land, Sea and Air*, 2005.

[45] S. Chalia, M. Kumar Bharti, P. Thakur, A. Thakur, and S.N. Sridhara. On the use of helmholtz resonators for damping acoustic pulsations in industrial gas turbines. *Journal of Engineering for Gas Turbines and Power*, 126:271–275, 2004.